

2



Defense Nuclear Agency
Alexandria, VA 22310-3398



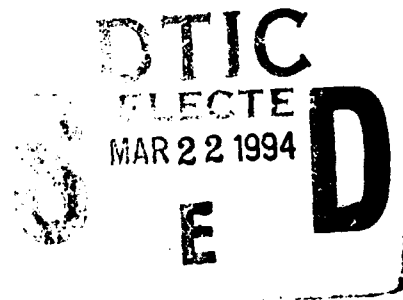
AD-A277 271

DNA-TR-93-61



Probabilistic Prediction of Late-time Nuclear Clouds

R. Ian Sykes
Stephen F. Parker
Douglas S. Henn
The Titan Corporation
California Research & Technology Div.
ARAP Office
P.O. Box 2229
Princeton, NJ 08543-2229



March 1994

Technical Report

CONTRACT No. DNA 001-90-C-0100

Approved for public release;
distribution is unlimited.

94-08944



DTIC QUALITY INSPECTED 1

'94 3 21 045

Destroy this report when it is no longer needed. Do not return to sender.

PLEASE NOTIFY THE DEFENSE NUCLEAR AGENCY,
ATTN: CSTI, 6801 TELEGRAPH ROAD, ALEXANDRIA, VA
22310-3398, IF YOUR ADDRESS IS INCORRECT, IF YOU
WISH IT DELETED FROM THE DISTRIBUTION LIST, OR
IF THE ADDRESSEE IS NO LONGER EMPLOYED BY YOUR
ORGANIZATION.



CLASSIFIED BY:

N/A since Unclassified

DECLASSIFY ON:

N/A since Unclassified

may be lofted by turbulent eddies and remain in the atmosphere for long periods. Calculations have been made for a range of atmospheric conditions for periods of 24 hours. The general conclusion from these studies is that the major factor influencing the fraction of dust remaining aloft after 12-24 hours is the initial size distribution. Meteorological variations produce some effect on the rate of fallout, but material with diameters above about $30\mu\text{m}$ is mostly deposited within 12 hours, while diameters below $10\mu\text{m}$ are only slightly depleted by gravitational settling over this time period. The turbulent deposition can be significant over forested areas, however, so that particles of $10\mu\text{m}$ size can be significantly reduced over a 12 hour period when compared to $1\mu\text{m}$ particles.

An analytical description of the statistics of low-level dust concentrations at late time after a nuclear burst was obtained, based on the r.m.s. fluctuations in the wind field. The problem is complicated by the fact that late-time dust at low altitude is comprised of a superposition of different particle sizes falling from different initial altitudes. The spatial location of the different size groups therefore depends on the integrated wind vector over the range of the descent. The analytic predictions were compared with a direct Monte Carlo simulation of a horizontally homogeneous wind field acting on the initial cloud. The analytic description must account for the vertical correlation of the wind field. A simple exponential correlation function resulted in a good representation of the probability distribution for an aircraft intercept mass.

A study was performed to determine the sensitivity of the dispersion prediction to variations in the initial conditions for a release of radioactive material from an attack on a nuclear power plant. The diffusive nature of atmospheric dispersion reduces the dependence on initial conditions as transport time increases, although conserved quantities such as total release mass are clearly unaffected by the diffusion process. Factors such as release height and release size are not critical for transport over distances greater than a few kilometers. The most critical aspects are the release height relative to the planetary boundary layer depth and the size distribution of the release. Releases of small particles or gaseous species above the mixed layer can remain aloft for long times before being mixed down to the surface. Releases inside the mixed layer, however, are quickly mixed through the boundary layer. A demonstration calculation was performed using a DICE/MAZ prediction of the radioactive cloud from a 20kT weapon, showing the extent of the contamination and the probabilistic prediction capability of the model.

CONVERSION TABLE

Conversion Factors for U.S. Customary to Metric (SI) Units of Measure

MULTIPLY TO GET	BY BY	TO GET DIVIDE
angstrom	1.000 000 X E -10	meters (m)
atmosphere (normal)	1.013 25 X E +2	kilo pascal (kPa)
bar	1.000 000 X E +2	kilo pascal (kPa)
British thermal unit (thermomechanical)	1.054 350 X E +3	joule (J)
calorie (thermomechanical)	4.184 000	joule (J)
cal (thermochemical)/cm ²	4.184 000 000 X E -2	megajoule/m ² (MJ/M ²)
curie	3.700 000 X +	* giga becquerel (GBq)
degree (angle)	1.745 329 X E -2	radian (rad)
degree Fahrenheit	$t_k = (T_F + 459.67)/1.8$	degree kelvin (K)
electron volt	1.602 19 X E -19	joule (J)
erg	1.000 000 X E -7	joule (J)
erg/second	1.000 000 X E -7	watt (W)
foot	3.048 000 X E -1	meter (m)
foot-pound-force	1.355 818	joules (J)
gallon (US. liquid)	3.785 412 X E -3	meter ³ (m ³)
inch	2.540 000 X E -2	meter (m)
jerk	1.000 000 X E +9	joule (J)
joule/kilogram (J/kg) (radiation dose absorbed)	1.000 000	Gray (Gy)
kilotons	4.183	terajoules
kip (1000 lbf)	4.448 222 X E +3	newton (N)
kip/inch ² (ksi)	6.894 757 X E +3	kilo pascal (kPa)
ktop	1.000 000 X E +2	newton-second/m ² (N-s/m ²)
micron	1.000 000 X E -6	meter (m)
mil	2.540 000 X E -5	meter (m)
mile (international)	1.609 344 X E +3	meter (m)
ounce	2.834 952 X E -2	kilogram (kg)
pound-force (lbs avoirdupois)	4.448 222	newton (N)
pound-force inch	1.129 848 X E -1	newton-meter (N*m)
pound/force/inch	1.751 268 X E +2	newton/meter (N/m)
pound/force/foot ²	4.788 026 X E -2	kilo pascal (kPa)
pound-force inch ² (psi)	6.894 757	kilo pascal (kPa)
pound-mass (lbm avoirdupois)	4.535 924 X E -1	kilogram (kg)
pound-mass-foot ² (moment of inertia)	4.214 011 X E -2	kilogram-meter
pound-mass-foot ³	1.601 846 X E +1	kilogram/meter ³ (kg/m ³)
rad (radiation dose absorbed)	1.000 000 X E -2	** Gray (Gy)
roentgen	2.579 760 X E -4	coulomb/kilogram (C/kg)
shake	1.000 000 X E -8	second (s)
slug	1.459 390 X E +1	kilogram (kg)
torr (mm Hg, °C)	1.333 22 x E -1	kilo pascal (kPa)

* the becquerel (Bq) is the SI unit of radioactivity; 1 Bq = 1 event/s.

** The Gray (Gy) is the SI unit of absorbed radiation.

TABLE OF CONTENTS

Section	Page
SUMMARY.....	iii
CONVERSION TABLE.....	v
FIGURES.....	vii
1 INTRODUCTION	1
2 'DUST-OFF' MODEL COMPARISON.....	3
2.1 OBJECTIVES AND METHODOLOGY	3
2.2 SCIPUFF MODEL IMPROVEMENTS	3
2.2.1 Improved Wind Shear Treatment	4
2.2.2 Relative Diffusion Prediction	7
2.3 TEST CASE RESULTS.....	9
3 ANATEX MODEL EVALUATION STUDY	18
4 BOUNDARY LAYER DIFFUSION EFFECTS	27
4.1 BACKGROUND	27
4.2 NUMERICAL MODEL.....	28
4.2.1 Turbulent Transport Model.....	28
4.2.2 Turbulent Deposition Model.....	30
4.2.3 Initial Conditions	32
4.2.4 Meteorological Parameters	35
4.3 RESULTS	38
4.4 SUMMARY OF BOUNDARY LAYER RESULTS.....	52
5 STATISTICAL FALL-OUT ANALYSIS	53
6 SCIPUFF MODEL STUDIES	69
6.1 RADIOACTIVE FALLOUT FROM 20KT WEAPON	69
6.2 NUCLEAR POWER PLANT RELEASE SENSITIVITIES.....	77
7 CONCLUDING REMARKS.....	86
8 REFERENCES.....	89
APPENDIX.....	91

FIGURES

Figure	Page
2-1	Multiburst scenario release locations..... 4
2-2	Winds for 16 January 1978 at 55°N, 37.5°E and 00Z..... 5
2-3	SCIPUFF results for the single burst scenario using the January wind field. Perspective views of the 10^{-10} gm/cm ³ iso-surface at $t = 0, 1$ and 8 hrs 8
2-4	SCIPUFF results for the single burst scenario using the January wind field Horizontal cross-sections at $t = 8$ hrs. Contour levels of $10^{-13}, 10^{-12}, 10^{-11}, 10^{-10}, 10^{-9}, 10^{-8},$ and 10^{-7} gm/cm ³ 11
2-5	SCIPUFF results for the single burst scenario using the July wind field. Horizontal cross-sections at $t = 8$ hrs. Contour levels of $10^{-13}, 10^{-12}, 10^{-11}, 10^{-10}, 10^{-9}, 10^{-8},$ and 10^{-7} gm/cm ³ 12
2-6	SCIPUFF results for the multi-burst scenario using the January wind field. Horizontal cross-sections at $t = 8$ hrs. Contour levels of $10^{-13}, 10^{-12}, 10^{-11}, 10^{-10}, 10^{-9}, 10^{-8},$ and 10^{-7} gm/cm ³ 13
2-7	SCIPUFF results for the multi-burst scenario using the July wind field. Horizontal cross-sections at $t = 8$ hrs. Contour levels of $10^{-13}, 10^{-12}, 10^{-11}, 10^{-10}, 10^{-9}, 10^{-8},$ and 10^{-7} gm/cm ³ 14
2-8	Intercepted dust masses along horizontal flight paths through the single burst cloud after 8 hours with winter winds. (a) East-West paths, (b) North-South paths. ——— $z=100\text{m}$; — — — — — $z=8\text{km}$; - - - - - $z=12\text{km}$ 15
2-9	SCIPUFF results for the single burst scenario using the January wind field and absolute diffusion scheme. Horizontal cross-sections at $t = 8$ hrs and $z = 100$ m. (a) mean total dust concentration, (b) r.m.s. fluctuation in total dust. Contour levels of $10^{-13}, 10^{-12}, 10^{-11}, 10^{-10},$ and 10^{-9} gm/cm ³ 16

FIGURES (Continued)

Figure	Page
2-10 Fractal realizations from the ensemble statistics of Figure 2-9. Horizontal cross-sections at $t = 8$ hrs and $z=100$ m. Contour levels of 10^{-13} , 10^{-12} , 10^{-11} , 10^{-10} , and 10^{-9} gm/cm ³	16
3-1 ANATEX release and surface sampler locations	19
3-2 Comparison of the SCIPUFF 24hr average PTCH surface concentration patterns with the observed patterns for the period 23-25 March	21
3-3 Predicted and observed ground sample cumulative distribution functions for the period 9-28 March	22
3-4 Predicted and observed ground sample cumulative distribution functions for PTCH along three arcs for the period 5 January-21 February. Predictions were made using a standard boundary layer depth of 1000m	23
3-5 Predicted and observed aircraft sample cumulative distribution functions for the period 9-28 March	24
3-6 Adjusted predicted and observed aircraft sample cumulative distribution functions for the period 9-28 March	25
3-7 Predicted and observed ground sample cumulative distribution functions for the period 9-28 March. Predictions were made using the ensemble meteorology	26
4-1 Surface deposition and gravitational settling velocity versus particle diameter for two surface roughness lengths. Surface friction velocity is assumed to be 0.4m/s, and the deposition is calculated for a height of 10m	32
4-2 Dust field from DICE at $t = 5$ mins. Contours are in g/cc	33

FIGURES (Continued)

Figure	Page
4-3 Vertical profiles of horizontally-integrated dust concentration from the DICE run at $t = 5$ mins. (a) show full profile (note logarithmic concentration scale), (b) shows detail in the lowest levels.	34
4-4 Diurnal variation of the planetary boundary layer. (a) r.m.s. vertical velocity fluctuation, contour interval 0.1m/s. (b) surface heat flux in Km/s.....	37
4-5 Integrated dust profiles at 4, 8, and 12 hours after release. Release is at (a) 00:00; (b) 06:00; (c) 12:00; (d) 18:00. Wind speed 10m/s, roughness length 0.01m	39
4-6 Integrated dust profiles at 4, 8, and 12 hours after release. Release is at (a) 00:00; (b) 06:00; (c) 12:00; (d) 18:00. Wind speed 10m/s, roughness length 1.0m	42
4-7 Integrated dust profiles at 4, 8, and 12 hours after release. Release is at (a) 00:00; (b) 06:00; (c) 12:00; (d) 18:00. Wind speed 2m/s, roughness length 1.0m	44
4-8 Integrated dust profiles at 12 hours after 06:00 release. Surface heat flux maximum is 0.075Km/s unless noted.	46
4-9 Integrated dust profiles at 4, 8, and 12 hours after release. Release is at (a) 00:00; (b) 06:00; (c) 12:00; (d) 18:00. Wind speed 10m/s, roughness length 0.01m, pedestal dust only	48
4-10 Integrated dust profiles at 12 hours after 06:00 release assuming all dust is 10 microns. Surface heat flux maximum is 0.075Km/s unless noted	50
4-11 Integrated dust profiles at 12 hours after 06:00 release assuming proposed incipient particle size distribution. Surface heat flux maximum is 0.075Km/s unless noted.....	51

FIGURES (Continued)

Figure	Page
5-1	Wind statistics for the East-West component from 3652 Moscow wind profiles. (a) local wind at altitude; (b) average wind between altitude and ground 57
5-2	Mean mass loading after 8 hours along a North-South flightpath at 100m altitude for an ensemble of 3652 Moscow winds. The explicit Monte-Carlo result (solid) and the ensemble statistical calculation (dashed) are shown as a function of East-West location relative to the burst 58
5-3	Cumulative distribution of the mass loading at 8 hours from the Monte-Carlo results with 3652 winds (i.e. probability that loading is less than given value) at two locations 60
5-4	Correlation between East-West velocities at two altitudes from 3652 Moscow wind profiles. Lower level is fixed at 1450m. Correlations between the local velocity and the average over the layer between the two levels are shown 63
5-5	R.m.s. mass loading after 8 hours for a North-South flightpath at 100m from an ensemble of 3652 Moscow winds. The explicit Monte-Carlo result (solid) and the statistical ensemble calculation (dashed) are shown 65
5-6	Probability of mass loading exceeding 1 mg/cm ² for the ensemble of 3652 Moscow winds. Comparison between Monte-Carlo calculation (solid) and statistical estimate (dashed) 66
5-7	Probability of mass loading exceeding 10 mg/cm ² for the ensemble of 3652 Moscow winds. Comparison between Monte-Carlo calculation (solid) and statistical estimate (dashed) 67
6-1	Distribution of radioactive material at $t = 5$ mins. (a) vertical distribution of active mass; (b) distribution by particle size, contours indicate fraction of mass contained in particles smaller than the indicated diameter 70

FIGURES (Continued)

Figure	Page
6-2 Initial wind field for the SCIPUFF simulation	71
6-3 SCIPUFF prediction of the ensemble mean concentration and standard deviation at $z=100\text{m}$ and $z=5\text{km}$ 8 hours after initiation of a 20kT burst centered at 42°N , 88°W . Contour levels of 10^{-3} , 10^{-2} , 10^{-1} , 1, and $10\mu\text{g}/\text{m}^3$	73
6-4 SCIPUFF prediction of the ensemble mean surface dose 8 hours after initiation of a 20kT burst centered at 42°N , 88°W . Contour levels of 10^{-7} , 10^{-6} , 10^{-5} , 10^{-4} , 10^{-3} and $10^{-2}\mu\text{g}/\text{m}^2$	74
6-5 SCIPUFF prediction of the ensemble mean surface radiation dose 8 hours after initiation of a 20kT burst centered at 42°N , 88°W . Contour levels of 0.01, 0.1, 10^{-5} , 1, 10 and 100rad/hr	75
6-6 SCIPUFF prediction of the probability of exceeding a surface radiation dose of (a) 0.1rad/hr and (b) 10rad/hr 8 hours after initiation of a 20kT burst. Contour levels of 1%, 5%, 20%, 50%, 80%, 100%.....	76
6-7 Surface dose at 48 hours after the release of a gaseous material at 500m from the Illinois source. Release start at (a) 01/07/87:00:00, (b) 02/04/87:00:00, (c) 03/04/87:00:00, (d) 01/07/87:12:00, (e) 02/04/87:12:00, (f) 03/04/87:12:00.	79
6-8 Surface dose at 48 hours after the release of a gaseous material at 500m from the Four Corners source. Release start at (a) 01/07/87:00:00, (b) 02/04/87:00:00, (c) 03/04/87:00:00, (d) 01/07/87:12:00, (e) 02/04/87:12:00, (f) 03/04/87:12:00.	79
6-9 Surface dose at 48 hours after the release on 02/04/87 at 12:00 from the Illinois source. Release of (a) gas at 500m, (b) gas at 1000m, (c) gas at 2000m, (d) 10μ at 500m, (e) 10μ at 1000m, (f) 10μ at 2000m	80

FIGURES (Continued)

Figure	Page
6-10 Surface dose at 48 hours after the release on 02/04/87 at 12:00 from the Illinois source. Release of (a) 30 μ m at 500m, (b) 30 μ m at 1000m, (c) 30 μ m at 2000m.....	80
6-11 Surface dose at 8 hours after the release of a gaseous material at 200m from the Illinois source. Release start at (a) 01/07/87:00:00, (b) 02/04/87:00:00, (c) 03/04/87:00:00, (d) 01/07/87:12:00, (e) 02/04/87:12:00, (f) 03/04/87:12:00.....	82
6-12 Surface dose at 8 hours after the release of a gaseous material at 200m from the Illinois source.. Release start at (a) 01/07/87:00:00, (b) 02/04/87:00:00, (c) 03/04/87:00:00, (d) 01/07/87:12:00, (e) 02/04/87:12:00, (f) 03/04/87:12:00.....	82
6-13 Surface dose at 8 hours after the release of a gaseous material at 200m from the Illinois source. (a) gas at 200m, (b) gas at 1000m, (c) gas at 2000m, (d) 10 μ at 200m, (e) 10 μ at 1000m, (f) 10 μ at 2000m	83
6-14 Surface dose at 8 hours after the release of a gaseous material at 200m from the Illinois source. (a) 30 μ m at 200m, (b) 30 μ m at 1000m, (c) 30 μ m at 2000m, (d) 100 μ m at 200m, (e) 100 μ m at 1000m, (f) 100 μ m at 2000m	83
6-15 Surface dose at 8 hours after the release on 02/04/87 at 00:00 from the Illinois source. (a) gas at 200m, (b) gas at 500m, (c) gas at 1000m, (d) 10 μ m at 200m, (e) 10 μ m at 500m, (f) 10 μ m at 1000m	84
6-16 Surface dose at 8 hours after the release on 02/04/87 at 00:00 from the Illinois source. (a) 30 μ m at 200m, (b) 30 μ m at 500m, (c) 30 μ m at 1000m, (d) 100 μ m at 200m, (e) 100 μ m at 500m, (f) 100 μ m at 1000m	84

SECTION 1

INTRODUCTION

The dust cloud lofted by a nuclear explosion contains a wide range of particle sizes, including many fine particles that can remain airborne for hours or days after the detonation. The dust environments from multiple bursts can therefore present a hazard to various defense systems and there is a need for quantitative prediction of the late-time cloud distributions. The late-time evolution of the cloud is largely controlled by the atmospheric wind field, which is responsible for dispersing the small particles. Other factors, such as gravitational settling and interaction with water/ice clouds, also play a role in determining the removal rate of the dust from the atmosphere.

The effects of wind on a dust cloud are generally described as transport and diffusion, and most mathematical models make a clear conceptual distinction between the two processes. The diffusion is represented in an analogous way to molecular diffusion and the observed, or forecast, wind field is used to move the cloud. This distinction between *transport* and *diffusion* relies upon a wide difference in length scales for the two processes. The diffusion of the cloud is actually brought about by random turbulent eddies, which separate particles from one another as they are advected in the chaotic flow field. If the turbulence eddies only exist at small scales, then we can clearly distinguish between the transport winds (the large scale variations) and the diffusing winds. Unfortunately, the spectrum of eddies in the atmosphere includes variations on all spatial scales, from millimeters up to global scale, and there is no spectral gap between the resolvable transport winds and the random turbulent eddies. The distinction between transport and diffusion is therefore arbitrary, and is defined by the resolution of the wind field. All "known" details of the wind field are included as transport, while "unknown" wind variations must be represented statistically as diffusion. The "knowledge" of the wind field is determined by the observing network, or the reliability of the numerical forecast.

The preceding discussion clearly implies that no prediction of atmospheric dispersion can be completely certain. The degree of uncertainty depends on the available input information for the prediction, but the inherent limitation on our knowledge of the detailed state of the atmosphere generally leads to significant uncertainty levels. The

initial development of the SCIPUFF (Second-order Closure Integrated Puff) model attempted to include a quantitative treatment of the uncertainty due to three-dimensional turbulent eddies in the planetary boundary layer (Sykes et al., 1988), and was extensively validated against local dispersion measurements at ranges of up to 50km. Under DNA sponsorship, SCIPUFF was extended to include dynamic effects of water condensation and evaporation (Lewellen et al., 1991) and also for application to larger scale dispersion problems. In this report, we describe the continued development of the quantitative description of prediction uncertainty for long range atmospheric transport and dispersion.

Several studies are reported below. Extensions of SCIPUFF and comparisons with other models and with tracer data from field experiment are described in Sections 2 and 3. An investigation of the effects of vertical diffusion in the planetary boundary layer is presented in Section 4. Section 5 deals with the representation of the uncertainty in a falling cloud of dust particles, with application to the aircraft environment at low altitude at times of several hours after burst. Section 6 describes several applications of SCIPUFF in the prediction of atmospheric dispersion, and finally Section 7 summarizes the principal findings of the report.

SECTION 2

'DUST-OFF' MODEL COMPARISON

2.1 OBJECTIVES AND METHODOLOGY.

The 'Dust-Off' model comparison exercise was initiated to examine the differences between various late-time cloud prediction models, and to determine the important features of the models with respect to the prediction of nuclear cloud evolution. Current models use a variety of diffusion parameterizations and numerical representation techniques, and valuable information on sensitivities can be obtained from direct comparison of model predictions. A series of test cases and a set of output measures were defined for three models, SCIPUFF, SAIC's TORAS, and Kaman's PEPPER code.

The test cases consisted of both single and multiburst scenarios and two representative wind fields. The initial cloud was specified as the LM02 TASS solution (300kT surface burst) at $t=10$ mins., and the dispersion model input was derived from the (r,z) -distributions, as appropriate. The single burst release location was 55°N, 37.5°E. The multiburst scenario consisted of 133 identical clouds, all released at the same initial time, with the horizontal spatial distribution shown in Figure 2-1. Three-dimensional wind fields were obtained at 12-hour intervals from the U.S. Air Force Environmental Technical Applications Center (ETAC) for 16 January and 4 July 1978. The winds were provided on a standard 64×64 grid for the Northern hemisphere, which was then interpolated onto a latitude-longitude mesh giving an effective spatial resolution of about 400km. Standard pressure levels were specified for the vertical profile, and a standard U.S. atmosphere was used to determine geometric heights. Release time was 00Z for each of the two days, and the cloud evolution was computed out to 16 hours after release.

2.2 SCIPUFF MODEL IMPROVEMENTS.

Two new features were added to SCIPUFF for the 'Dust-Off' comparison exercise. An improved treatment of wind shear effects was incorporated, and the capability to use a 'relative diffusion' estimate was added to the code. The 'relative diffusion' prediction

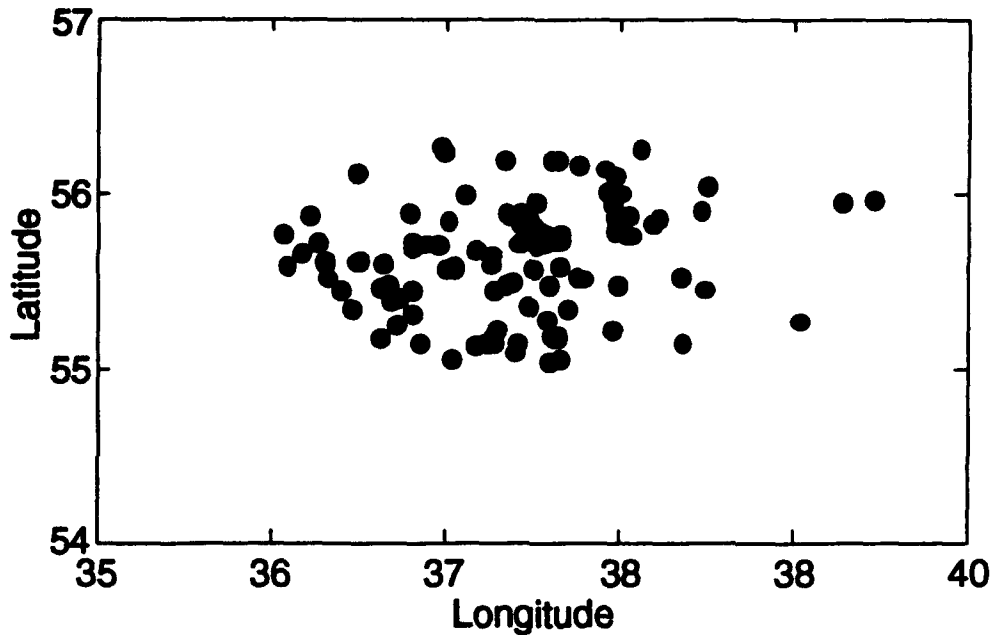


Figure 2-1. Multiburst scenario release locations.

allowed a more direct comparison between the SCIPUFF predictions and those from other models.

2.2.1 Improved Wind Shear Treatment.

The wind profile at the single burst release location for the winter case is shown in Figure 2-2, and clearly displays a very strong vertical shear. Over a 16 hour period, the distortion due to the vertical shear dominates the dispersion of the cloud. The existing version of SCIPUFF used a Gaussian shape for each of the collection of puffs, with separate spread parameters in each of the three orthogonal directions, that is, East-West, North-South, and vertical. Vertical wind shear was represented as an enhanced horizontal spread rate for each component direction. This method does not properly describe wind shear, which distorts the Gaussian shape rather than diffusing it, so a more complete treatment was implemented.

The restriction of the Gaussian spatial moment description to the three coordinate axes is equivalent to specifying a diagonal form for the second-moment tensor. The general definition of the second-moment is

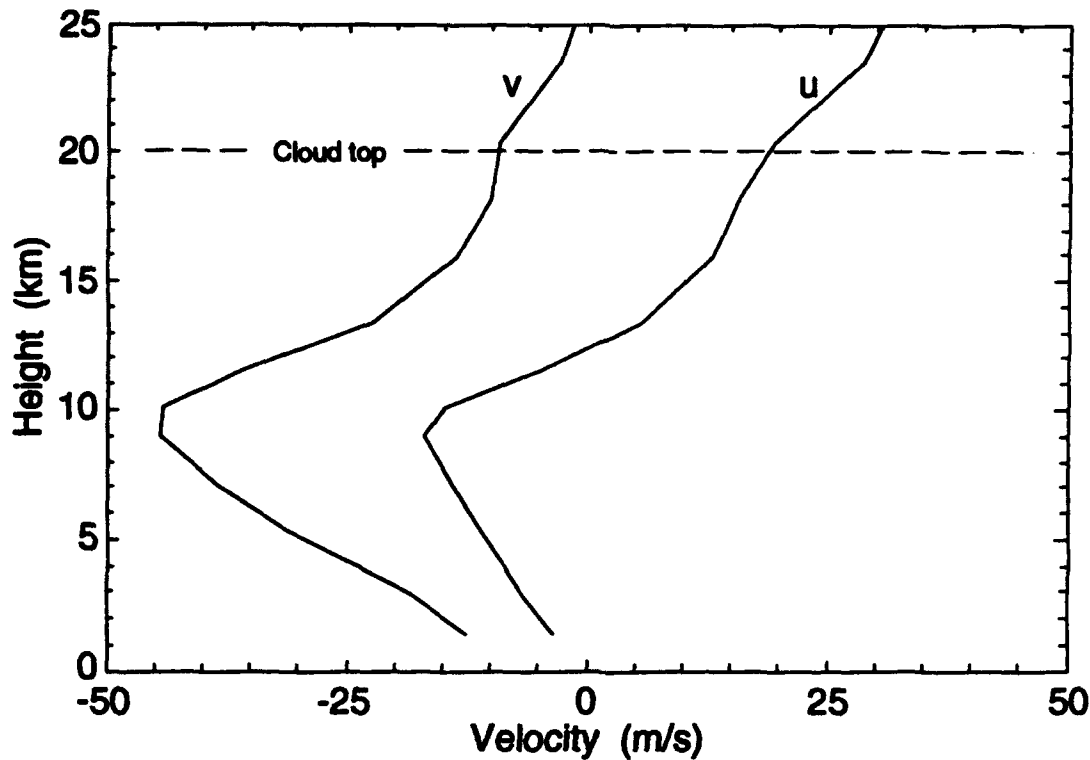


Figure 2-2. Winds for 16 January 1978 at 55°N, 37.5°E and 00Z.

$$\sigma_{ij} = \frac{1}{Q} \int x'_i x'_j c dV \quad (2.1)$$

where Q is the total mass of the puff, c is the local concentration, and x'_i is the coordinate vector relative to the puff centroid. The local puff concentration is represented by the generalized Gaussian distribution

$$c(x) = \frac{Q}{(2\pi)^{3/2} (Det(\sigma))^{1/2}} \exp\left[-\frac{1}{2} \sigma_{ij}^{-1} x'_i x'_j\right] \quad (2.2)$$

The general Gaussian distribution therefore requires 6 moments instead of 3, since the second-rank tensor is symmetric. The effect of wind shear on the evolution of the second moments is given by

$$\frac{d\sigma_{ij}}{dt} = \sigma_{ik} \frac{\partial u_j}{\partial x_k} + \sigma_{kj} \frac{\partial u_i}{\partial x_k} \quad (2.3)$$

so that a completely general wind field can be included. The wind shear terms are in addition to the turbulent diffusion terms, but it is important to note that a non-divergent

velocity field cannot increase the volume of the puff in the absence of diffusion terms. The volume is proportional to $Det(\sigma)^{1/2}$ and conservation of volume is an equivalent statement to zero-divergence in the velocity field. Conservation is derivable from Equation (2.3) using the definition of the determinant

$$6Det(\sigma) = \epsilon_{i\alpha\beta}\epsilon_{j\gamma\delta}\sigma_{ij}\sigma_{\alpha\gamma}\sigma_{\beta\delta} \quad (2.4)$$

(Jeffreys, 1963), where ϵ_{ijk} is the alternating third rank tensor. Differentiating Equation (2.4) with respect to time gives

$$2\frac{d}{dt}(Det(\sigma)) = \epsilon_{i\alpha\beta}\epsilon_{j\gamma\delta}\frac{d\sigma_{ij}}{dt}\sigma_{\alpha\gamma}\sigma_{\beta\delta} \quad (2.5)$$

and substituting from Equation (2.2), we obtain

$$\begin{aligned} 2\frac{d}{dt}(Det(\sigma)) &= \epsilon_{i\alpha\beta}\epsilon_{j\gamma\delta}\sigma_{\alpha\gamma}\sigma_{\beta\delta}\left(\sigma_{ik}\frac{\partial u_j}{\partial x_k} + \sigma_{jk}\frac{\partial u_i}{\partial x_k}\right) \\ &= 2Det(\sigma)\epsilon_{i\alpha\beta}\epsilon_{k\alpha\beta}\frac{\partial u_i}{\partial x_k} \\ &= 4Det(\sigma)\frac{\partial u_i}{\partial x_i} \end{aligned}$$

which is zero for a divergence-free velocity field.

The equations for the second-moments are advanced sequentially by means of analytical solutions for the diagonal strain components, followed by each off-diagonal velocity gradient component individually. These analytic solutions conserve the puff volume so the only diffusive effect is due to the turbulence parameterization.

Generalization of the puff description requires modification to the puff interaction calculation, local concentration computations, and also in the puff splitting/merging algorithms. The overlap integrals and concentration evaluations must account for the skewed axes of the Gaussian, and the splitting rules utilize the off-diagonal Gaussian moments to determine the locations of the newly-created puffs. Both splitting and merging conserves all the puff moments, and the splitting algorithm produces puffs with smaller volume and realizable moments.

A demonstration of the capability provided by the improved treatment of shear is illustrated in Figure 2-3, which shows the single burst cloud evolving over 8 hours in the January wind field. The perspective views of the 10^{-11} gcm^{-3} iso-surface use a distorted

scale to represent the horizontal stretching of the cloud, which covers a range of several hundred kilometers by the end of the computation. The ability of the puffs to distort under the action of the persistent shear allows the code to maintain a continuous representation of the cloud without unreasonable computational effort. This calculation contained 646 puffs at the last time illustrated with 10 particle size groups in the representation.

2.2.2 Relative Diffusion Prediction.

The standard concentration field output from *SCIPUFF* consists of an ensemble average concentration along with a prediction of the variance about the mean. The ensemble is dependent on the input wind field data, which is always incomplete due to limited spatial and temporal resolution, and the model predictions give a probabilistic description of the concentration field resulting from the uncertain winds. This makes comparison between *SCIPUFF* predictions and those from a conventional deterministic model very difficult. In order to facilitate such comparisons, we modified the *SCIPUFF* diffusion algorithm to allow the use of a 'relative diffusion' scheme. The concepts of 'absolute' and 'relative' dispersion are discussed by Pasquill (1974) and can loosely be thought of as continuous 'plume' dispersion and instantaneous 'puff' dispersion, respectively. Absolute dispersion corresponds to the normal *SCIPUFF* ensemble average, where (unresolved) eddies of all scales are included in the dispersion process. This can be interpreted as a long time average of a continuous plume, where the averaging is sufficiently long to sample all the eddies. More generally, the ensemble average is a probabilistic prediction, where large eddies are regarded as meandering the cloud and introducing uncertainty into its position; a long term average will reduce this uncertainty and give the usual plume average, but a short term average can still contain significant uncertainty.

We can regard a deterministic prediction of the cloud dispersion as an attempt to predict the likely concentration in the cloud, ignoring the uncertainty in its position. There is no clear distinction between the 'meandering' eddies and the 'diffusing' eddies, but there is a natural way to restrict the *SCIPUFF* prediction to include only the cloud-scale eddies. *SCIPUFF* already requires an estimate of the cloud-scale turbulence to

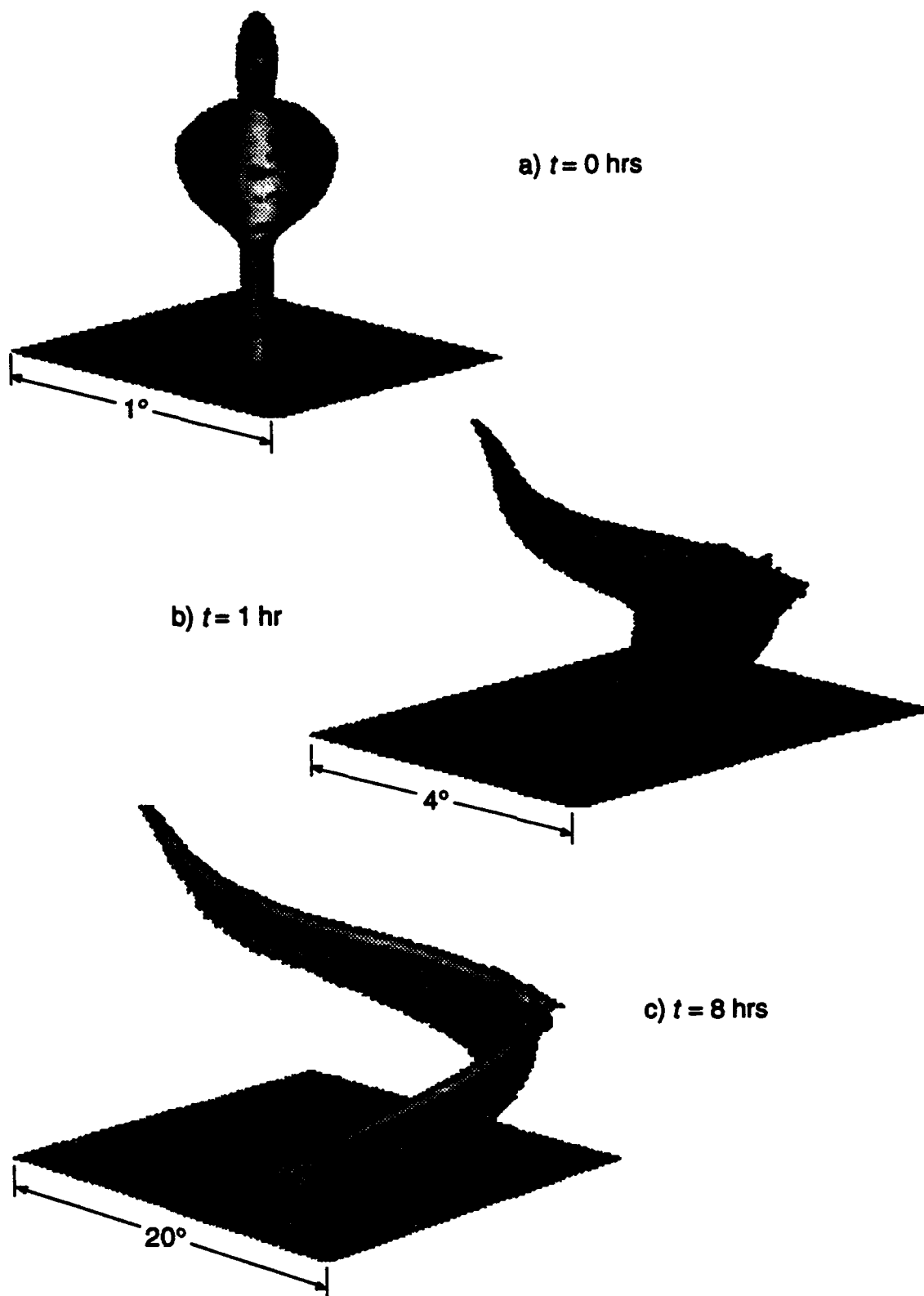


Figure 2-3. SCIPUFF results for the single burst scenario using the January wind field. Perspective views of the 10^{-10} g/cm³ iso-surface at $t = 0, 1$ and 8 hrs.

calculate the dissipation of the concentration fluctuation variance, so we define a 'relative' diffusion prediction to utilize only this part of the turbulence spectrum. Specifically, given a cloud length scale, λ_c , and a turbulence length scale representing the 'maximum' energy-containing eddy size, Λ_H , we represent the velocity variance available for diffusion as

$$\overline{u_r'^2} = \overline{u_B'^2} \left(\frac{\lambda_c}{\Lambda_H} \right)^{2/3} \quad (2.6)$$

for $\lambda_c < \Lambda_H$, where $\overline{u_B'^2}$ is the ambient velocity variance. This representation is consistent with the observed 5/3-power law spectrum (Nastrom and Gage, 1985).

2.3 TEST CASE RESULTS.

Results from the model inter-comparison exercise are not the subject of this report, but we shall present several examples of the SCIPUFF output for the designated test cases. As discussed above, single and multiple burst scenarios were specified for two meteorological conditions. Some experimentation was performed to determine the appropriate resolution for the calculation, particularly with regard to the particle size distribution. A logarithmically uniform size bin spacing was employed, ranging from $1\mu\text{m}$ up to $1024\mu\text{m}$, with a dust density of 2.0gcm^{-3} . Test runs were made with 5, 10, 20, and 40 size bins, showing that 10 bins was sufficient to maintain an accurate description of the cloud over the time period of the calculation. The model resolution was effectively extended by the inclusion of an additional vertical spread term to represent the range of particle fall velocities over the finite range of the size bin. Thus, the particles fall with the mass-weighted mean velocity, given by

$$\overline{v_d} = \sum_{i=1}^3 \alpha_i v_{di}$$

where

$$v_{d1} = v_d(d_{\min})$$

$$v_{d2} = v_d(d_{\text{mean}})$$

$$v_{d3} = v_d(d_{\max})$$

referring to the particle fall speed at the minimum, mean, and maximum sizes in the size bin, respectively. The mass weights, α_i , are inversely proportional to the diameter, consistent with the -4 power law for the number density. The vertical puff spread

equation includes a growth term, so that σ_z increases like σ_{vd} , where the r.m.s. fall velocity is obtained from the three values at the bin boundaries and bin center. i.e.,

$$\sigma_{vd}^2 = \sum_{i=1}^3 \alpha_i v_{di}^2 - \bar{v}_d^2$$

This additional term spreads the puffs and maintains a continuous vertical concentration distribution, reducing the tendency for puffs to separate due to differential fall speeds.

Horizontal cross-sections through the concentration field at $t=8$ hrs and at three standard altitudes are presented in Figures 2-4 through 2-7. These fields show both total dust concentration and also the concentration of dust particles with sizes greater than $50\mu\text{m}$ from each of the four cases, i.e., winter and summer winds, single and multiburst scenarios. These four calculations were made using the relative diffusion algorithm described in Section 2.2.2, and there are several features of interest in the results.

First, we note the continuous nature of the SCIPUFF prediction. The particle size distribution resolution together with the generalized Gaussian puff description allows the code to maintain an accurate description of the highly distorted cloud as it shears and separates the different particle sizes. This is particularly evident in the single burst, winter wind case shown in Figure 2-4. Here the strong wind shear stretches the cloud over a distance of order 1000km over the 8hr period. This stretching separates the main cloud from the pedestal, as can be seen by comparing the total dust plot with that for the dust above $50\mu\text{m}$. The larger particles in the section at $z=100\text{m}$ must necessarily have originated at much higher altitudes, since they have been falling for 8hrs, while the smaller particles originated at altitudes much closer to 100m. Comparison between the two concentration fields shows that the larger particles form the Western section of the cloud furthest from the burst location, while the smaller pedestal particles make up the high concentrations in the North-East. These cross-section plots can be compared with the perspective view of the cloud in Figure 2-3, where the "curtain" of larger particles falling out of the sheared cloud downstream of the pedestal is clear.

The summer wind case in Figure 2-5 shows a simpler cloud structure, but the wind shear effect is still obvious. The multiburst scenarios (Figures 2-6 and 2-7) can be thought of as a simple superposition of 133 single burst clouds with appropriate origin shifts. These calculations show the same basic features as the single burst scenarios, but

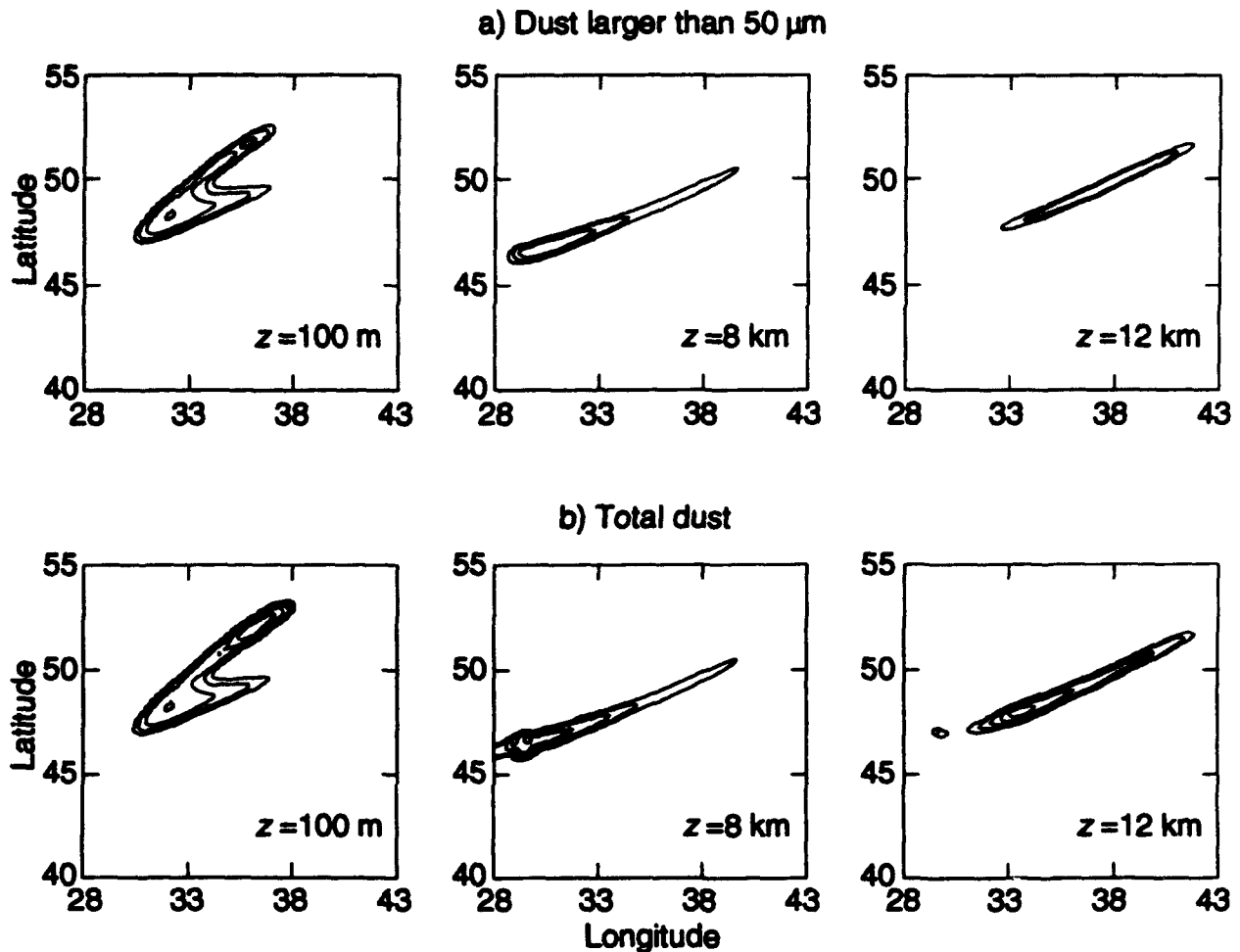


Figure 2-4. SCIPUFF results for the single burst scenario using the January wind field. Horizontal cross-sections at $t = 8$ hrs. Contour levels of 10^{-13} , 10^{-12} , 10^{-11} , 10^{-10} , 10^{-9} , 10^{-8} and 10^{-7} gm/cm^3 .

there is less detail in the clouds since the overlapping concentration fields tend to smooth out the individual features.

The intercepted dust along an aircraft flightpath is an important quantity for strategic planning purposes, and Figure 2-8 shows the SCIPUFF prediction for both North-South and East-West paths through the single burst cloud shown in Figure 2-4. Integrated dust concentrations are shown at the three altitudes as a function of intercept latitude or longitude. The shear-induced offset is clear in the altitude dependence, and the near-surface separation between the main cloud and the pedestal is also evident, with the pedestal dust lying to the North and the East of the main cloud.

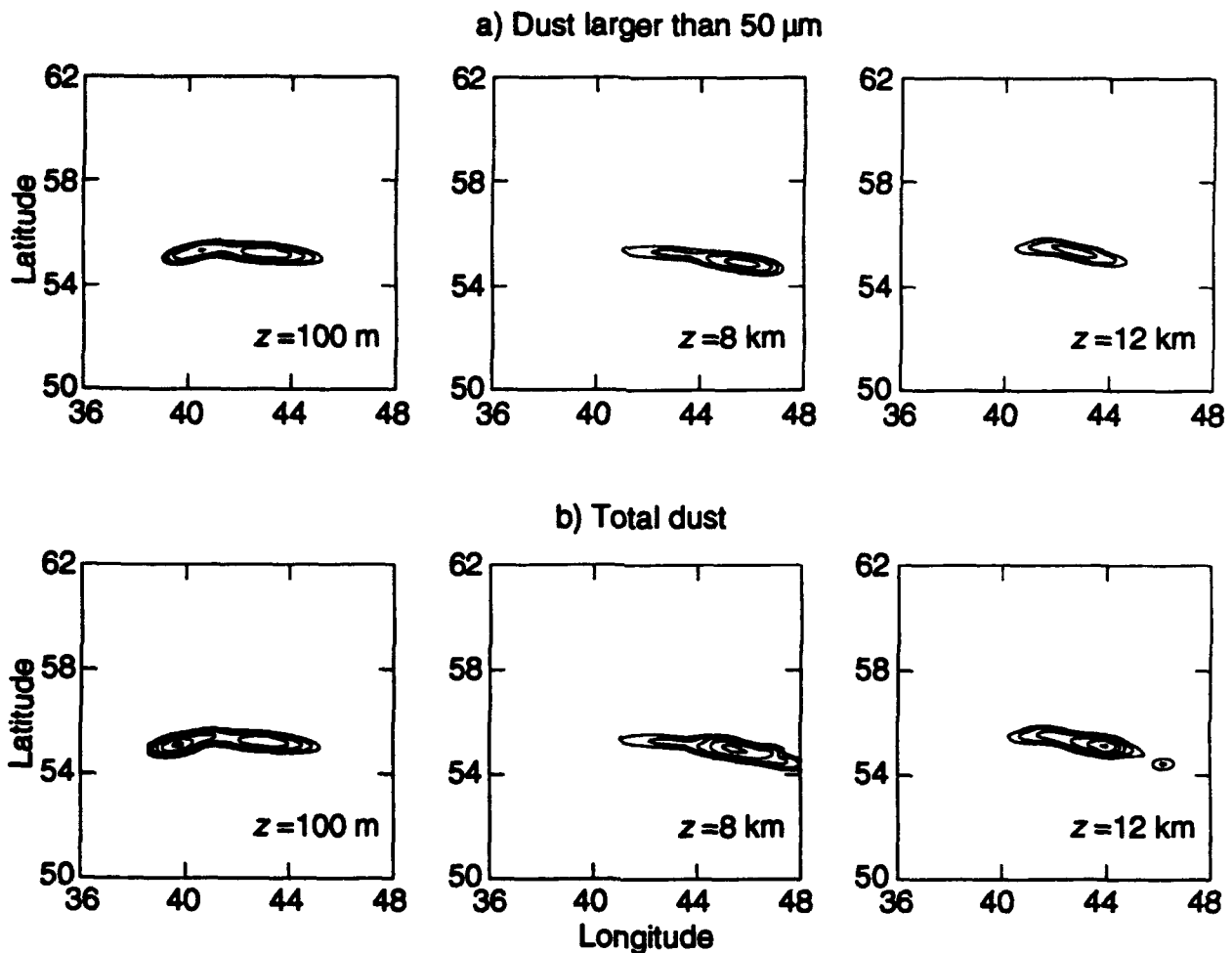


Figure 2-5. SCIPUFF results for the single burst scenario using the July wind field. Horizontal cross-sections at $t = 8$ hrs. Contour levels of 10^{-13} , 10^{-12} , 10^{-11} , 10^{-10} , 10^{-9} , 10^{-8} and 10^{-7} gm/cm³.

As noted earlier, the SCIPUFF predictions shown above were obtained using the relative diffusion model to facilitate comparison with deterministic predictions. However, the normal SCIPUFF prediction is an absolute diffusion estimate of the mean concentration together with a calculation of the expected variance about this mean. The absolute diffusion prediction shows a much wider spread, since all scales of eddies are included in the dispersion process which now represents positional uncertainty in addition to cloud diffusion. Figure 2-9 shows the $z=100\text{m}$ fields from the single burst test case with winter winds. The mean concentration contours in this figure can be contrasted with those in Figure 2-4. The increased diffusion is obvious, but Figure 2-9 also contains the r.m.s. fluctuation prediction and this is seen to be larger than the mean value, in general. This indicates a large uncertainty in the predicted concentration at any particular location

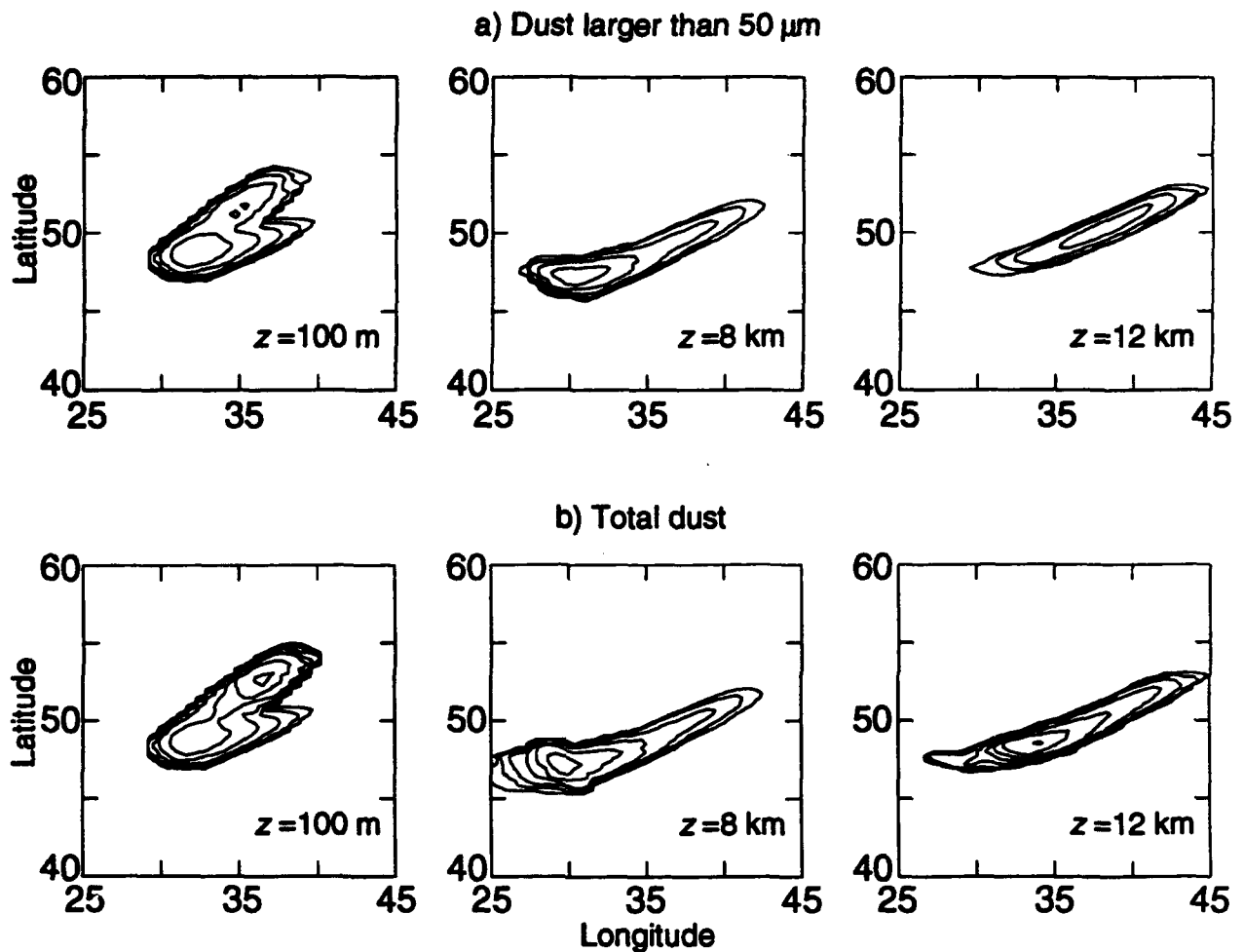


Figure 2-6. SCIPUFF results for the multi-burst scenario using the January wind field. Horizontal cross-sections at $t = 8$ hrs. Contour levels of 10^{-13} , 10^{-12} , 10^{-11} , 10^{-10} , 10^{-9} , 10^{-8} and 10^{-7} gm/cm^3 .

and should be interpreted as mostly due to uncertainty in position, i.e., the available wind information is not sufficient to reliably predict the cloud position relative to the actual cloud width.

The fluctuation intensity characterizes the random nature of the cloud, and this can be used to generate 'realizations' of the instantaneous concentration distribution. We use the statistical description together with a 'fractal' representation technique to generate a random field with an appropriate spatial structure. The random fields created by this technique possess the same statistical properties as the SCIPUFF prediction but other details must be assumed. Thus, we use a clipped normal representation of the probability

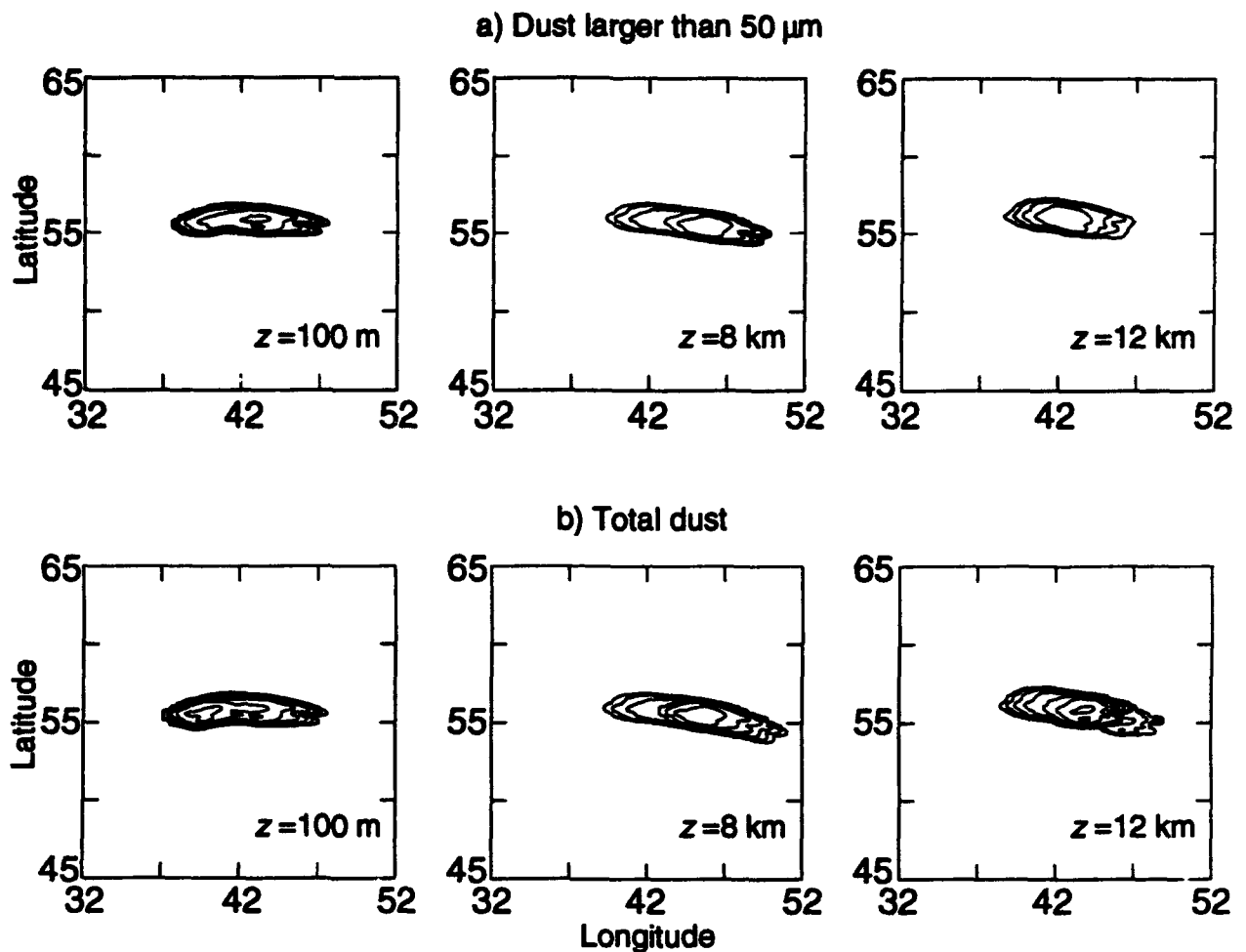


Figure 2-7. SCIPUFF results for the multi-burst scenario using the July wind field. Horizontal cross-sections at $t = 8$ hrs. Contour levels of 10^{-13} , 10^{-12} , 10^{-11} , 10^{-10} , 10^{-9} , 10^{-8} and 10^{-7} gm/cm^3 .

distribution function for concentration at any point, together with a spatial correlation scale based on the SCIPUFF prediction of the cloud scale, λ_c , and we also specify the fractal dimension of the field so that a concentration contour has dimension 1.3. The fractal dimension is based on estimates from atmospheric observations of natural clouds (Lovejoy, 1982). The fractal fields are intended to represent possible clouds from the ensemble of all possible clouds, and two examples are given in Figure 2-10. These fields were generated from the statistics shown in Figure 2-9 but are clearly very different from the average concentration field. The intermittent nature of the clipped normal distribution gives much smaller regions of high concentration. The concentration levels and areal coverage are broadly similar to the relative diffusion prediction in Figure 2-4, but

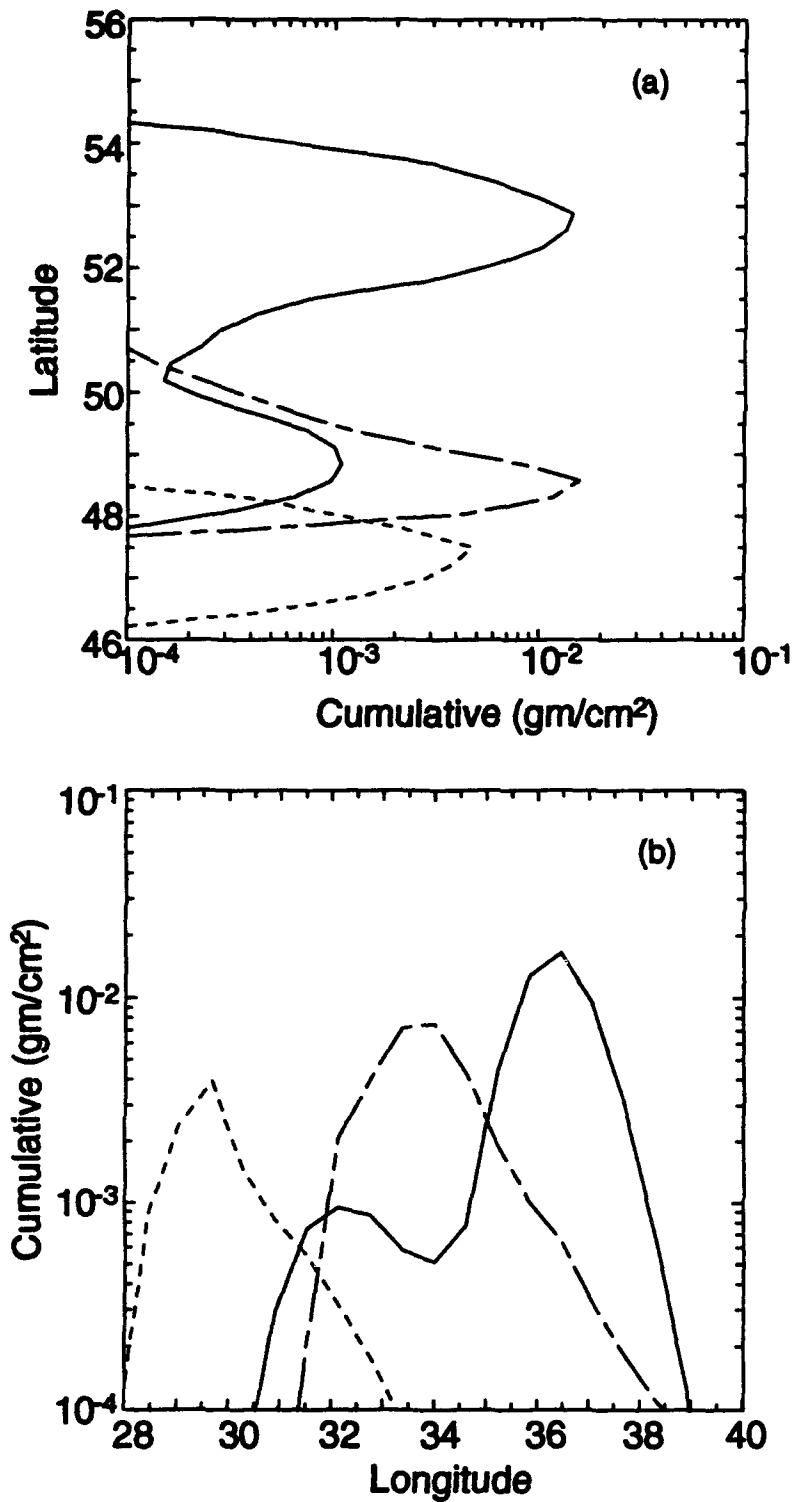


Figure 2-8. Intercepted dust masses along horizontal flight paths through the single burst cloud after 8 hours with winter winds. (a) East-West paths, (b) North-South paths. — $z=100\text{m}$;
 - - - $z=8\text{km}$; - · - $z=12\text{km}$.

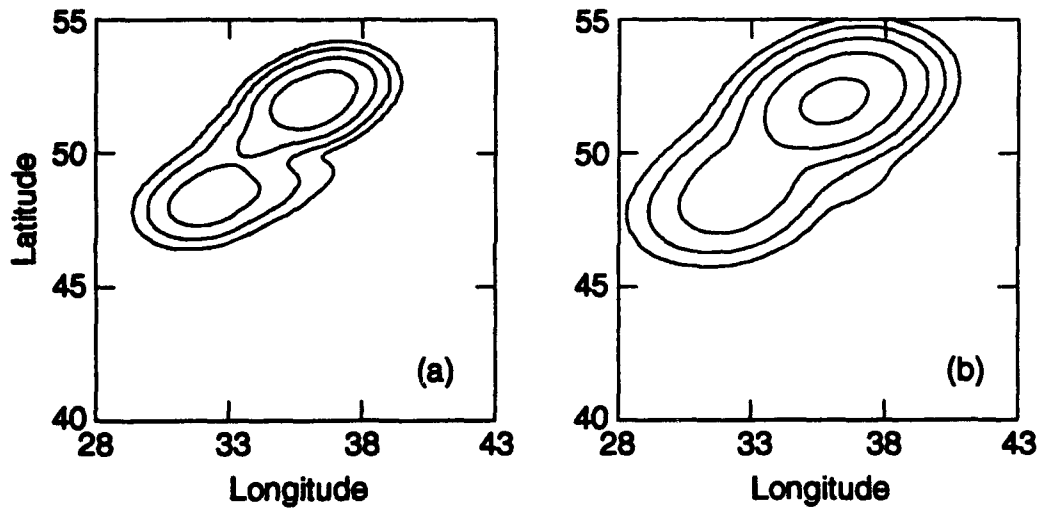


Figure 2-9. SCIPUFF results for the single burst scenario using the January wind field and absolute diffusion scheme. Horizontal cross-sections at $t = 8$ hrs and $z = 100$ m. (a) mean total dust concentration, (b) r.m.s. fluctuation in total dust. Contour levels of 10^{-13} , 10^{-12} , 10^{-11} , 10^{-10} and 10^{-9} gm/cm³.

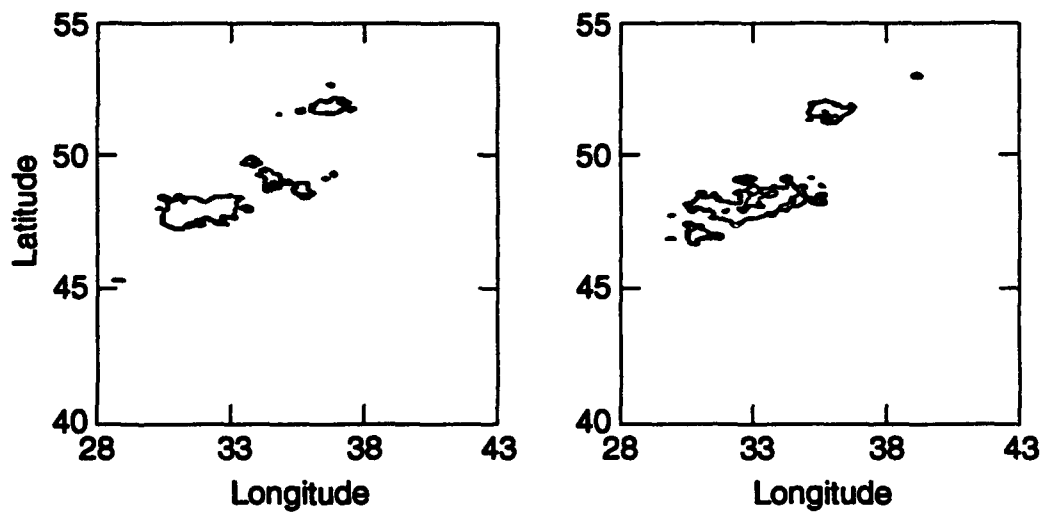


Figure 2-10. Fractal realizations from the ensemble statistics of Figure 2-9. Horizontal cross-sections at $t = 8$ hrs and $z = 100$ m. Contour levels of 10^{-13} , 10^{-12} , 10^{-11} , 10^{-10} and 10^{-9} gm/cm³.

the fields are much more complex due to the random nature of the variability. Unfortunately, the intermittency of the clipped normal distribution gives very sharp boundaries around the non-zero concentration regions, making it difficult to distinguish the logarithmic contour levels. However, the maximum concentration values in both realizations are close to 10^{-8} g/cc and occur in the region around 52°N 36°E, with levels roughly an order of magnitude smaller in the South-Western regions of the cloud.

SECTION 3

'ANATEX' MODEL EVALUATION STUDY

Model validation is a vital part of any program development but this has always been a difficult exercise for long range atmospheric dispersion models. Large scale atmospheric flow fields, with length scales ranging from hundreds to thousands of kilometers, cannot be simulated in the laboratory with sufficient verisimilitude for dispersion effects to be measured. We must therefore rely on field observations for model evaluation purposes. Field programs must deal with the inherent uncertainties of the wind field, which cannot be measured with enough detail for reliable trajectory calculations, and also with limited sampling of the tracer distribution over the large horizontal scales of interest. Most model evaluations are therefore restricted to qualitative comparison at continental scales.

The Across North America Tracer Experiment (ANATEX) was chosen to evaluate the SCIPUFF model predictions because it is an unusually complete study of *long-range transport and dispersion*. The wind field uncertainties are unavoidable, but the ANATEX data provides an exceptionally large data base for model evaluation at the scales of interest here. This is of particular value in evaluating a probabilistic dispersion model like SCIPUFF, where an assessment of the uncertainty in the prediction is made, since the comparison with observations can only be made on a statistical basis. ANATEX was conducted between January and March, 1987, under the auspices of NOAA (National Ocean and Atmosphere Administration). Specialized tracer materials were released from two sources in Montana and Minnesota in cycles of short duration over the period of the experiment. The tracers were detected on a network of 77 surface samplers, illustrated in Figure 3-1, covering the entire Eastern half of the United States and the Canadian Maritime Provinces. The samplers recorded 24-hour average concentrations throughout the experiment. In addition, three aircraft made direct sampling flights through the plumes within a few hundred kilometers of the source on a number of occasions.

Wind fields were provided by NOAA from the Nested Grid Model (NGM), an operational forecast model with a spatial resolution of about 100km over the continental United States. Three-dimensional wind fields were stored every 2 hours throughout the

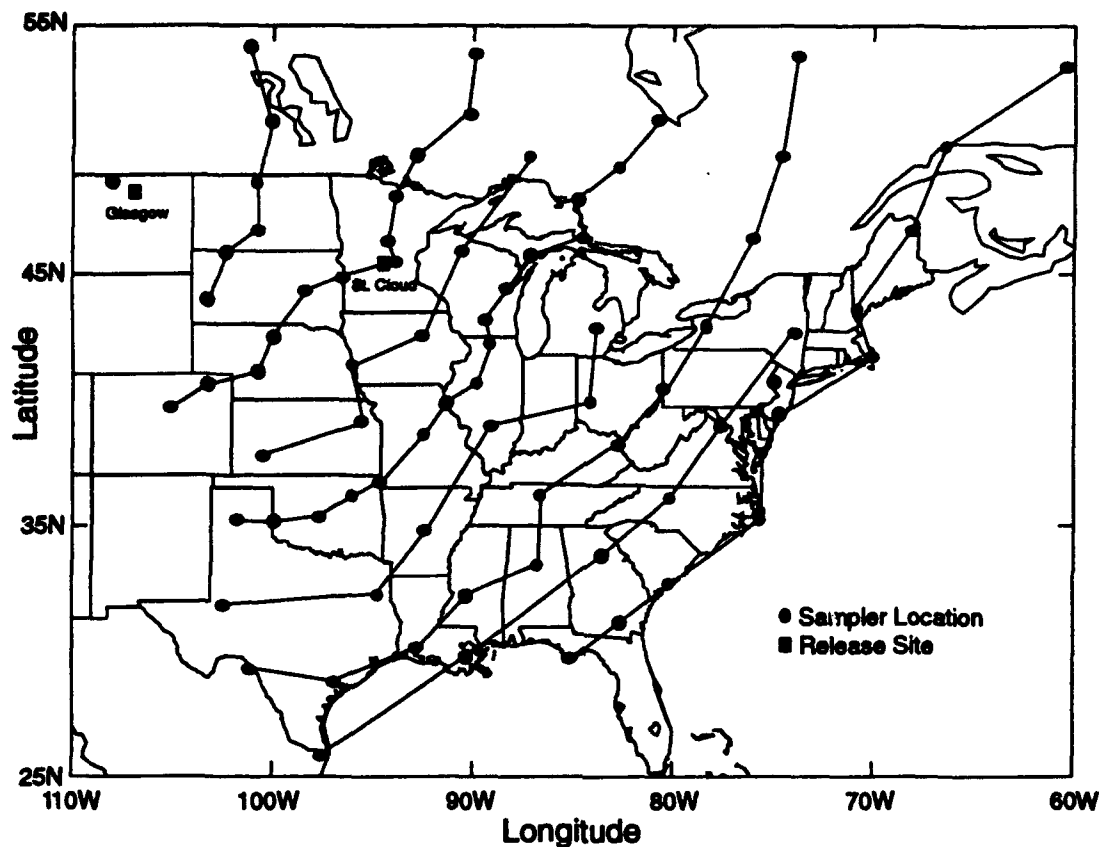


Figure 3-1. ANATEX release and surface sampler locations.

experimental period, with the exception of one week in March where the meteorological data is incomplete. The data was therefore divided into two parts, covering 7 weeks of January and February, and 3 weeks of March, where wind fields were available. SCIPUFF was run continuously for these periods, simulating the multiple releases from each of the two release locations, and tracking the total tracer concentrations over the Eastern U.S. A complete time history of the tracer concentrations at each surface sampler site was saved, and 24-hour averages were computed for comparison with the surface observations. In addition, tracer concentrations along the specified aircraft flightpaths were also saved for comparison with the direct sampling by the aircraft systems. The complete results from the validation study were published in the *Journal of Applied Meteorology*, and the paper is included as an Appendix to this report. The results will therefore only be summarized in this section, and the reader is referred to the Appendix for further details.

A typical comparison between the predicted surface concentration distribution and the observed values is shown in Figure 3-2. The general shape and magnitude of the surface concentrations is correctly predicted by the model, but detailed comparison of the concentrations at specific sampler locations is not very good. The reason for the poor correlation is mostly the inaccuracy of the cloud trajectory prediction. Small errors in the cloud position produce large discrepancies between the predicted and observed concentrations, even though the overall distribution may be very similar. This is a common problem in model evaluation, and various techniques have been developed to remove the effect of trajectory errors. One of the standard comparison statistics is the cumulative concentration distribution, i.e., the function $F(c)$ defined such that F is the fraction of the observations less than the value, c . The function can be defined for any subset of the observations to examine dependence on location or time, but the comparison becomes more meaningful for larger samples since the statistical uncertainties are reduced.

A comparison between the SCIPUFF predictions of the 24-hour average tracer concentrations over the whole network for the March period is shown in Figure 3-3. The agreement is seen to be good over the entire range of concentrations, indicating that the correct fraction of concentrations is predicted at each level. These predictions were obtained using the boundary layer description provided by NOAA, but results using this estimate were not as good for the January-February period. The NOAA estimates of the boundary layer depth appeared to be very low for this period, and a SCIPUFF prediction using a standard 1000m deep layer during the daytime gave much improved agreement. The comparison for individual sampler arcs is shown in Figure 3-4, illustrating that the range dependence of the concentration values is also correctly predicted. Further discussion of these results can be found in the Appendix.

The uncertainty in the 24-hour samples is mainly due to the trajectory differences arising from the numerical forecast errors. We have not attempted to model the random forecast errors, but have simply compared the cumulative distributions. The contribution from unresolved eddies (smaller than the 100km NGM grid) is insignificant in the surface tracer data since the 24-hour average is long enough to reduce these uncertainties to negligible proportions. This is not true for the short-term aircraft sampling, which is only a 6-minute duration. The uncertainty in these values was therefore a significant factor in the model evaluation. A direct comparison between the predicted and observed distributions showed a large overestimate of the number of trace (less than 1f/l)

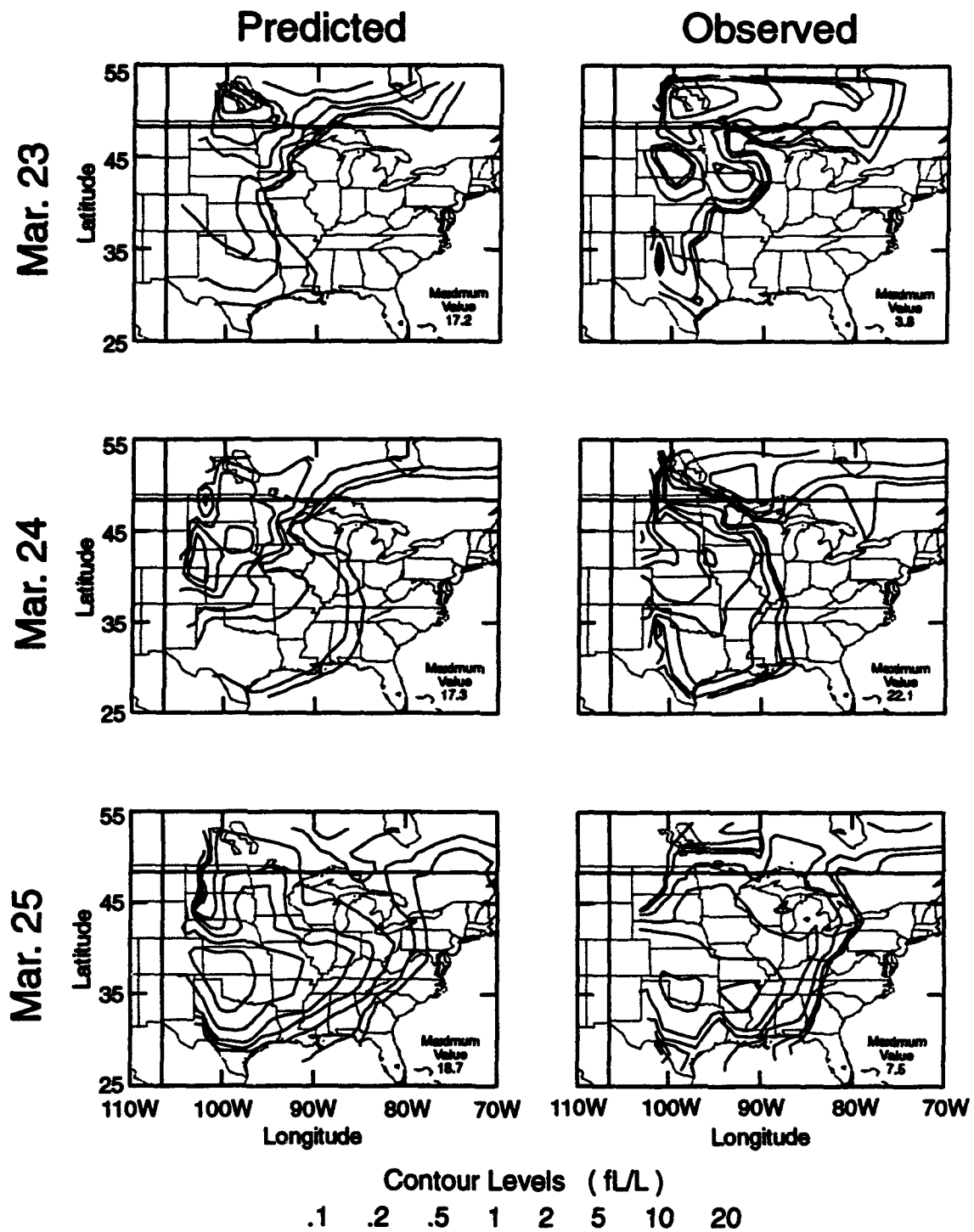


Figure 3-2. Comparison of the SCIPUFF 24hr average PTCH surface concentration patterns with the observed patterns for the period 23-25 March.

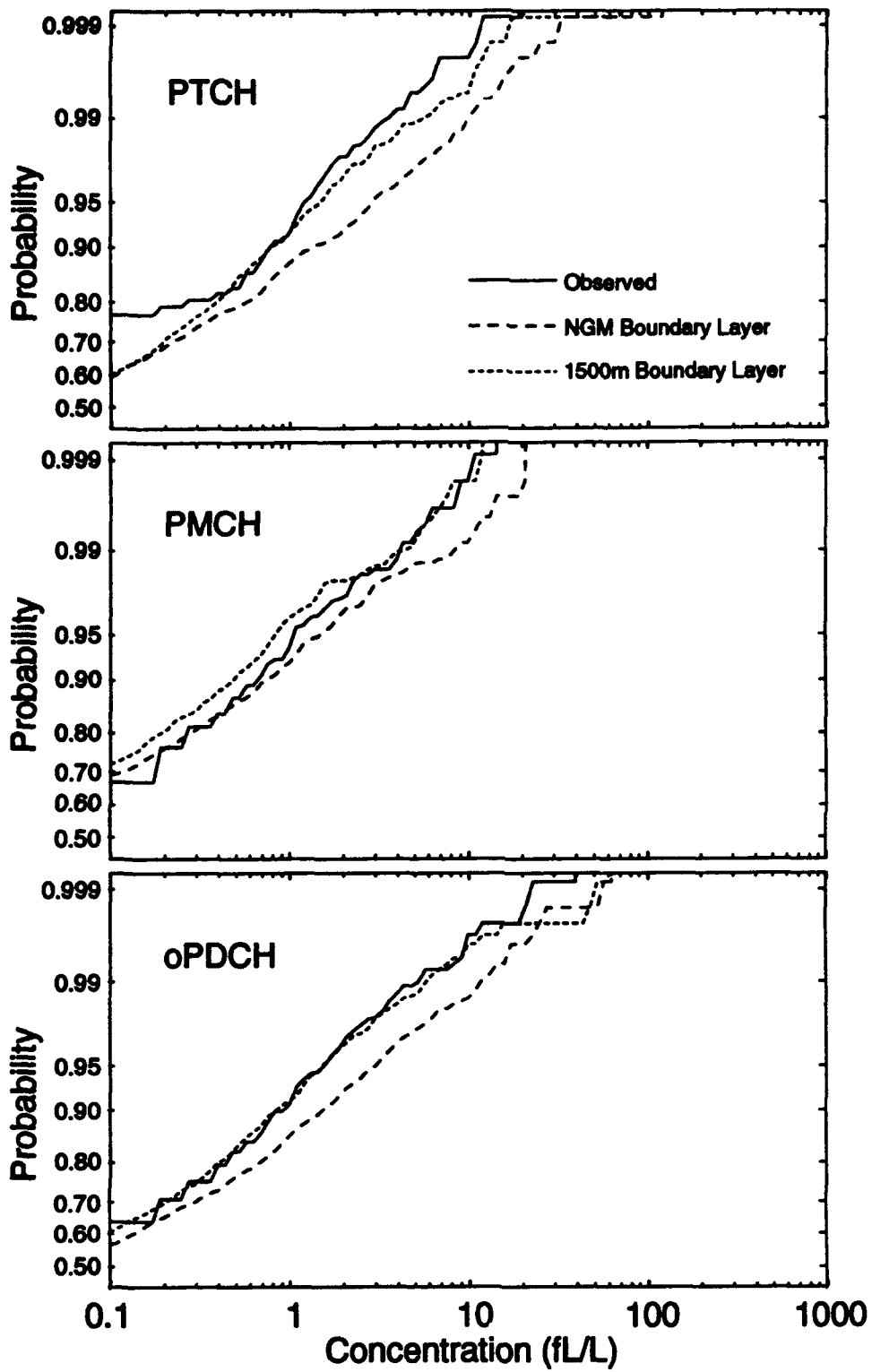


Figure 3-3. Predicted and observed ground sample cumulative distribution functions for the period 9-28 March.

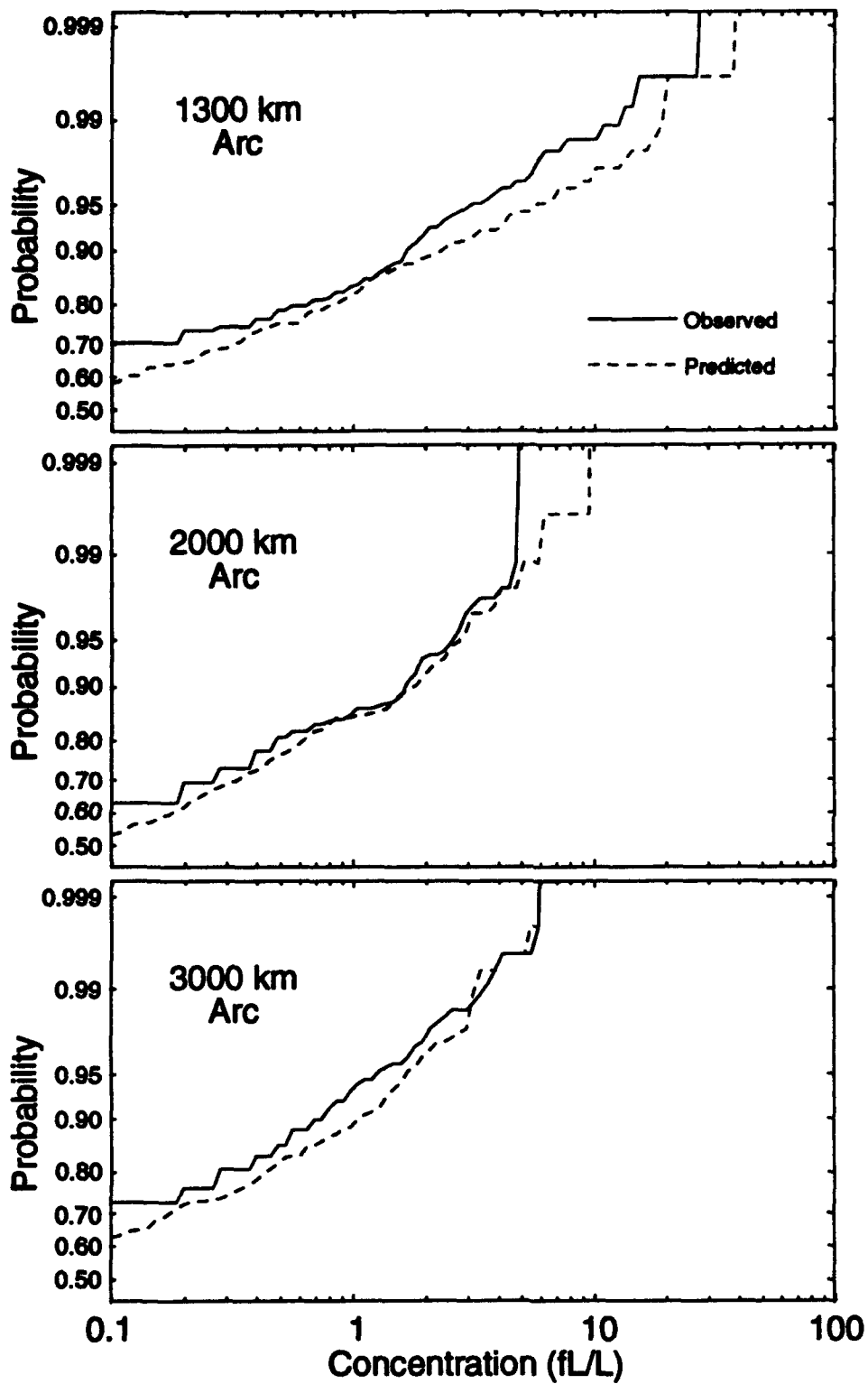


Figure 3-4. Predicted and observed ground sample cumulative distribution functions for PTCH along three arcs for the period 5 January-21 February. Predictions were made using a standard boundary layer depth of 1000m.

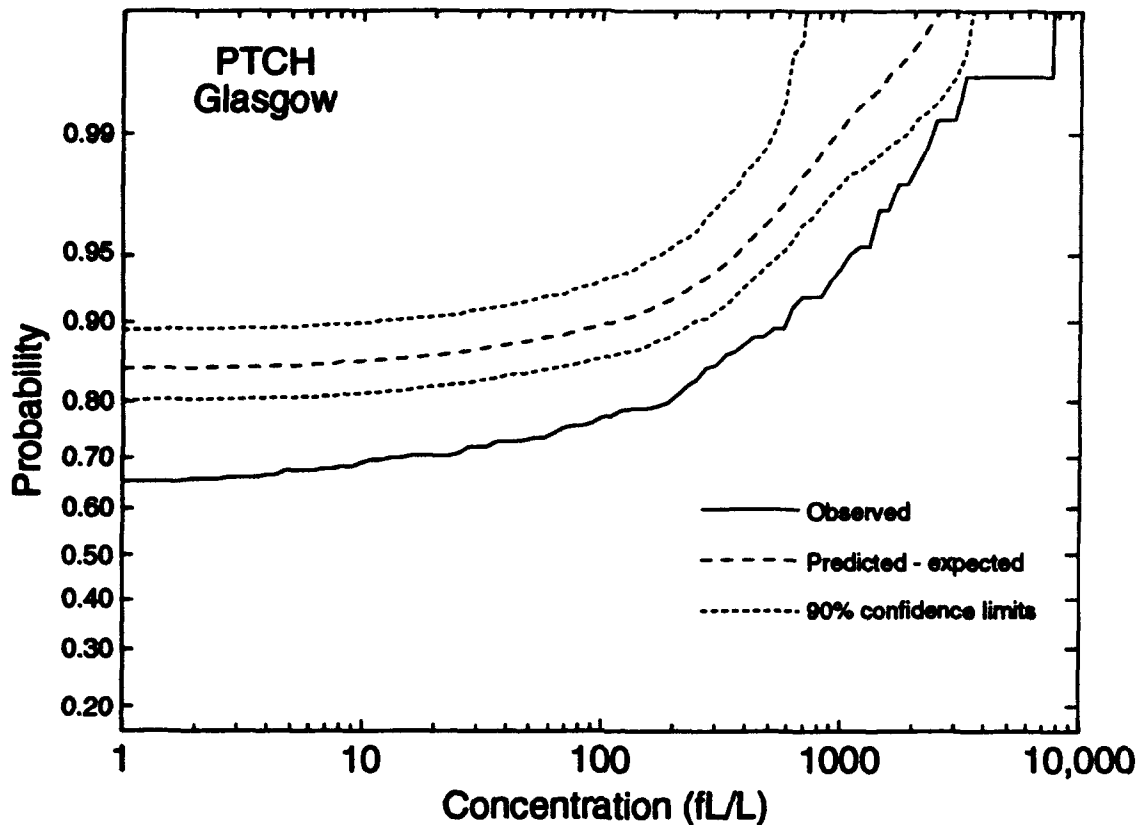


Figure 3-5. Predicted and observed aircraft sample cumulative distribution functions for the period 9-28 March.

concentration samples, as can be seen in Figure 3-5. The predicted confidence bounds are included in the figure, but it is clear that the observations lie well outside the acceptable range. A likely reason for the discrepancy is the non-random nature of the aircraft sampling; flights were made on the basis of forecast trajectories, with readjustment after initial samples were taken. We expect the aircraft to record fewer zero concentrations than a completely random sample, therefore, since there was a definite effort to locate the actual plume. We can only compare the distribution of non-zero concentrations, in this case, since the conditional probability of intercepting the plume cannot be accurately estimated. If we adjust the predicted zero fraction to match the observations we obtain the improved agreement shown in Figure 3-6, which is much more acceptable. Most of the observed distribution now falls within the predicted confidence bounds for the sample.

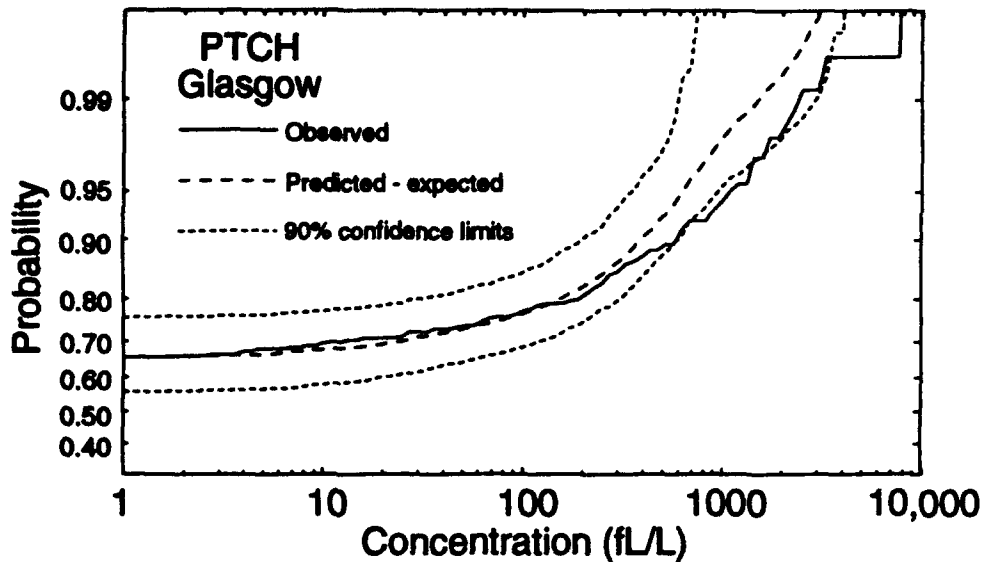


Figure 3-6. Adjusted predicted and observed aircraft sample cumulative distribution functions for the period 9-28 March.

As part of the ANATEX study, we also examined the possibility of predicting the expected distribution of concentrations based simply on the long term average wind statistics for the entire Eastern United States. There is no detailed information on the wind field, only average speed and direction as a function of altitude, together with a variance about the mean. The SCIPUFF prediction is compared with the surface sampler observations in Figure 3-7, and shows reasonable agreement considering the very limited information used as input. The model predicts a large uncertainty range, due to the very uncertain wind field input, so the expected concentration distribution is sampled from the predicted range with an assumed probability density function. For all our shorter range (less than 100km) predictions with shorter averaging times (up to 1 hour), we have found that the 'clipped-normal' distribution gives a good prediction, but the results in Figure 3-7 were obtained using a log-normal distribution. The clipped-normal gave too much intermittency and was unable to match the observations. There is some indication, therefore, that the longer averaging and transport times are more appropriately represented by a log-normal probability distribution. The results do indicate, however, that reasonable estimates of expected concentration values can be predicted with limited descriptions of the wind field. Particular events cannot be predicted without detailed information, but the correct probability of a particular event can be predicted.

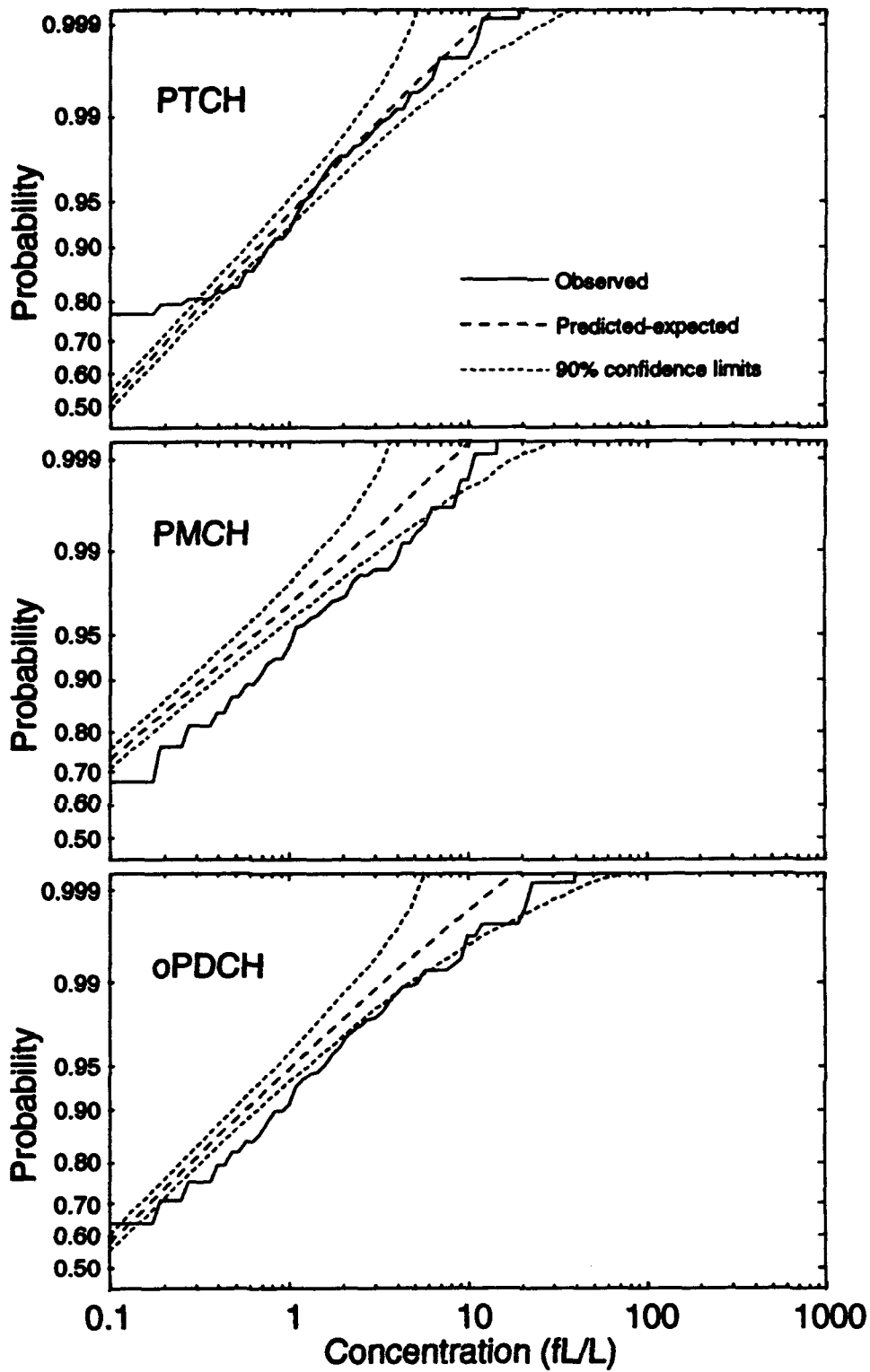


Figure 3-7. Predicted and observed ground sample cumulative distribution functions for the period 9-28 March. Predictions were made using the ensemble meteorology.

SECTION 4

BOUNDARY LAYER DIFFUSION EFFECTS

4.1 BACKGROUND.

The blast of a large nuclear weapon lofts large amounts of dust and ejecta high into the atmosphere. In addition to this high cloud of material, the strong winds near the surface, induced by the rapidly-rising fireball, scour loose material to form a broad pedestal of low-lying dust. The flow associated with the blast of the explosion also lofts the sand/soil particles, so that the pedestal can represent a significant fraction of the total mass of material injected into the atmosphere by the burst. The pedestal material is confined to a relatively shallow layer above the ground, but the action of turbulent eddies on the dust can lift it to heights of order 1km, which represents a typical mixing depth for surface-driven turbulence. The possibility that the large dust mass in the pedestal can remain within the surface mixing layer for periods of hours raises concern, and a more detailed study than has hitherto been undertaken is needed to answer questions about the importance of this phenomenon.

There are two basic physical mechanisms determining the evolution of the dust field in the lowest layers of the atmosphere; first, the turbulent eddies generated by heat input from the ground and by mechanical drag on the rough surface transport the particles through the air, and second, the deposition of the particles onto the ground. The first mechanism tends to maintain the particles in suspension, while the second is purely a reduction of airborne material. The relative balance between these two mechanisms depends strongly on the particle size. For large particles, i.e. larger than $100\mu\text{m}$, gravitational settling is the major deposition mechanism, and the turbulent eddy velocity must be compared with the equilibrium fall rate to determine the importance of turbulent convection on the particles. Typical eddy velocities are of the order of 0.5ms^{-1} , while particles of $100\mu\text{m}$ size have a terminal velocity of about 0.3ms^{-1} , so that particles larger than $100\mu\text{m}$ are unlikely to be prevented from falling for very long. This preliminary balance determines the size range of particles which can be influenced significantly by atmospheric boundary layer turbulence to be below $100\mu\text{m}$. For smaller particles the gravitational settling rate decreases rapidly with diameter, but under turbulent conditions

the most important deposition mechanism can be the impact of particles onto the surface roughness elements. Thus, a realistic examination of the response of the dust cloud under turbulent conditions needs to account for the turbulent deposition of the smaller particles.

In this study, we focus on the vertical distribution of the dust mass, i.e. we are not concerned with the horizontal transport and dispersion of the cloud. The conservation equation for the dust concentration can be integrated over the entire horizontal plane to eliminate the horizontal terms, and reduce the problem to a one-dimensional, time-dependent set of equations. The wind transport and horizontal diffusion only redistribute the mass in the horizontal, so that we can ignore these effects if we assume that the boundary layer is horizontally homogeneous and we are only interested in the vertical distribution. The one-dimensional results from this study will therefore give information on how fast the dust is removed from the atmosphere in an overall sense, and on the altitude dependence, but provides no guidance in assessing an actual local concentration level since this will depend on the horizontal redistribution.

The next section briefly describes the model equations used to represent the atmospheric turbulence and the surface deposition rate, together with the numerical techniques employed in their solution. Section 4.3 presents the results of the calculations, which cover a range of conditions, including wind speed, surface heating, surface roughness, time of release, and particle size spectrum. Finally, Section 4.4 discusses the results, and presents the general conclusions from the investigation.

4.2 NUMERICAL MODEL.

4.2.1 Turbulent Transport Model.

The model used in this study is based on turbulent dispersion research in the field of particulate transport from industrial sources. The basic turbulence model is derived from the second-order closure technique and a surface deposition formulation consistent with the turbulence closure is employed. Both models are fully described by Lewellen and Sheng (1980).

The particle size spectrum is represented by a number of discrete bins with no interaction between different size groups, so that the bins can be treated independently.

This neglects any particle agglomeration or break-up, although these mechanisms could conceivably be significant in the high density environment of the early cloud. However, a description of these effects is beyond the current state-of-the-art and is therefore omitted from the present study. Similar remarks apply to electrostatic effects, which could be important in the transport of very small particles, but very little is known about their role in the atmosphere.

We denote the (horizontally-integrated) concentration in a size group characterized by diameter, d_{α} , by $c_{(\alpha)}$, and write the conservation equation for $c_{(\alpha)}$ as

$$\frac{\partial \overline{c_{(\alpha)}}}{\partial t} = -\frac{\partial \overline{w'c'_{(\alpha)}}}{\partial z} + \frac{\partial v_{(\alpha)} \overline{c_{(\alpha)}}}{\partial z} \quad (4.1)$$

where the overbar denotes the Reynolds (or ensemble) average operator, and the prime denotes the random turbulent fluctuation about the average. The second-order correlation term is the turbulent flux of concentration, which is often parameterized as a diffusive flux proportional to the mean gradient in simple models. This assumption is inaccurate in some circumstances, especially in buoyancy-driven flows, and at best requires specification of an eddy diffusivity. The second-order closure technique derives a predictive equation for the turbulent flux itself, and seeks to rationally model the higher-order moments which appear in this equation.

The gravitational settling velocity $v_{(\alpha)}$, appropriate for the particle size, is determined from the balance between aerodynamic drag and gravitational forces, i.e.

$$\rho_d V g = \frac{\rho_a}{2} c_D A_p v^2 \quad (4.2)$$

where ρ_d is the dust density, ρ_a is the air density, V is the particle volume, A_p is the particle cross-section area, and c_D is the drag coefficient. The drag coefficient is a function of Reynolds number, $Re=vd/\nu$, where d is the effective particle diameter and ν is the kinematic viscosity of air, given by

$$c_D = \frac{24}{Re} (1 + 0.15 Re^{0.682}) \quad (4.3)$$

for $Re < 1000$, and held at a constant value of 0.424 for all larger Reynolds numbers.

The equation for the vertical concentration flux is written in the form

$$\frac{\partial \overline{w'c'_{(a)}}}{\partial t} = -\overline{w'^2} \frac{\partial \overline{c_{(a)}}}{\partial z} + \frac{\partial v_{(a)} \overline{w'c'_{(a)}}}{\partial z} + \frac{\partial}{\partial z} \left(v_c q \Lambda \frac{\partial \overline{w'c'_{(a)}}}{\partial z} \right) - A \frac{q}{\Lambda} \overline{w'c'_{(a)}} + \frac{g}{T_0} \overline{c'_{(a)} \theta'} \quad (4.4)$$

where q is the rms turbulent velocity fluctuation, Λ is the turbulence length scale, g is the gravitational acceleration, T_0 is the reference temperature for the Boussinesq approximation, and θ' is the temperature fluctuation. A and v_c are dimensionless empirical constants used in the turbulence modeling, and take the values 0.75 and 0.3 respectively. It can be seen that the boundary layer turbulent velocity fluctuations appear directly in the concentration flux equation. The boundary layer dynamics are computed along with the dust equations, so that the diurnal variation of the turbulence is correctly included in the calculation. The details of the diurnal meteorology as specified for this study will be given below.

4.2.2 Turbulent Deposition Model.

The deposition of small particles onto the surface can be modeled using a turbulent deposition velocity, v_d , which augments the gravitational deposition velocity, $v_{(a)}$. The additional flux of concentration onto the surface due to turbulent transfer is then written as the product of the near-surface concentration and the turbulent deposition velocity, which depends on the character of the surface, the particle size, and also on the turbulence. We use a relatively simple description of the surface in terms of a single roughness length in this study; e.g. a forest is represented by a large roughness length compared with a smooth surface such as desert sand. The large roughness length not only increases the surface drag, and hence the turbulence intensity, but also produces a more efficient scavenging of the small particles as they are swept through the roughness elements (i.e. leaves in the forest case).

The specific form of the turbulent deposition velocity is obtained from the work of Lewellen and Sheng (1980). We base the formulation on the passive scalar flux rate, modified as appropriate for finite particle size. Thus we write

$$v_d = \frac{c_\theta \bar{u} P_s}{1 + P_s} \quad (4.5)$$

where \bar{u} is the mean wind at a reference height (the lowest model grid-point in our numerical integration), c_θ is the bulk transfer coefficient for a passive scalar, and P_s ,

represents the particle size effects. c_θ depends on the surface roughness, and the Monin-Obukhov length, which is a measure of the buoyancy forces in the turbulent transfer process.

The particle effects are modeled as

$$P_s = 0.8 \frac{\left[(D/\nu)^{0.7} + 0.1 \frac{u_*^2 \tau_v}{\nu} (1 - e^{-0.08 q^2 \tau_v / \nu}) \right]}{(1 + q \tau_v / \Lambda)^2} \quad (4.6)$$

where D is the particle diffusivity due to Brownian motion (from Friedlander, 1977), ν is the molecular viscosity of air, q is the rms turbulent velocity, u_* is the surface friction velocity, and Λ is the turbulence length scale. τ_v is the particle response timescale and is obtained from the drag law, so that

$$\tau_v = \frac{4\rho_p d}{3\rho_a c_D q} \quad (4.7)$$

where the Reynolds number is based on q . The turbulent velocity scale is used in this definition since we are primarily interested in modeling the response of the particle to the turbulent eddy field. We note that for small particles with small Reynolds numbers, the timescale is independent of q and depends only on the fluid properties and the particle size and density.

The physics of the turbulent particle deposition model are governed by the balance between the inertial effects of the particles in the accelerating turbulent field and Brownian motion effects. Very small particles are diffused across the viscous sublayer onto the surface, while larger particles are impacted inertially onto the surface elements. Examples of the variation of turbulent deposition velocity with particle size are shown in Figure 4-1, and compared with the gravitational settling velocity. These results are computed for a reference height of 10m, and surface friction velocity of 0.4ms^{-1} and a particle density of 2g/cc . Two surface roughness values are shown, and it can be seen that the turbulent deposition only slightly exceeds the gravitational term for the low roughness case, and this occurs only for particle diameters between about $5\mu\text{m}$ and $20\mu\text{m}$. For the high roughness case, however, the turbulent deposition is almost a factor of ten larger than gravitational settling for $10\mu\text{m}$ particles, and is the principal deposition mechanism for sizes between $2\mu\text{m}$ and $40\mu\text{m}$. The deposition velocities are of the order of a few cms^{-1} for particles above $10\mu\text{m}$ in the high roughness case. These velocities increase with increasing friction velocity, i.e with wind speed.

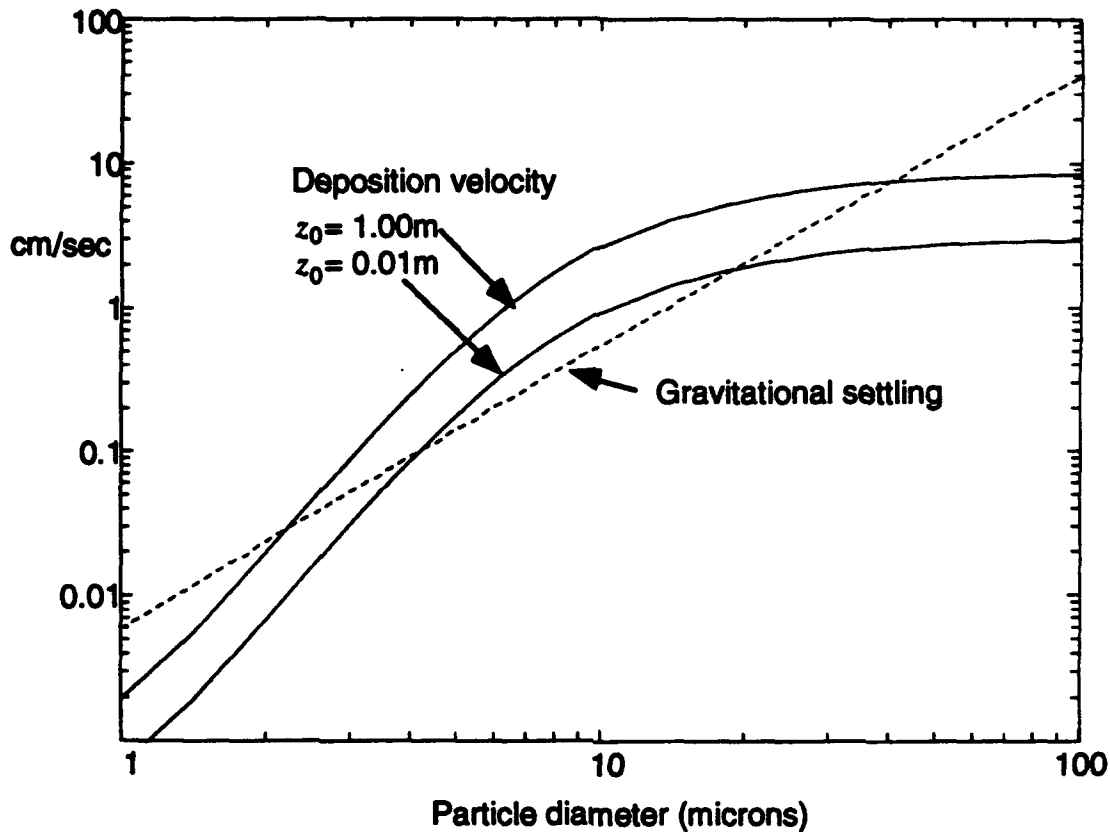


Figure 4-1. Surface deposition and gravitational settling velocity versus particle diameter for two surface roughness lengths. Surface friction velocity is assumed to be 0.4m/s, and the deposition is calculated for a height of 10m.

4.2.3 Initial Conditions.

The numerical integration is initialized with the dust distribution from a DICE calculation at $t = 5$ min. for a 1MT burst at a scale height of 200sft. The DICE computation (Hassig et al., 1992, p25) was made with a very fine grid near the surface, in order to resolve the sweep-up of the pedestal dust and follow its evolution for the first 5 minutes. The DICE computation was also concerned with the larger size ejecta, so that only one particle size group was devoted to the sub-100 μ m sizes, and at 5 minutes this is the only group with significant mass remaining in the air. The spatial distribution of the mass in this group is given in Figure 4-2, which shows the cloud extending up to about 15km, with a shallow pedestal out to about 5km horizontally. The primary focus of the DICE calculation was to examine the near-surface dust layer, and the increased diameter

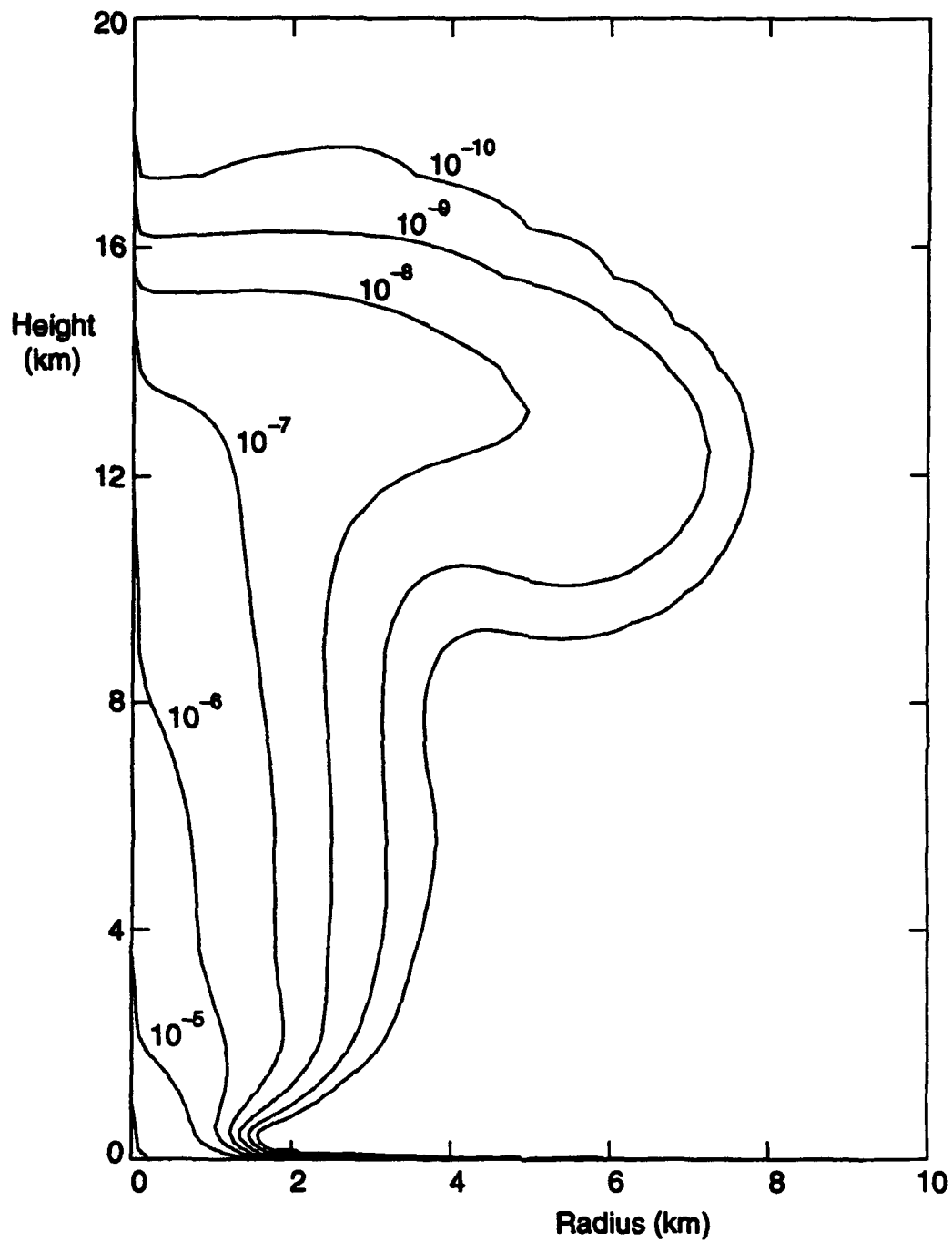


Figure 4-2. Dust field from DICE at $t = 5$ mins. Contours are in g/cc.

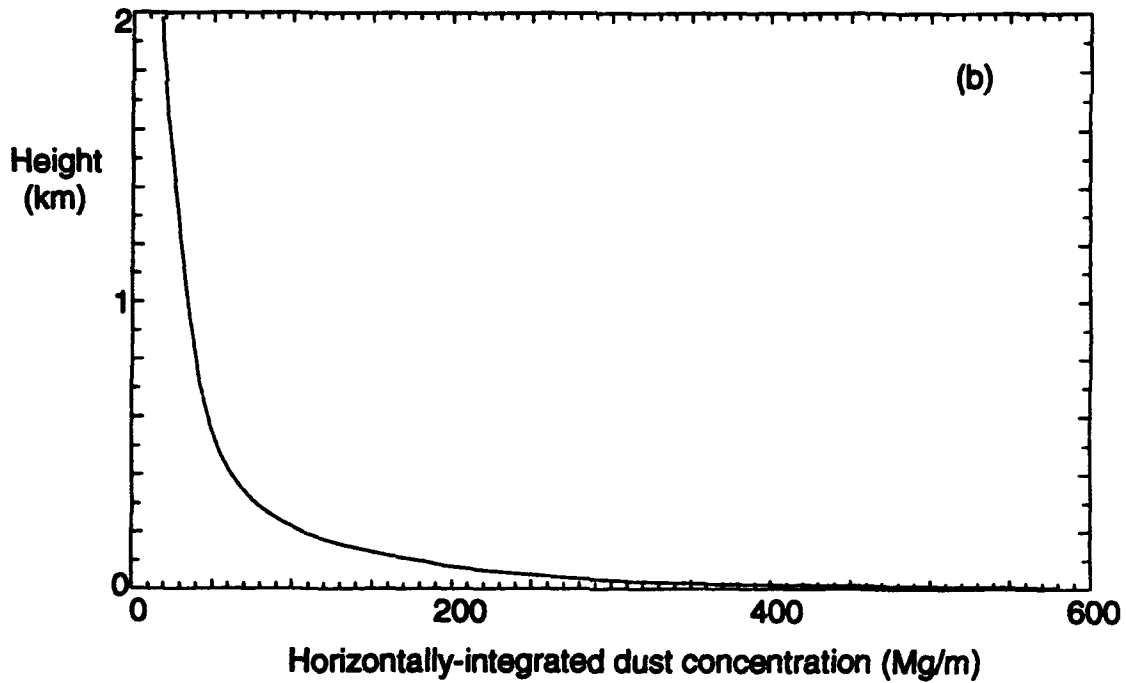
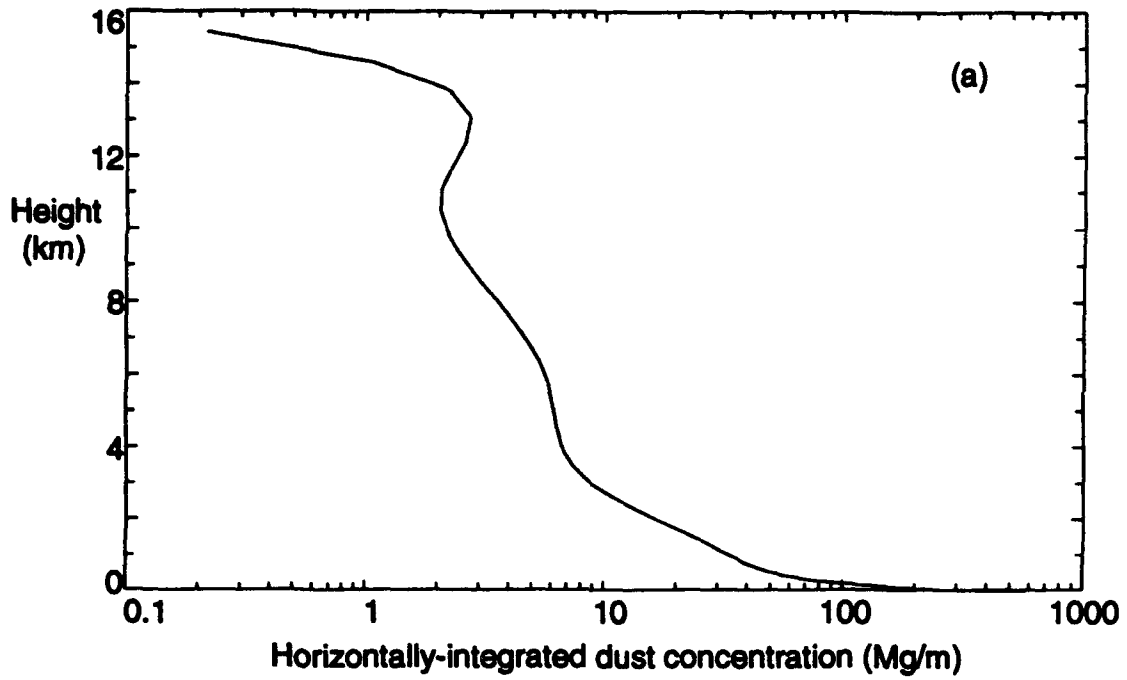


Figure 4-3. Vertical profiles of horizontally-integrated dust concentration from the DICE run at $t=5$ mins. (a) shows full profile (note logarithmic concentration scale), (b) shows detail in the lowest levels.

of the cloud stem above the 500m height is due to increased diffusion - both numerical and parameterized turbulence. Above about 200m, both vertical cell size and turbulence mixing length increase with altitude. The horizontally-integrated mass distribution, used to initialize the boundary layer calculation, is given in Figure 4-3. It can be seen that the highest densities are near the surface, but the extent of the high density is only about 100m in the vertical. The dust distribution does extend high into the atmosphere, however, and over the long period of the integration this dust can influence concentrations in the boundary layer through gravitational settling.

We avoid specifying detailed size distributions at this stage by using a normalized dust density for a range of particle size bins. In fact, we initialize 7 bins spanning the range from 1 μ m to 100 μ m with logarithmic spacing. The particle size bins evolve independently, i.e. the concentration in one bin is not affected by concentrations in any other bin, since we ignore any change in particle size due to agglomeration or fracture. We can therefore renormalize the dust concentrations to simulate any desired initial size distribution, subject only to the constraint that the total initial mass matches the DICE mass field.

The most commonly used size distribution is the a^{-4} spectrum, where a refers to the particle radius. This power law applies to the number density, so that the actual mass spectrum follows an a^{-1} law, since the particle volume is proportional to a^3 . Most of our results will be based on this distribution, but we will examine the importance of the particle size, providing guidance on the sensitivities.

4.2.4 Meteorological Parameters.

Results were obtained for a range of meteorological conditions, in an effort to gain some information on the possible range of variations in the dust field. Ambient conditions, such as wind speed, surface heating, and surface roughness are expected to play a role in the dust field evolution, as is the time of release in relation to the diurnal variation. We have computed a matrix of cases; two geostrophic winds were considered, 10ms⁻¹ and 2ms⁻¹, and two surface roughness lengths were used, a 1m roughness representative of a forest-type surface, and a 1cm roughness typical of a smooth desert-type surface. Two surface heating rates were also considered, a high value of 0.275°Kms⁻¹ (approximately 300Wm⁻²) and a low value of 0.075°Kms⁻¹; these are maximum daytime heating rates, with the high value being typical of a clear summer day,

and the low value more appropriate for a cloud-covered situation. For all the cases considered, four initializations were made at 6 hour intervals from midnight to determine the effect of time of day of release on the dust evolution.

The surface heating is specified as a sinusoidal variation during the daylight hours, i.e. from 06:00 to 18:00 local time, with a small constant negative heat flux at night. We have not considered variations in the length of the day, since we expect the specified parameter variations to dominate the response. The periodic surface heating allows the calculation to be run for several days, so that a near-periodic diurnal boundary layer can be developed. The boundary layer is not perfectly periodic because the net heat input during a 24 hour period is positive, i.e. more heat is input during the day than is lost at night. This imbalance causes the mixed layer to grow a little deeper each day as it steadily warms and erodes the overlying stable atmosphere. The relative change from one day to the next is small, however, and does not significantly affect the dust transport. The actual surface energy balance at night is a complex interaction between turbulent flux, radiative fluxes and heat flux from the soil or subsurface, which determines the nocturnal boundary layer structure. We have simply specified a constant cooling at night, however, but the variation of external parameters considered covers the range of nocturnal boundary layer behavior.

All the boundary layer integrations were initialized with an idealized wind profile, but were run for 3-5 days to allow the establishment of a reasonably periodic diurnal profile. The dust releases were made into the established boundary layer at 00:00, 06:00, 12:00 and 18:00 local time, where 12:00 represents maximum surface heat input, and 06:00 and 18:00 represent sunrise and sunset respectively. A typical variation of the vertical turbulence energy component for a 2 day period is shown in Figure 4-4. These results were obtained following a 5 day initialization period, and clearly show the suppression of turbulence during the night. Shortly after sunrise, when the surface heat flux becomes positive, a relatively slow growth of the turbulence, both in depth and intensity is visible, as the heating erodes the surface-based inversion formed during the night. At about 10:30 local time, the mixing reaches the top of the nocturnal inversion and grows very quickly through the remnant of the previous day's mixed layer to reach a depth of about 1200m. The boundary layer grows very slowly for the rest of the day, with slowly decaying intensity after 12:00 until the surface heating becomes negative about 18:00 and the turbulence collapses. This behavior is closely repeated on the second day with a boundary layer roughly 100m deeper.

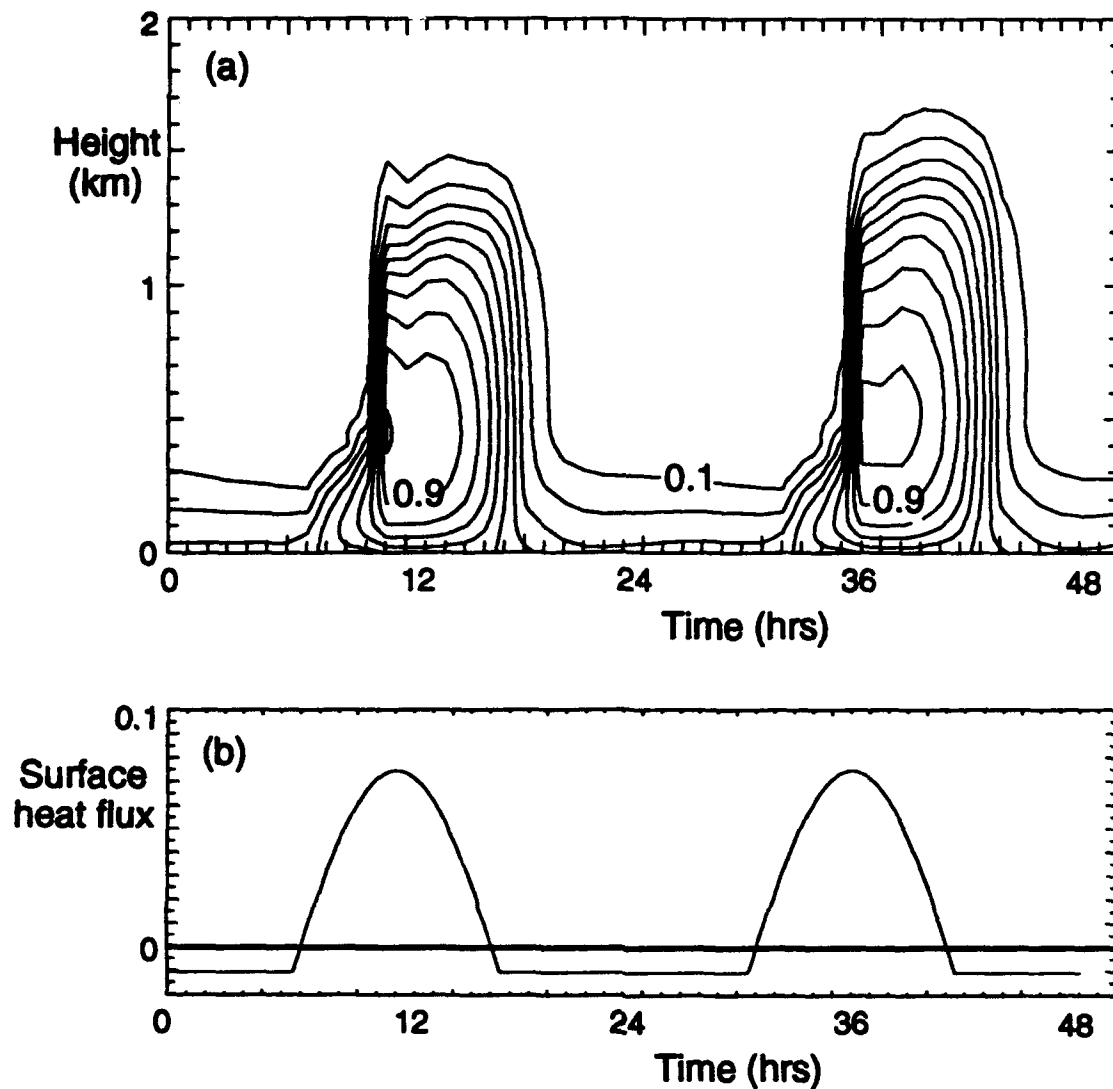


Figure 4-4. Diurnal variation of the planetary boundary layer.
 (a) r.m.s. vertical velocity fluctuation, contour interval 0.1 m/s
 (b) surface heat flux in K/s

All the mixing layers used in this study were between 1000m and 1500m deep, which is a typical range for convectively mixed layers. It is certainly possible for deeper mixing to occur, but 2000m is a reasonable extreme value for inversion-capped mixing. For shallower layers, it is possible for large-scale subsidence to prevent mixed layer growth,

but layers below 500m are very unusual under conditions of positive surface heating. These extreme values would modify the dust concentration results somewhat, so that a well-mixed value would be proportionally higher in a shallow layer.

4.3 RESULTS.

Figure 4-5 shows the concentration profiles at 4, 8, and 12 hours after release for the four initial start times with $U_0 = 10\text{ms}^{-1}$, $z_0 = 0.01\text{m}$, and $H_{\text{max}} = 0.075^\circ\text{Kms}^{-1}$ ($\sim 100\text{Wm}^{-2}$). The initial particle size distribution is α^{-1} , and the multiple lines indicate cumulative total up to the various size groups, which are represented by nominal particle diameters of 1, 2, 6, 10, 20, 60, 100 μm . These particle sizes can be considered as the mass mean diameters (MMD) of 7 size bins, with boundaries at 1, 1.4, 3.5, 7.8, 14, 35, 78, and 144 μm . The MMD of the smallest size group is actually 1.2 μm , not 1 μm , but the size distribution is truncated at 1 μm and the discrepancy is not significant for the deposition processes considered in this section. Thus the leftmost line in Figure 4-5 gives concentration in the 1 μm group (between 1 and 1.4 μm), the next is concentration in the 1 μm and 2 μm groups (between 1 and 3.5 μm), while the rightmost line gives total concentration for all size groups. The boundary layer mixing during the daytime hours is very evident in this figure, which shows a well mixed layer reaching depths of about 1.5km in the afternoon. At 4 hours after release, three of the four cases show roughly the same maximum level, namely 80-100 Mg/m, but it is clear that the noon release has produced a deep mixed profile and reduced the mean concentration by about a factor of 2. The other release times are confined closer to the surface and the initial concentration is only modified by the gravitational settling of the larger particles.

At later times the boundary layer mixing has made its appearance in more of the cases, so that at 12 hours after release there is strong similarity between the 00:00, 06:00 and 12:00 release cases. The 18:00 release evolves through the nocturnal hours during this period, and is still shows a shallow maximum, although the turbulence induced by the 10ms^{-1} wind does mix the material up to about 300m depth. The other three cases have all undergone at least one half of the daily mixing cycle, and show very similar profiles with an almost constant total concentration of about 35Mg/m. The 12:00 release does show a more pronounced surface minimum at 12 hours since the deposition removes the lowest layers of dust and there is no replenishment from above due to the limited vertical extent of the turbulence in the nocturnal hours. The preferential loss of the larger

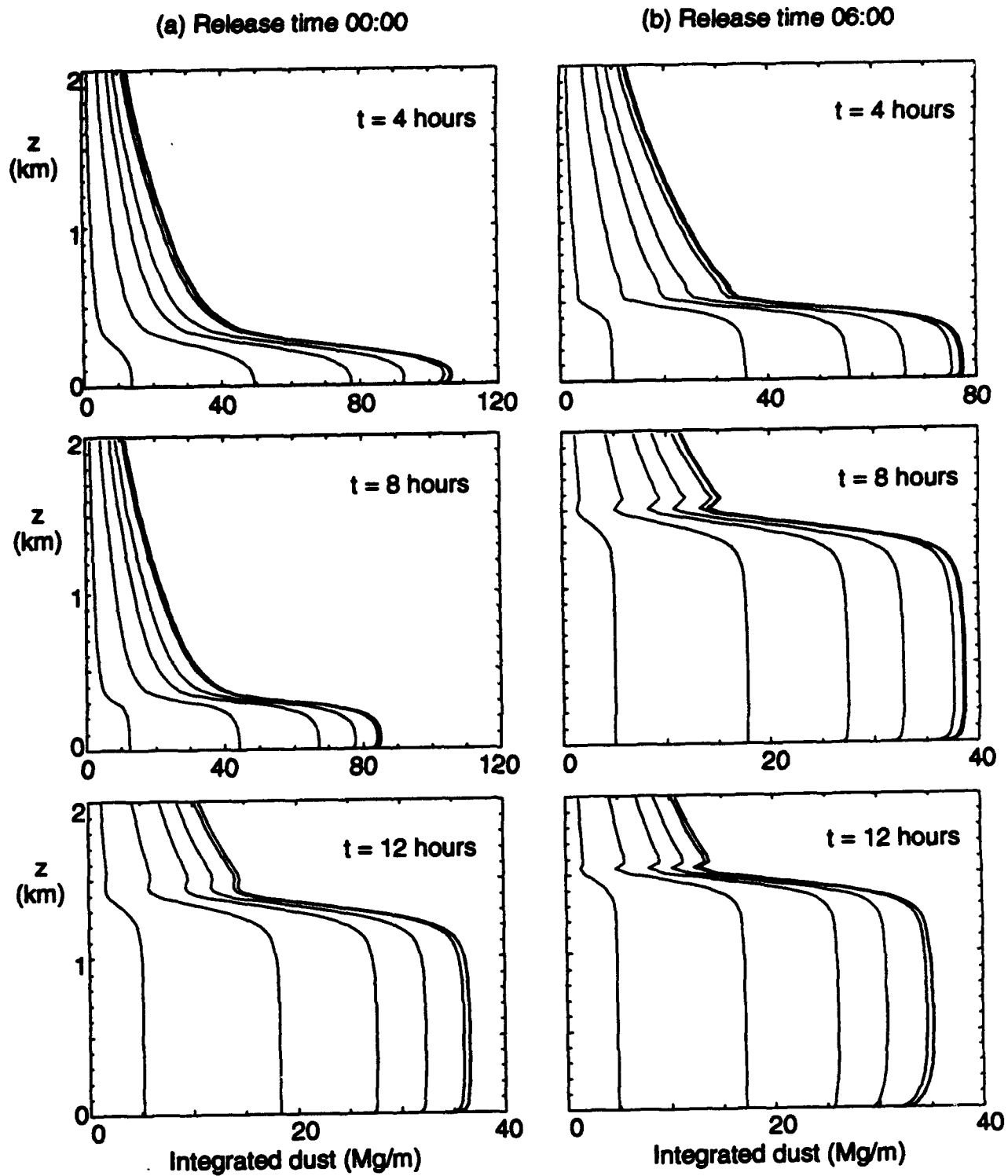


Figure 4-5. Integrated dust profiles at 4, 8, and 12 hours after release. Release is at (a) 00:00; (b) 06:00; (c) 12:00; (d) 18:00. Wind speed 10m/s, roughness length 0.01m.

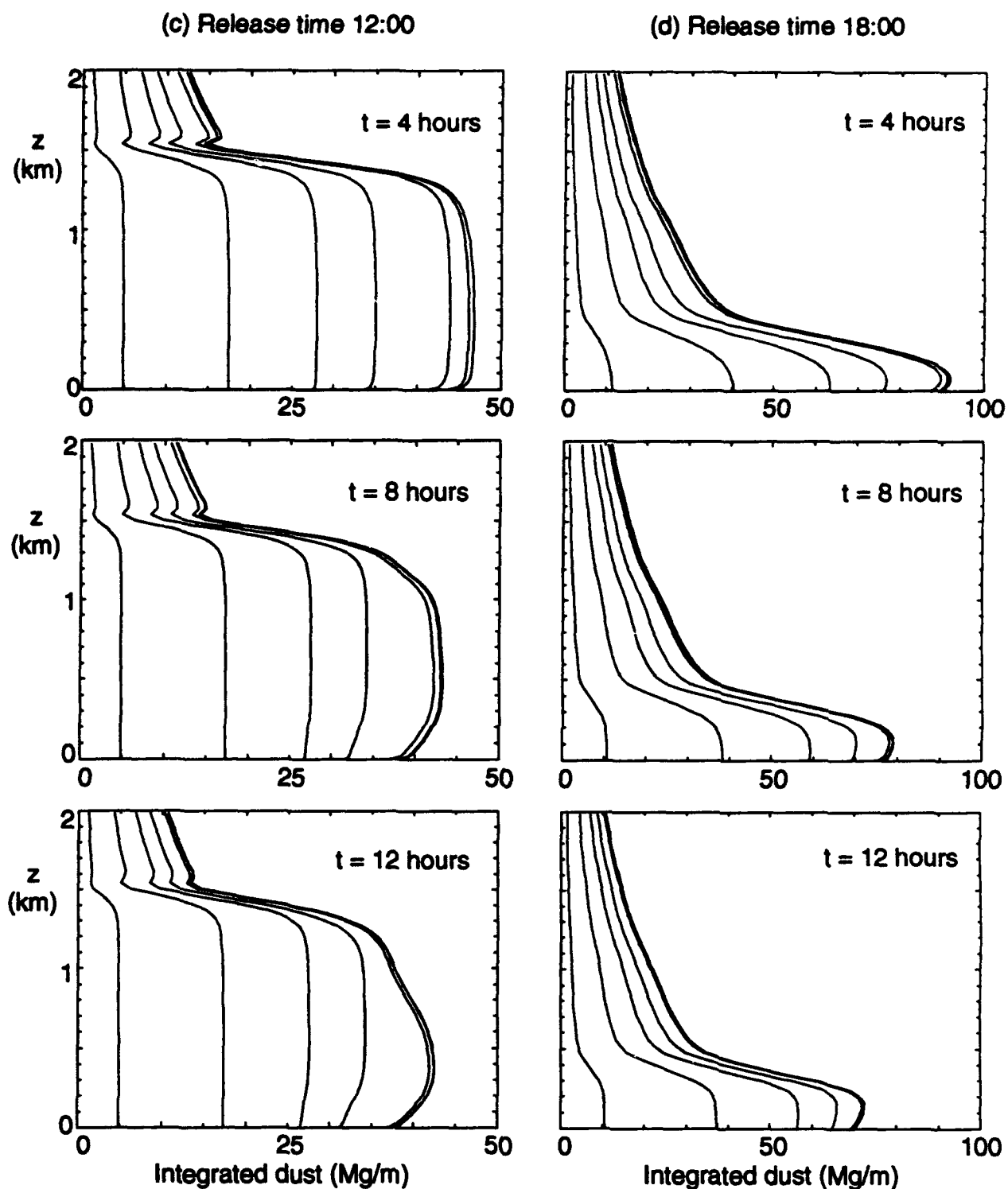


Figure 4-5. Integrated dust profiles at 4, 8, and 12 hours after release. Release is at (a) 00:00; (b) 06:00; (c) 12:00; (d) 18:00. Wind speed 10m/s, roughness length 0.01m (Continued).

particle groups is also evident in the results at 12 hours, with the fraction of the dust in the rightmost bands being reduced. It is clear, however, that most of the reduction occurs in the first 4 hours, as the larger particles fall out relatively quickly. Almost all of the mass is contained in the lowest 5 size groups, i.e., particle diameters less than $35\mu\text{m}$, after 4 hours of evolution.

Increasing the surface roughness to 1m , but holding all other factors the same, produces the dust profiles in Figure 4-6. There are two main differences induced by this change; first the nocturnal boundary layer is much deeper, so that the pedestal is mixed higher at all times, and second the deposition is larger, so that the concentrations in the lowest 1km at 12 hours after release are slightly less than those in Figure 4-5. The differences are not large, however, since the bulk of the remaining material is in the small size groups, which still have small deposition velocities. The surface minimum is more pronounced in this case, indicating the stronger removal mechanism at the rough surface. The nocturnal turbulence is generated by the relatively high wind speeds in Figure 4-6. This can be seen in Figure 4-7, which shows the same high roughness length, but has a wind speed of only 2ms^{-1} . In this low wind case, the turbulence is quenched almost down to the surface at night, so that the initial profile evolves over 12 hours due only to gravitational settling in the 18:00 release case. For other release times, however, the daytime mixing produces profiles at 12 hours which are similar to the high wind speed case, but with slightly higher values due to the reduced turbulent deposition rate.

Some indication of the range of profiles is given in Figure 4-8, which shows profiles at 12 hours after an 06:00 release under various meteorological conditions. All the cases show a mixed layer development, with low level concentrations ranging from roughly 20 Mg/m to 35 Mg/m . This narrow range is representative of the complete extent of the results from our matrix of release times, wind speeds, etc. The high wind speed, high roughness length case shows visible evidence of surface deposition, with a detectable low level minimum. The relatively small variation with meteorological parameters is due to the similarity of the mixing history over a 12 hour period between the various cases, together with the small deposition rates for the small particles. The general conservation of the small particle mass ensures that the mixed layer density is always about the same, and since all our mixing layers are roughly the same depth we obtain the same final concentration.

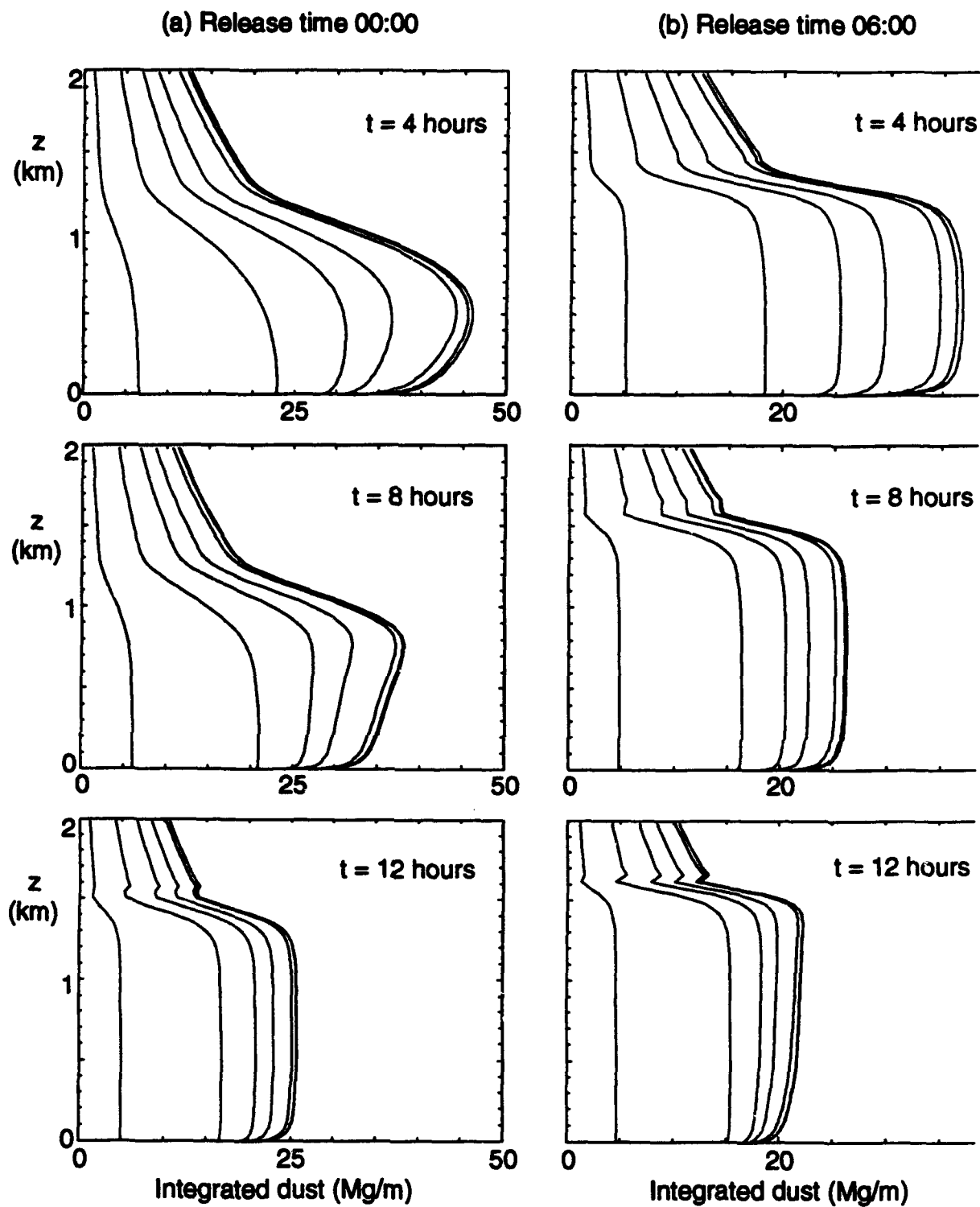


Figure 4-6. Integrated dust profiles at 4, 8, and 12 hours after release. Release is at (a) 00:00 (b) 06:00; (c) 12:00; (d) 18:00. Wind speed 10m/s, roughness length 1.0m.

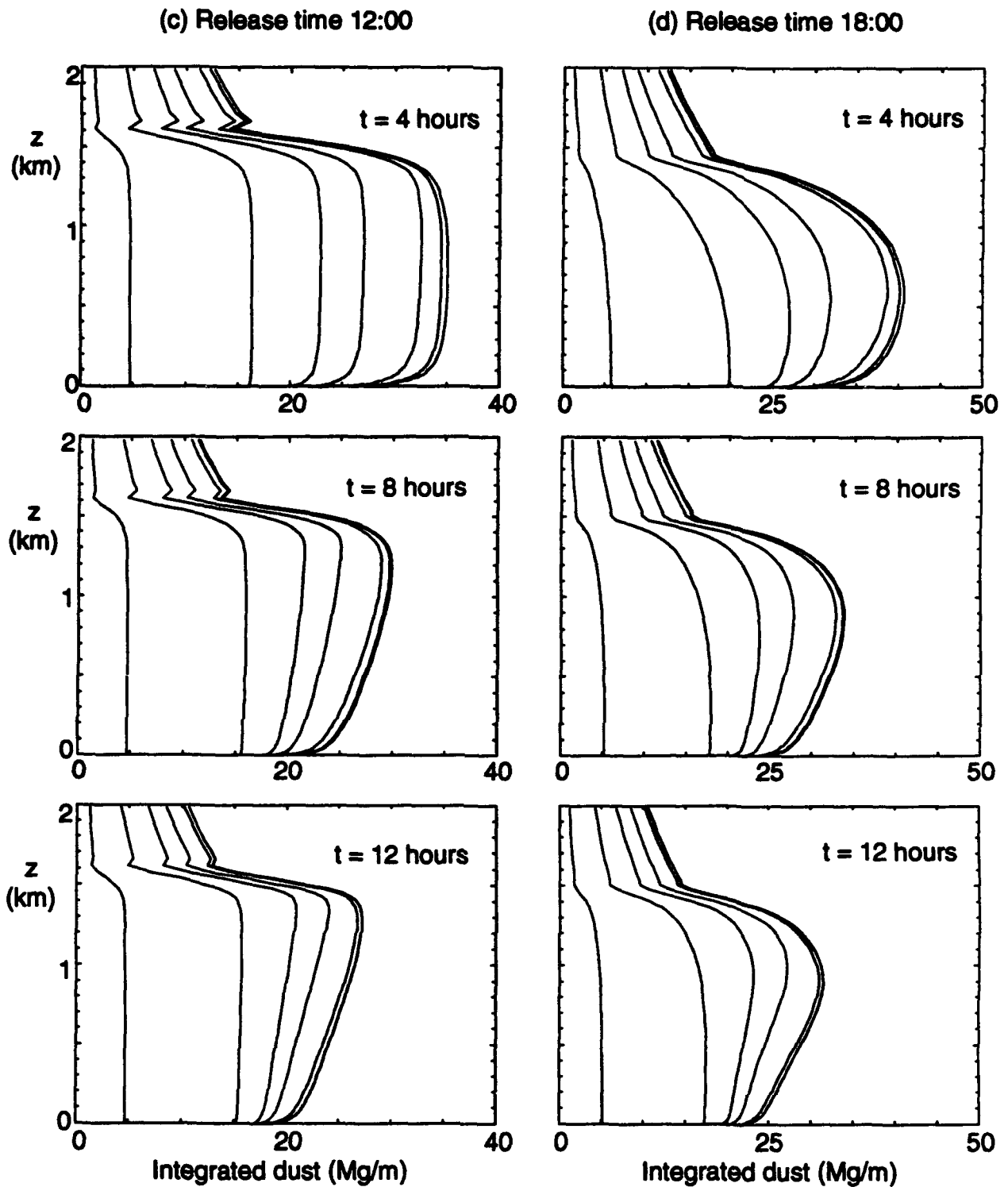


Figure 4-6. Integrated dust profiles at 4, 8, and 12 hours after release. Release is at (a) 00:00; (b) 06:00; (c) 12:00; (d) 18:00. Wind speed 10m/s, roughness length 1.0m (Continued).

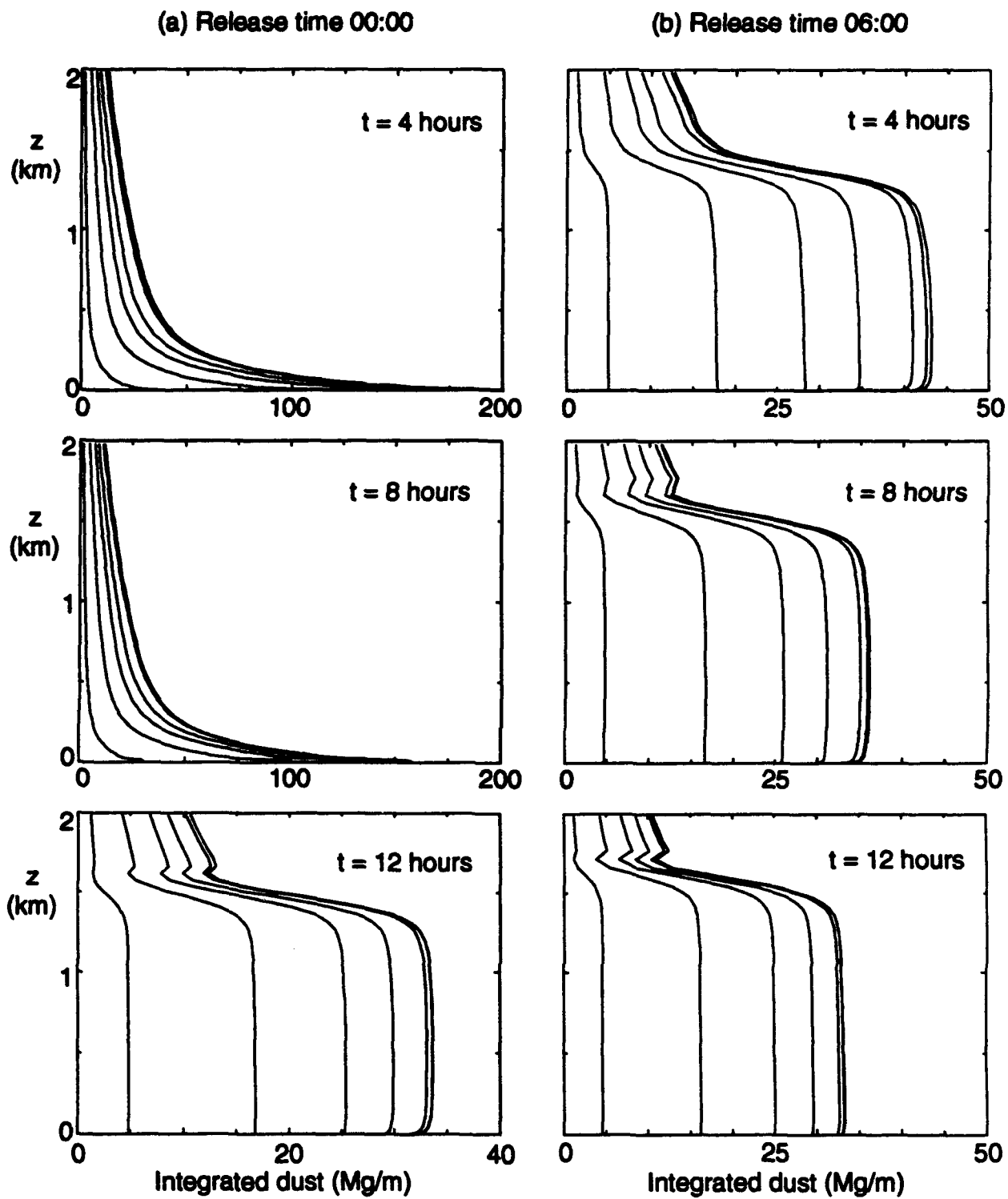


Figure 4-7. Integrated dust profiles at 4, 8, and 12 hours after release. Release is at (a) 00:00; (b) 06:00; (c) 12:00; (d) 18:00. Wind speed 2m/s, roughness length 1.0m.

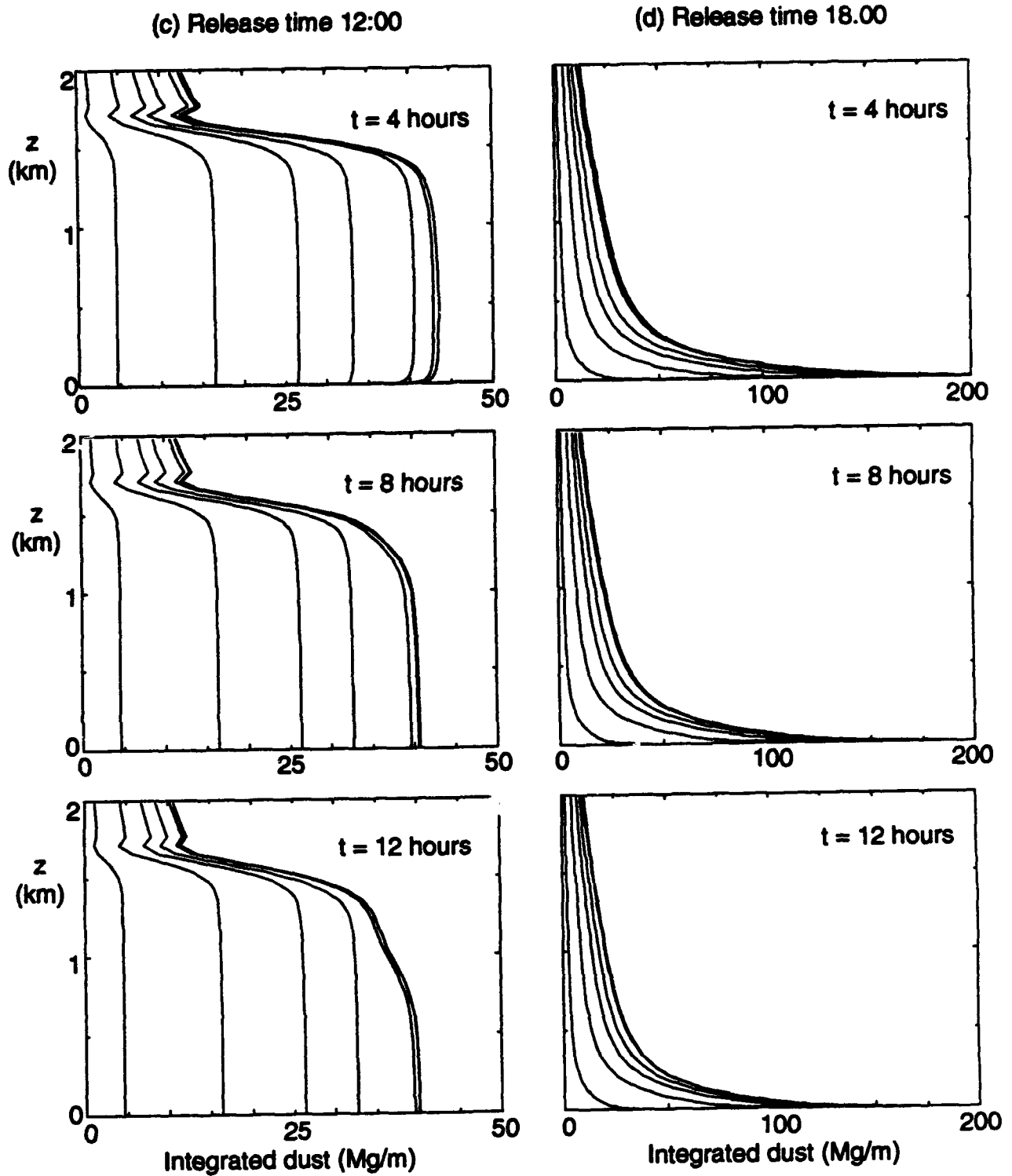


Figure 4-7. Integrated dust profiles at 4, 8, and 12 hours after release. Release is at (a) 00:00; (b) 06:00; (c) 12:00; (d) 18:00. Wind speed 2m/s, roughness length 1.0m (Continued).

Dust profiles 12 hours after an 06:00 release for various meteorological conditions

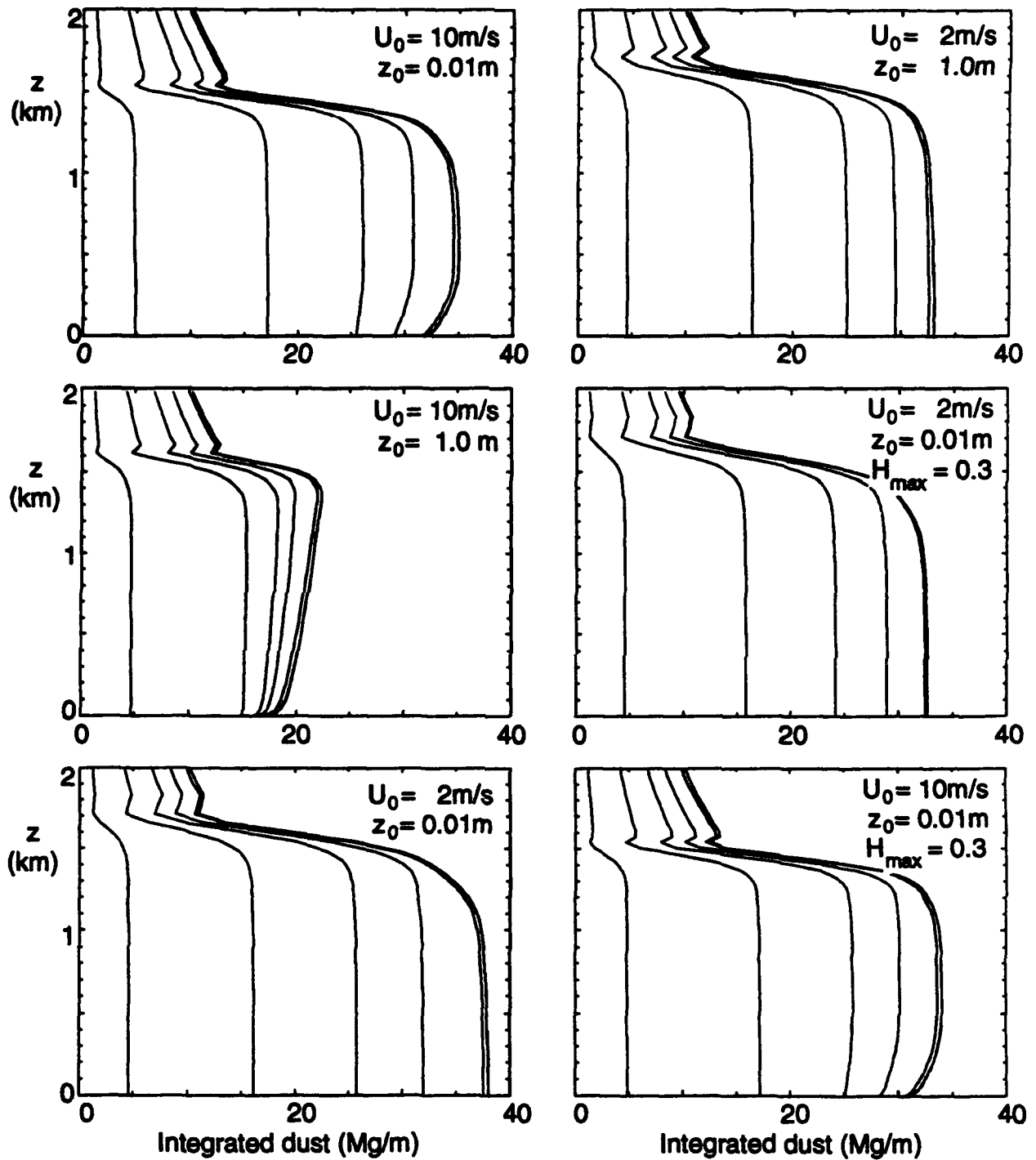


Figure 4-8. Integrated dust profiles at 12 hours after 06:00 release. Surface heat flux maximum is 0.075Kw/s unless noted.

The contribution from the pedestal in the late time dust profiles is indicated in Figure 4-9, where the initial dust field was truncated at $z=500\text{m}$ but all other parameters were the same as those in Figure 4-5. The limited vertical extent is evident in Figure 4-9, with no dust present above the mixed layer. The levels are also reduced at 12 hours, with mixed layer levels of about 20 Mg/m in the mixed cases and about 60 Mg/m in the 18:00 release case, i.e. roughly 2/3 of the full vertical distribution results. We also note that the largest size groups, with MMD 60 μm and 100 μm , are completely removed from the pedestal by 12 hours, and that the 100 μm group has settled out before 4 hours. The role of the turbulence in lofting the larger particles can be seen in the presence of the larger particles in the upper region of the mixed layer 4 hours after the 12:00 release, which immediately experiences turbulent mixing, but not for any of the other release times.

The particle size is very important in determining the fate of the dust over periods of 12 hours or more. Figure 4-10 shows the same cases as Figure 4-8, but under the assumption that all the particles are 10 μm size, instead of the spectral distribution. For high wind speed cases, the concentrations at 12 hours are lower, indicating increased deposition and gravitational settling compared with the earlier figure. The high roughness and high wind speed results are interesting, since they demonstrate that turbulent deposition at the surface is the important effect in reducing the low level dust concentrations. Low wind speed cases show slightly higher concentrations than Figure 4-8. This could be anticipated from Figure 4-1, which suggests that the deposition rate for these particles is important in the high wind speed, high roughness cases. The deposition velocity is generally small for 1 μm particles, but 10 μm particles can be absorbed quite rapidly under the appropriate conditions of high turbulence and roughness. The reduction in concentration near the surface is also evident in the high wind speed cases, indicating the importance of the surface deposition. In general, these results show much more sensitivity to the meteorology than those in Figure 4-8.

A more realistic particle size distribution, the proposed incipient distribution for the sweep-up material (Hassig, personal communication), emphasizes the mass in the larger particles. Results for various meteorological conditions are given in Figure 4-11. There is clearly more material in the 20 μm and 60 μm size groups, and this material displays the expected sensitivity to meteorology indicated by Figure 4-10. In general, the increased proportion of mass in the larger size groups leads to lower concentrations at

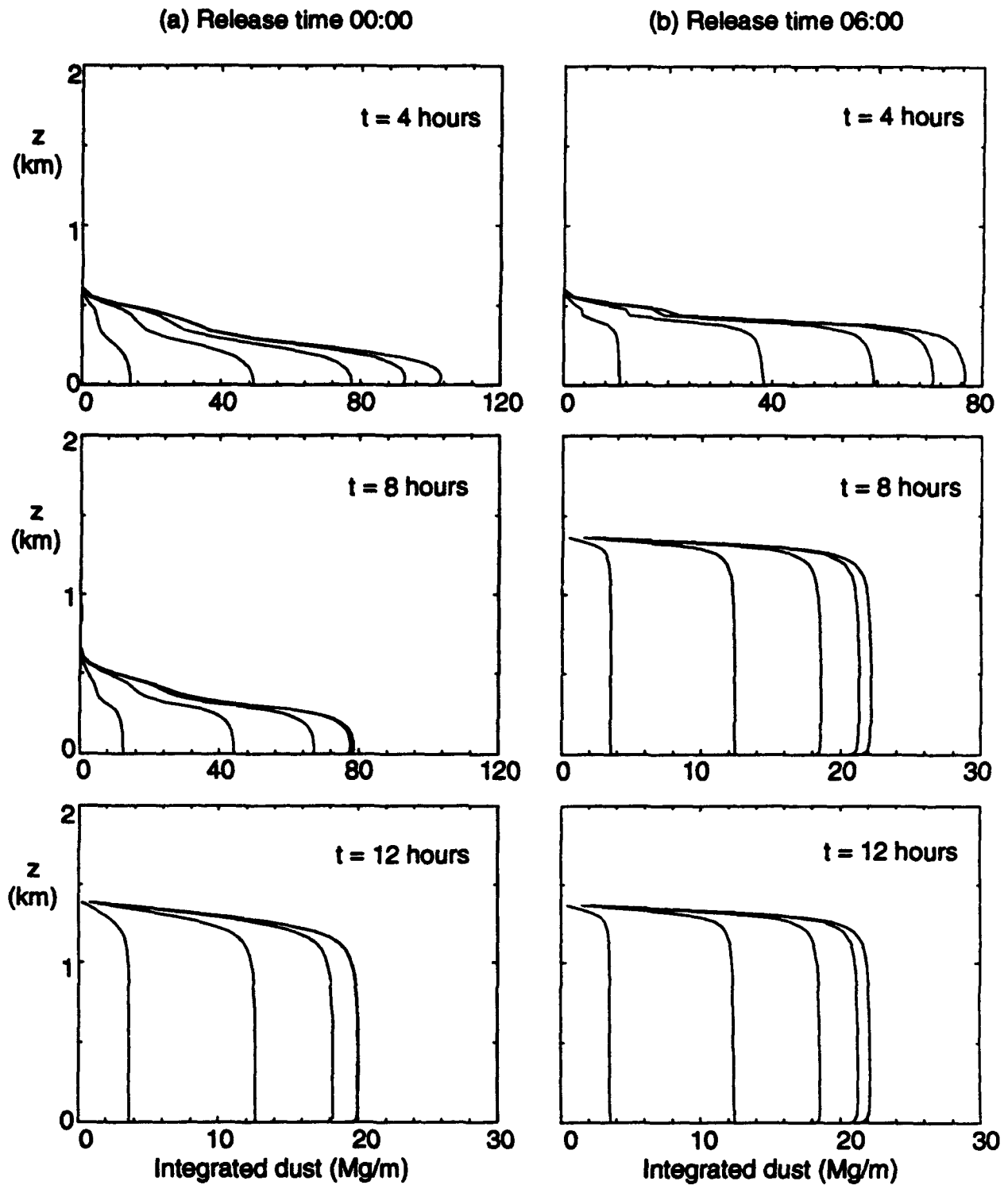


Figure 4-9. Integrated dust profiles at 4, 8, and 12 hours after release. Release is at (a) 00:00; (b) 06:00; (c) 12:00; (d) 18:00. Wind speed 10m/s, roughness length 0.01m, pedestal dust only.

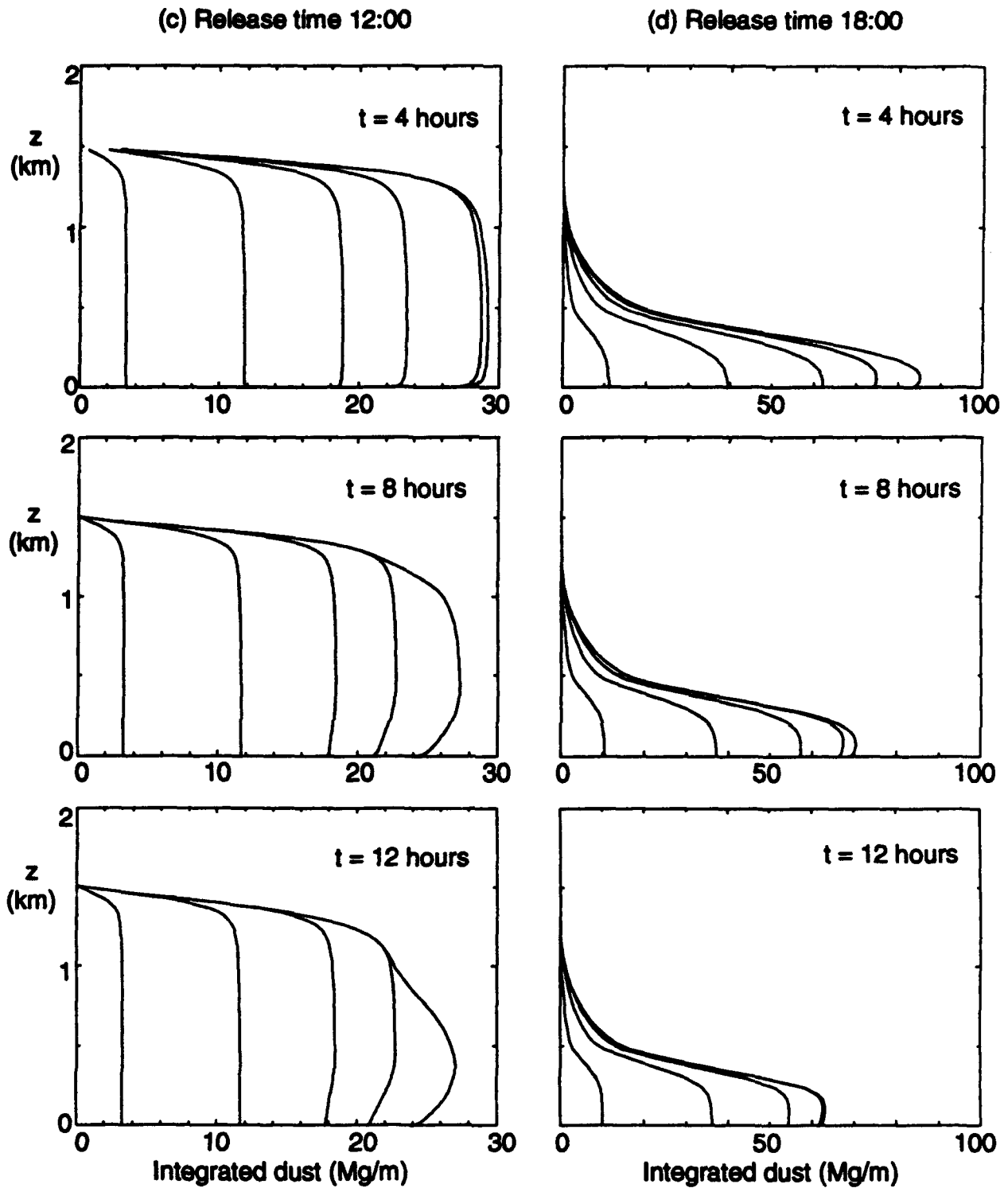


Figure 4-9. Integrated dust profiles at 4, 8, and 12 hours after release. Release is at (a) 00:00; (b) 06:00; (c) 12:00; (d) 18:00. Wind speed 10m/s, roughness length 0.01m, pedestal dust only (Continued).

Dust profiles 12 hours after an 06:00 release for various meteorological conditions

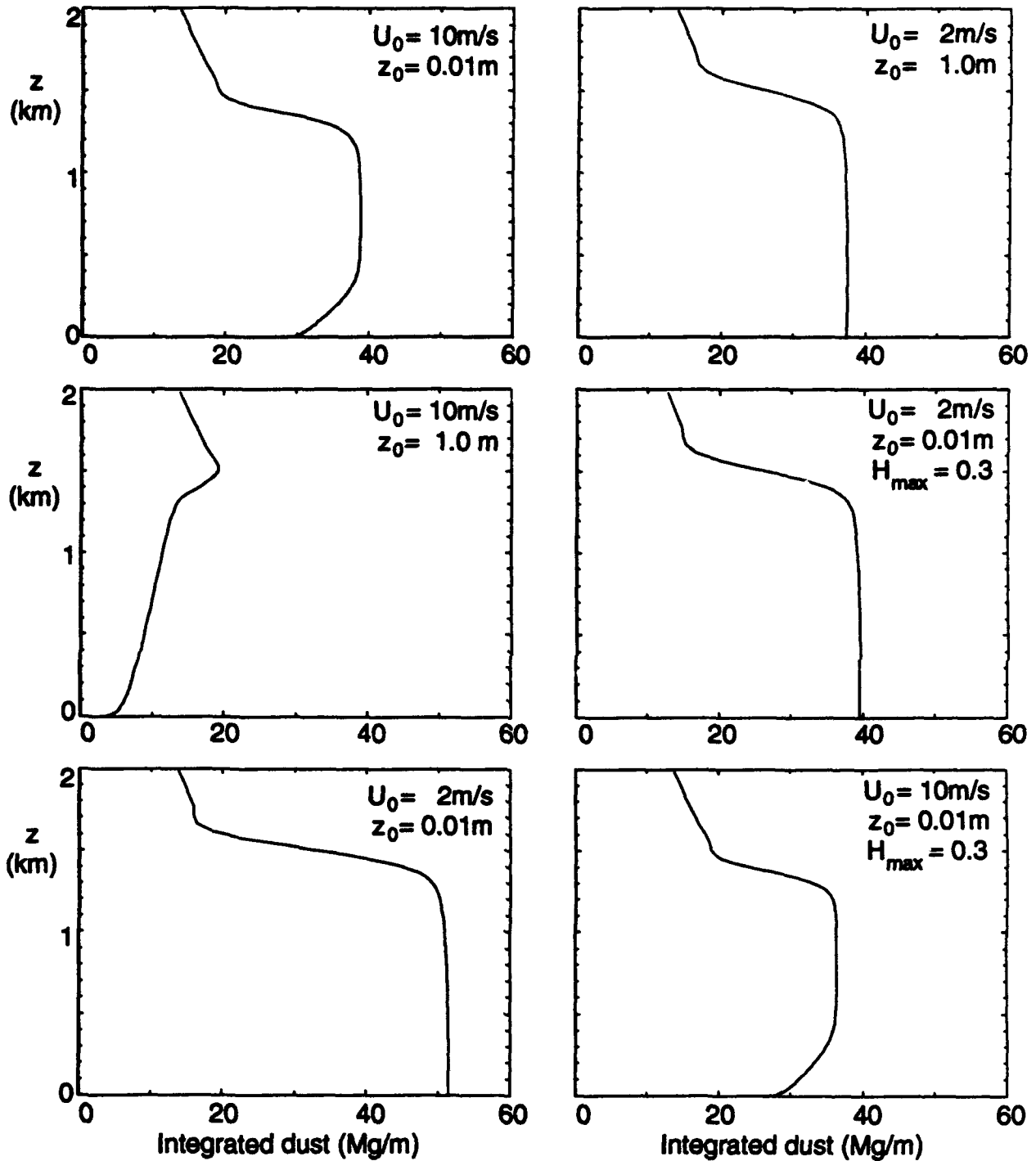


Figure 4-10. Integrated dust profiles at 12 hours after 06:00 release assuming all dust is 10 microns. Surface heat flux maximum is 0.075Kw/m² unless noted.

Dust profiles 12 hours after an 06:00 release for various meteorological conditions

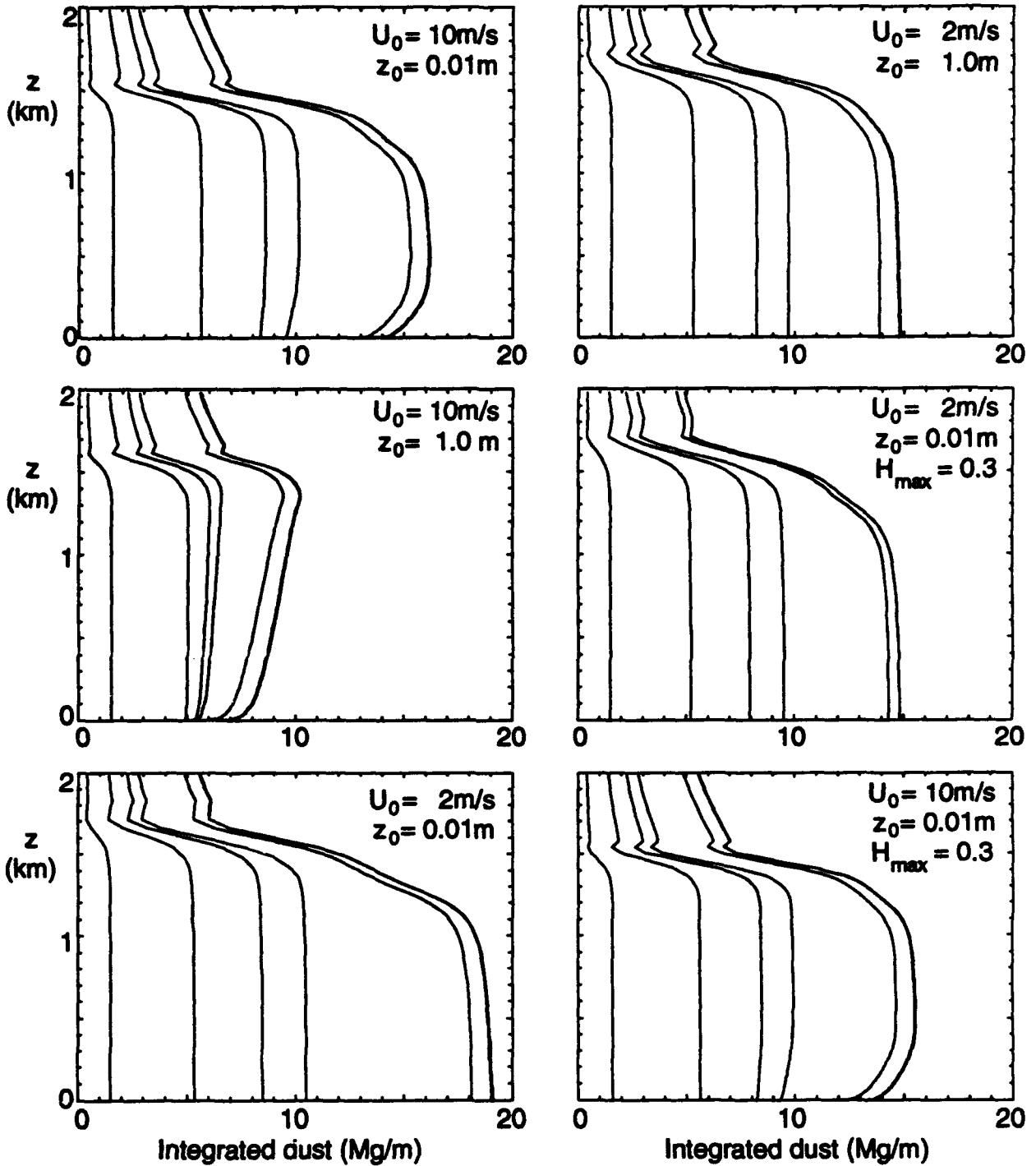


Figure 4-11. Integrated dust profiles at 12 hours after 06:00 release assuming proposed incipient particle size distribution. Surface heat flux maximum is 0.075Km/s unless noted.

later times, since this mass is deposited more effectively than the smallest size groups. The mixed layer total concentrations are roughly half the values of Figure 4-8.

4.4 SUMMARY OF BOUNDARY LAYER RESULTS.

Numerical solutions of the turbulent transport and deposition model equations have indicated that a significant fraction of the dust pedestal from a large nuclear burst can remain lofted in the surface mixing layer for periods of up to 24 hours. This behavior is dependent on the particle size distribution in the pedestal, and can be summarized as follows.

For particles below $5\mu\text{m}$, the turbulent deposition and also gravitational settling are negligible over the time period of one day, so that the initial material is simply redistributed vertically by the turbulence induced by daytime heating. Provided a mixed layer of depth around 1km is formed during the day, the vertical distribution of material is insensitive to meteorological parameters, although the lateral distribution will depend on the wind. This result will apply if the bulk of the pedestal dust is in this size range, as might be predicted by a typical size spectrum assumption, if a lower cutoff of $1\mu\text{m}$ is assumed.

For particles above $30\mu\text{m}$, the gravitational settling is sufficiently rapid that the pedestal is removed after a few hours, even in the presence of relatively strong vertical mixing. This result is also insensitive to meteorological variations.

The size range between $5\mu\text{m}$ and $30\mu\text{m}$ displays more complex behavior, since the turbulent deposition velocities in this range can vary from negligible to significant over the range of meteorological parameters, while the gravitational settling is generally small. Thus, under light wind, small roughness conditions most of this material will remain lofted through the mixed layer for 24 hours, while the surface deposition under high wind speed, high roughness conditions will deplete the material by up to 90% over such a period.

SECTION 5

STATISTICAL FALL-OUT ANALYSIS

The dust lofted by a nuclear burst persists in the atmosphere for many hours. Different size particles fall at different rates, so the distribution changes with time as it is moved by the local winds. Dust can cause damage to aircraft systems, so predictions of the late-time distribution are important for planning purposes. However, while predictions are certainly feasible for a given wind field using current late-time dispersion models, the wind field is generally not known for planning scenarios. Statistical studies of the climatological variability in the wind field at specific sites shows the r.m.s. fluctuation in wind component speed to be larger than the mean value, indicating a large uncertainty, and a statistical description of the effects of this variability on aircraft vulnerability is desirable.

Ross (1991) has initiated an effort to extend the SAFER methodology (Ross and Mazzola, 1993) to the aircraft problem. This approach, successfully applied to the RV-fratricide problem, gives a very efficient analytical description of the probability of encountering critical loading, and is simple enough to apply at a systems planning level. The difficulties involved in the late-time aircraft problem, however, prevented the calculation of more than the ensemble average dust mass loading along a flightpath. The late-time problem is more complicated than the RV-fratricide problem, since it critically involves dust falling through different levels of the atmosphere, and the winds vary with altitude in general. The RV-fratricide problem was restricted to relatively short times, where only horizontal transport need be considered. Unfortunately, the ensemble mean mass loading is not the most useful quantity for a planner, who usually wants to know the probability of failure, and the objective of the present study is the extension of Ross' approach to provide this probabilistic information.

The dust density distribution is specified as a function of space (x), time (t), and particle size (a), i.e., $\chi(x, t, a)$. The aircraft mass loading involves a line integral of the dust along a flightpath at a certain altitude. This could be in any direction at any time after the burst, but we specify these parameters as fixed for definiteness in the analysis. We consider the mass loading along a N-S flightpath at $z = 100\text{m}$ and $t = 8$ hours after burst,

$$\begin{aligned}
m(x) &= \int_{-\infty}^{\infty} dy \int_{-\infty}^{\infty} da \chi(x, y, 100\text{m}, 8\text{hrs}, a) \\
&= \int_{-\infty}^{\infty} \mu(x, a) da
\end{aligned} \tag{5.1}$$

where $\mu(x, a)$ is the mass loading density from particles size a . We assume that $\mu(x, a)$ is obtained from the initial loading of particle size a , at an initial altitude of $z_0(a)$ such that the particles fall to $z = 100\text{m}$ after 8 hours. This is the methodology adopted by Ross (1991) and provides a simple conceptual framework for analyzing the effects of wind variations.

We further assume that $\mu(x, a)$ has a Gaussian spatial distribution with centroid $X(a)$, and spread $\sigma(a)$, i.e.,

$$\mu(x, a) = \frac{M_0(a)}{\sqrt{2\pi} \sigma(a)} \exp\left[-\frac{(x - X(a))^2}{2\sigma^2(a)}\right] \tag{5.2}$$

where

$$M_0(a) = \iint \chi(x, y, z_0(a), 0, a) dx dy \tag{5.3}$$

The centroid location, X , is determined by the wind profile, $u(z)$, over the levels traversed by the particles as they fall to $z = 100\text{m}$. Assuming a constant fall velocity,

$$X = U(z_0) t \tag{5.4}$$

where

$$U(z) = \frac{1}{(z - 100\text{m})_{100\text{m}}} \int_{100\text{m}}^z u(z') dz' \tag{5.5a}$$

i.e., the centroid displacement is the layer-averaged velocity multiplied by the translation time. In reality, the particle fall speed is height-dependent due to the variation in air density, so the layer-average velocity should strictly include a weighting factor proportional to the inverse fall speed, as described by Ross (1991). Thus

$$U(z) = \frac{1}{8 \text{ hrs}} \int_{100\text{m}}^z \frac{u(z')}{w_d(z')} dz' \tag{5.5b}$$

where w_d is the local fall speed. Definition (5.5b) is size-dependent, in general, since fall speed depends on particle size, so the wind statistics will be defined using Equation

(5.5a) in the subsequent analysis for simplicity. We note that the proper definition (5.5b) could be used to define the appropriate $U(z)$, and this was actually used in the Monte-Carlo realizations computed below.

The spread, σ , is determined by atmospheric diffusion. We assume a simple model for diffusion, although a more sophisticated formulation could easily be employed since the subsequent analysis only uses the value of σ and is independent of the precise diffusion mechanism. For definiteness, we use the Heffter parameterization for the diffusive spread, which is a constant rate growth of the horizontal spread, i.e.,

$$\sigma = 0.5t \quad (\sigma \text{ in meters, } t \text{ in seconds}) \quad (5.6)$$

Equations (5.1)-(5.6) permit the calculation of $m(x)$ if we are given:

- (i) a wind profile, and
- (ii) an initial dust density distribution.

The problem we seek to solve is to determine the statistics of $m(x)$ when the winds are uncertain, i.e., we only have statistical information on the wind field. However, Equations (5.1)-(5.6) can be used directly to perform Monte-Carlo simulations of the loading problem using a large collection of observed wind profiles. This technique is not computationally efficient, but does generate a 'true' distribution with which to compare simplified models.

The main component of uncertainty in m is due to uncertainty in X , i.e., where does the dust go? We therefore assume σ is fixed in the following analysis, and only the centroid is random. The conceptual model is thus a horizontal Gaussian spatial distribution with fixed spread for each particle size located at a random centroid position.

The mass centroid, X , is a random variable, related to the random wind field through Equation (5.4). The mean and variance of X are easily seen to be

$$\bar{X} = \bar{U}(z_0) t \quad (5.7)$$

$$\Sigma^2 = \overline{X'^2} = \overline{(X - \bar{X})^2} = \overline{U'^2}(z_0) t^2 \quad (5.8)$$

We represent the probability distribution function (pdf) of X by a Gaussian, so that

$$p(X) = \frac{1}{\sqrt{2\pi}\Sigma} \exp \left[-\frac{(X - \bar{X})^2}{2\Sigma^2} \right] \quad (5.9)$$

Then, using Equation (5.2), we calculate the mean size-dependent loading,

$$\begin{aligned}\bar{\mu}(x, a) &= \int \mu(x, a; X) p(X) dX \\ &= \frac{M_0}{\sqrt{2\pi S}} \exp \left[-\frac{(x - \bar{X})^2}{2S^2} \right]\end{aligned}\quad (5.10)$$

where $S^2 = \sigma^2 + \Sigma^2$ (5.11)

and hence, from Equation (5.1), the mean mass loading is

$$\bar{m}(x) = \int \bar{\mu}(x, a) da \quad (5.12)$$

The mean wind statistics are presented by Ross (1991) and are repeated here in Figure 5-1, which shows the mean and standard deviation as a function of altitude from 3652 Moscow wind profiles. These profiles were used to compute 3652 mass loading profiles from an initial TASS LM02 cloud using Equations (5.1)-(5.6). The ensemble mean loading from these Monte-Carlo results is shown in Figure 5-2, along with the ensemble prediction from equations (10) and (12). The mean loading compares well with the Monte-Carlo calculation, indicating the accuracy of the Gaussian approximation for the pdf of the wind fluctuations.

The above analysis gives qualitatively similar results to Ross's analysis, in spite of his assumption of disks rather than Gaussian distributions. The main difference is due to our assumption that the wind is constant below the lowest observation level, whereas Ross appears to assume that the wind goes linearly to zero at the ground. We believe that the mixing effect of the planetary boundary layer will produce a more uniform vertical profile over this region. We also include the late-time diffusion using the Heffter model, so our intercepted dust loadings are lower than Ross'. The mean mass loading is not sensitive to the detailed shape assumption, since $\sigma \ll \Sigma$, and therefore the wind fluctuations dominate the result.

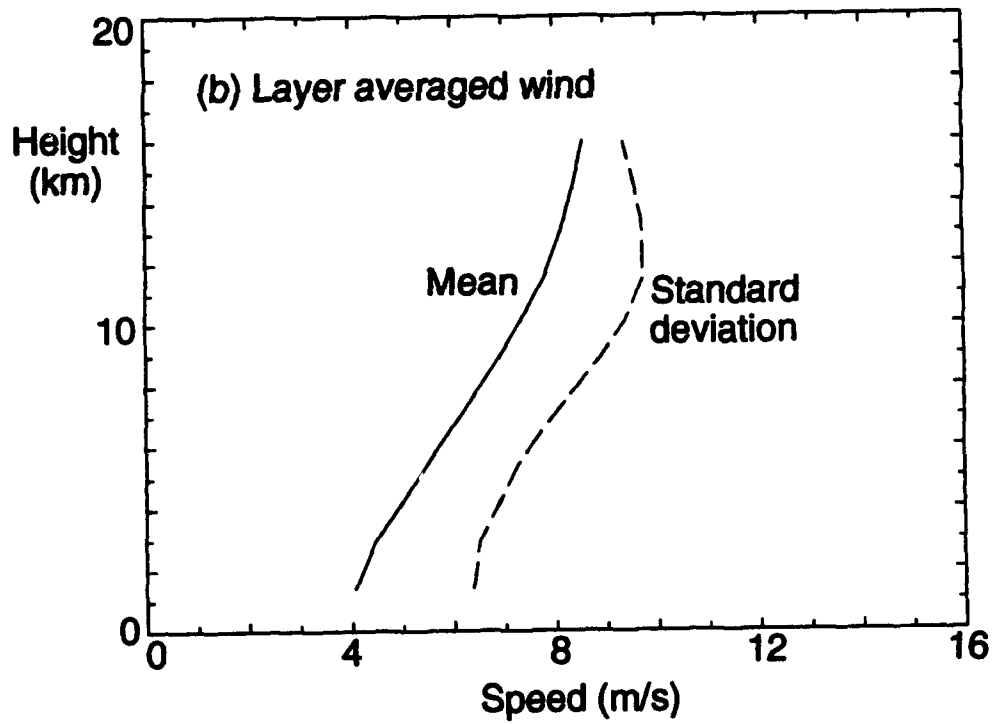
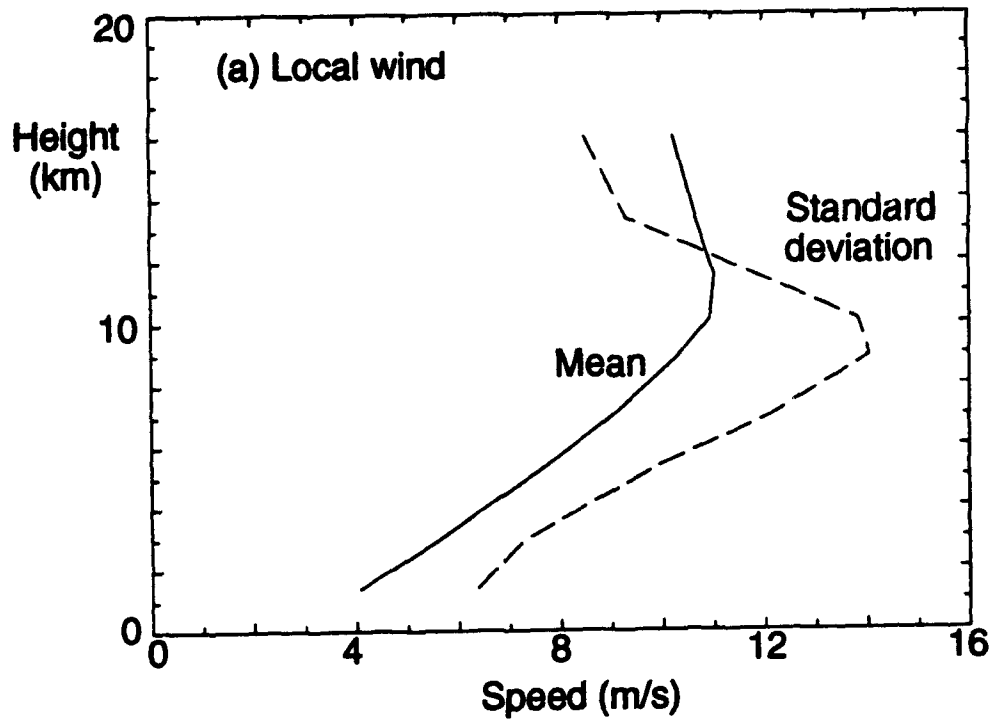


Figure 5-1. Wind statistics for the East-West component from 3652 Moscow wind profiles. (a) local wind at altitude; (b) average wind between altitude and ground.

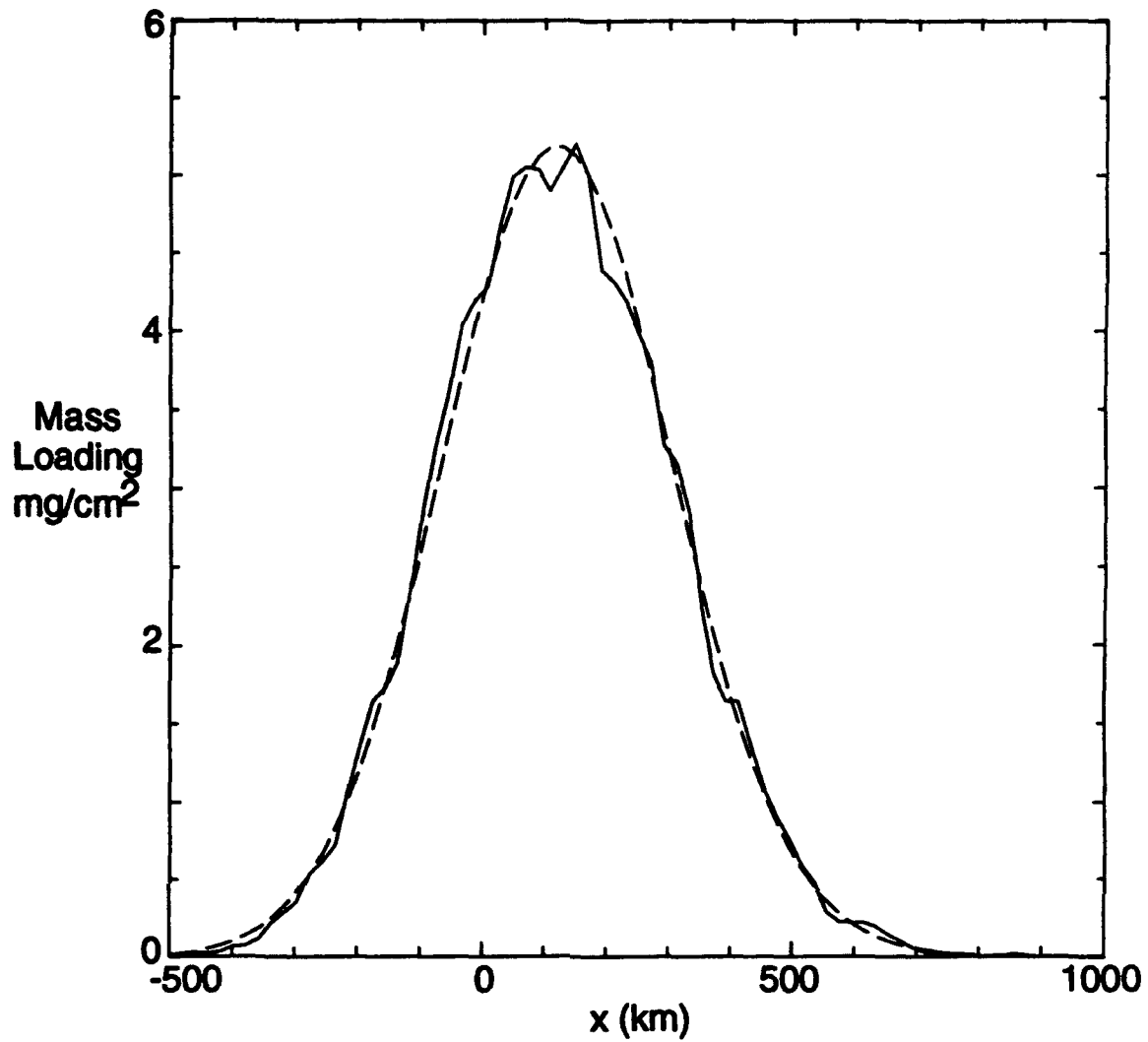


Figure 5-2. Mean mass loading after 8 hours along a North-South flightpath at 100m altitude for an ensemble of 3652 Moscow winds. The explicit Monte-Carlo result (solid) and the ensemble statistical calculation (dashed) are shown as a function of East-West location relative to the burst.

So far, we have only produced a slightly different version of the mean mass loading. Our objective, however, is to obtain information about the pdf of $m(x)$, not just the average value, so we need to extend the analysis. Calculation of the detailed pdf of m is extremely complicated, so a simpler approach is needed. The mean value is the first moment of the pdf, and gives no information about the range of possible values in the distribution. By calculating higher moments, more detail about the pdf is revealed and quantitative estimates can be derived. We seek to compute the second moment, $\overline{m'^2}$, and use an analytic shape assumption about the pdf to get estimates of likelihood of exceeding a specified threshold. The anticipated shape is the clipped-normal function, which provides an intermittent pdf and is completely determined by the mean and variance of the distribution.

Some support for the use of a clipped normal distribution is provided by the Monte-Carlo results themselves. The explicit calculation of 3652 realizations allows us to construct the pdf at any location, and the cumulative distribution function (cdf) of the mass loading at two x -locations is shown in Figure 5-3. The cdf represents the fraction of the loadings below the level plotted on the horizontal axis. The distortion of the vertical scale is such that a clipped normal distribution is a straight line, and the intercept on the axis gives the probability of zero loading, i.e. the intermittency. The Monte-Carlo results show a reasonably straight-line section, apart from a tail-off at small loadings, i.e., there is a significant probability of a small but non-zero loading. The pdf at higher loadings can be well represented by the clipped normal, but the details at low mass loading would require a different shape assumption for the pdf. For the present purposes, we assume that the larger values are of interest, and use the clipped normal distribution.

The statistics of $\mu(x,a)$ are identical to those of Gifford's (1959) meandering plume model. Thus, following Gifford's analysis, the variance is given by

$$\begin{aligned} \overline{\mu'^2} &= \int (\mu - \bar{\mu})^2 p(X) dX \\ &= \frac{M_0^2}{2\pi\sigma(\sigma^2 + 2\Sigma^2)^{1/2}} \exp\left[-\frac{(x - \bar{X})^2}{\sigma^2 + 2\Sigma^2}\right] - \bar{\mu}^2 \end{aligned} \quad (5.13)$$

However, the mass loading involves an integral over particle size, so

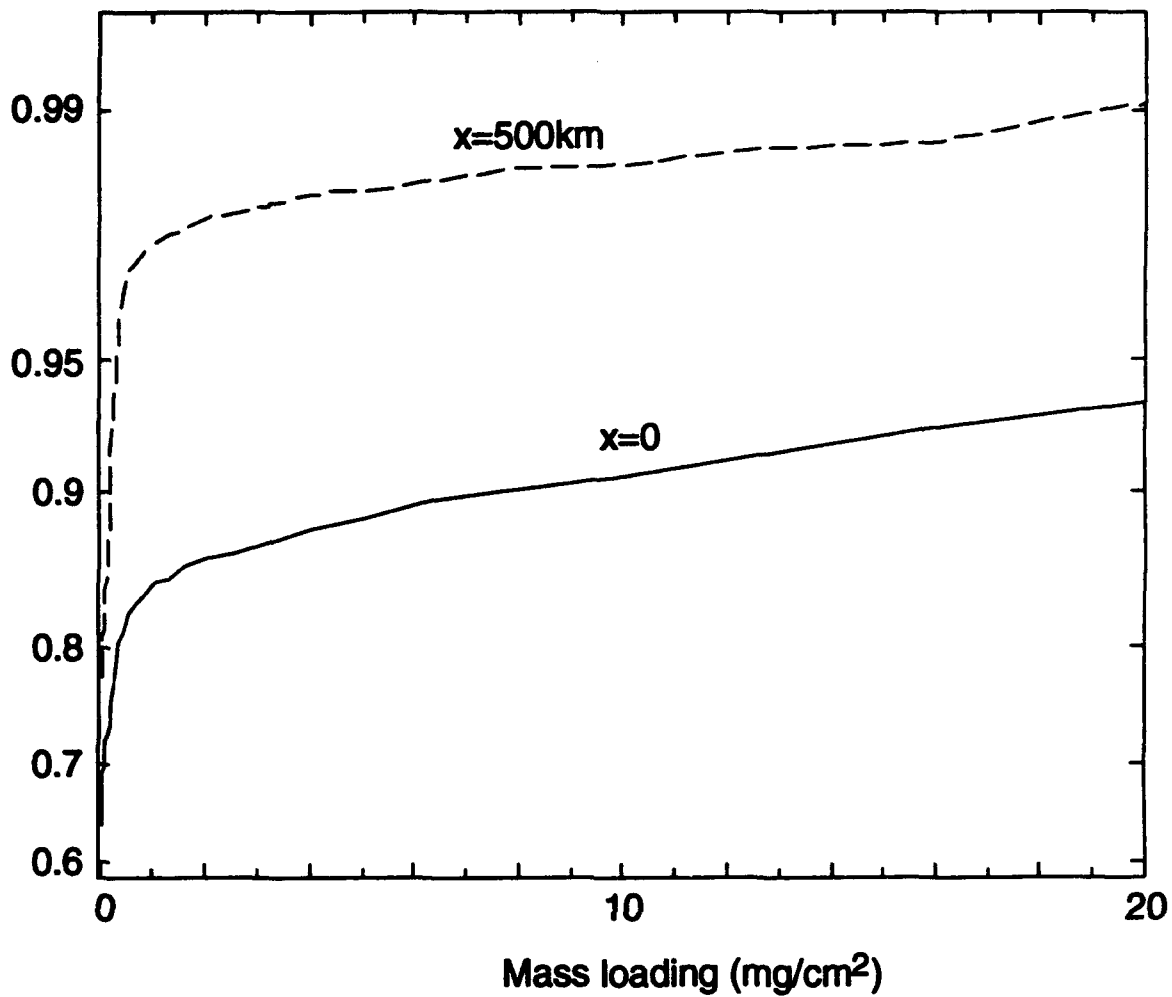


Figure 5-3. Cumulative distribution of the mass loading at 8 hours from the Monte-Carlo results with 3652 winds (i.e. probability that loading is less than given value) at two locations.

$$\overline{m'^2} = \int_{a_{\min}}^{a_{\max}} da_1 \int_{a_{\min}}^{a_{\max}} da_2 \overline{\mu'(a_1)\mu'(a_2)} \quad (5.14)$$

i.e., we need the correlation between the loadings from different particle sizes.

A similar problem arises in the time-averaging of Gifford's meandering plume, where temporal correlations are required, and a solution based on the wind fluctuation correlation was given by Sykes (1984). We can use the same approach for our particle size integration, but we need to extend the analysis to account for the inhomogeneous statistics of the wind field. As we shall see below, the wind field is very strongly correlated at different heights, but the increasing mean and variance with altitude has a large effect on the loading correlations. The two-point correlation is defined as

$$\overline{\mu(a_1)\mu(a_2)} = \iint \mu(a_1, X_1)\mu(a_2, X_2)p(X_1, X_2)dX_1dX_2 \quad (5.15)$$

and this can be evaluated if the joint probability of the centroid locations, $p(X_1, X_2)$, for the two particle sizes can be specified.

We assume a joint-normal distribution for the centroids, i.e.,

$$p(X_1, X_2) = \frac{1}{2\pi \Sigma_1 \Sigma_2 (1-r^2)^{1/2}} \times \exp \left[\frac{-X_1'^2 \Sigma_2^2 - 2rX_1'X_2'\Sigma_1\Sigma_2 - X_2'^2 \Sigma_1^2}{2\Sigma_1^2 \Sigma_2^2 (1-r^2)} \right] \quad (5.16)$$

where

$$\Sigma_1^2 = \overline{X_1'^2}, \quad \Sigma_2^2 = \overline{X_2'^2}, \quad \text{and} \quad r = \frac{\overline{X_1'X_2'}}{\Sigma_1 \Sigma_2}$$

Since $X = U(z_0)t$, the correlation r is related to the wind correlation. We model

$$r(a_1, a_2) = \exp \left[-\frac{|a_1 - a_2|}{\ell(a_1)} \right] \quad (5.17)$$

where

$$\ell = \ell_u / \frac{dz_0}{da} \quad (5.18)$$

and ℓ_w^* is determined from the correlation of the winds at different altitudes. The correlation function,

$$\frac{\overline{U'(z_1)U'(z_2)}}{\left(\overline{U'^2(z_1)} \overline{U'^2(z_2)}\right)^{1/2}} \quad (5.19)$$

is shown in Figure 5-4 for $z_1=1450\text{m}$. The very strong correlation over a depth of 15km is obvious. The actual velocity correlation is also given, illustrating the effect of the vertical averaging in (5-5a). The fact that a falling particle experiences an average velocity over the depth of its fall greatly increases the correlation between the winds experienced by particles from different initial heights. Fitting an exponential function to the correlation curve in Figure 5-4 gives a vertical length scale of about 50km for the velocity field. Thus the transport at altitude is extremely well correlated with the near-surface transport, but it is not identical since the winds are higher aloft. This difference causes different particle sizes to fall out at different locations and destroys the particle correlations.

Substituting (5-16) into (5-15) and using (5-2), after some algebraic manipulation, we obtain

$$\overline{\mu(a_1)\mu(a_2)} = Q_{12} \exp\left[-\frac{(x - \bar{X}_{12})^2}{2\sigma_{12}^2}\right] \quad (5.20)$$

where

$$Q_{12} = \frac{M_{01} M_{02}}{\left[S_1^2 S_2^2 - r^2 \sigma_1^2 \sigma_2^2\right]^{1/2}} \exp\left[-\frac{(\bar{X}_1 - \bar{X}_2)^2}{2(S_1^2 + S_2^2 - 2r\sigma_1\sigma_2)}\right] \quad (5.21)$$

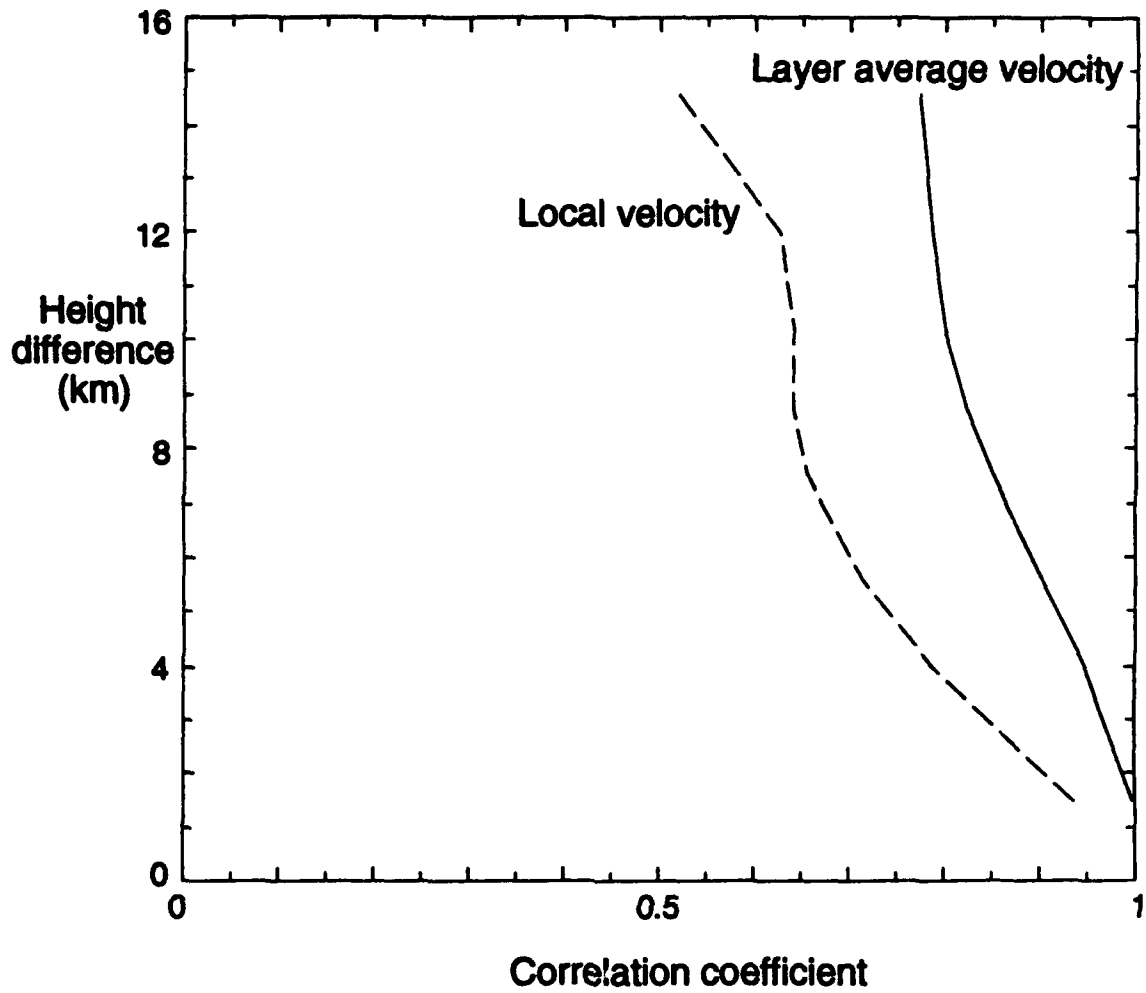


Figure 5-4. Correlation between East-West velocities at two altitudes from 3652 Moscow wind profiles. Lower level is fixed at 1450m. Correlations between the local velocity and the average over the layer between the two levels are shown.

$$\bar{X}_{12} = \frac{\bar{X}_1(S_2^2 - r\Sigma_2\sigma_2) + \bar{X}_2(S_1^2 - r\sigma_1\Sigma_1)}{S_1^2 + S_2^2 - 2r\sigma_1\sigma_2} \quad (5.22)$$

$$\sigma_{12}^2 = \frac{S_1^2 S_2^2 - r^2 \sigma_1^2 \sigma_2^2}{S_1^2 + S_2^2 - 2r\sigma_1\sigma_2} \quad (5.23)$$

Equation (5.14) involves a double integral over the size spectrum, but much of this space is uncorrelated. For speed and simplicity of computation, we represent the correlation function by an exponential with scale λ , and integrate analytically over one of the dimensions, to get

$$\overline{m'^2(x)} = \int_{a_{\min}}^{a_{\max}} \overline{\mu'^2(a, x)} g(a, x) da \quad (5.24)$$

where

$$g(a, x) = \lambda(a, x) (2 - e^{-(a-a_{\min})/\lambda} + e^{-(a_{\max}-a)/\lambda}) \quad (5.25)$$

The correlation scale, $\lambda(a, x)$, is numerically determined from the point, a' , where $\frac{\mu'(a)\mu'(a')}{\mu'^2(a)}$ falls to a value of 0.5. This involves a numerical search at each point, but is still very efficient.

The profile of the mass loading standard deviation is shown in Figure 5-5, in comparison with the Monte-Carlo result. The analytic model shows reasonably good agreement with the explicit calculation, giving a standard deviation roughly twice the mean value near the peak of the curve at $x=0$. As we move away from the peak, the ratio gets larger indicating more intermittent statistics as illustrated in Figure 5-3.

Figures 5-6 and 5-7 show the predicted probability of exceeding $1\text{mg}/\text{cm}^2$ and $10\text{mg}/\text{cm}^2$ as a function of horizontal (E-W) location, using the predicted variance and the clipped normal assumption or the pdf. Again, the agreement with the Monte-Carlo calculation is very encouraging, demonstrating that the analysis can be used

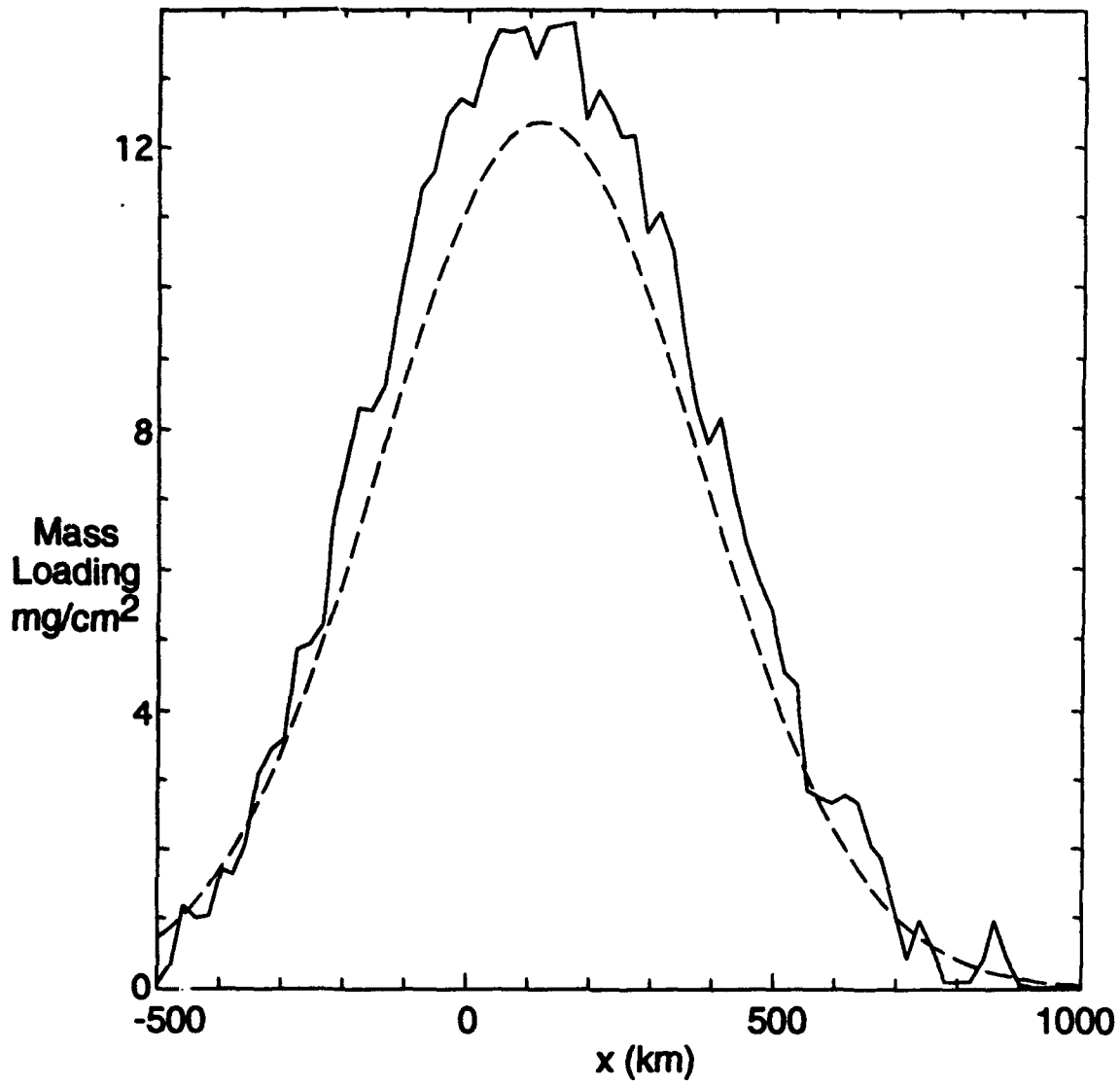


Figure 5-5. R.m.s. mass loading after 8 hours for a North-South flightpath at 100m from an ensemble of 3652 Moscow winds. The explicit Monte-Carlo result (solid) and the statistical ensemble calculation (dashed) are shown.

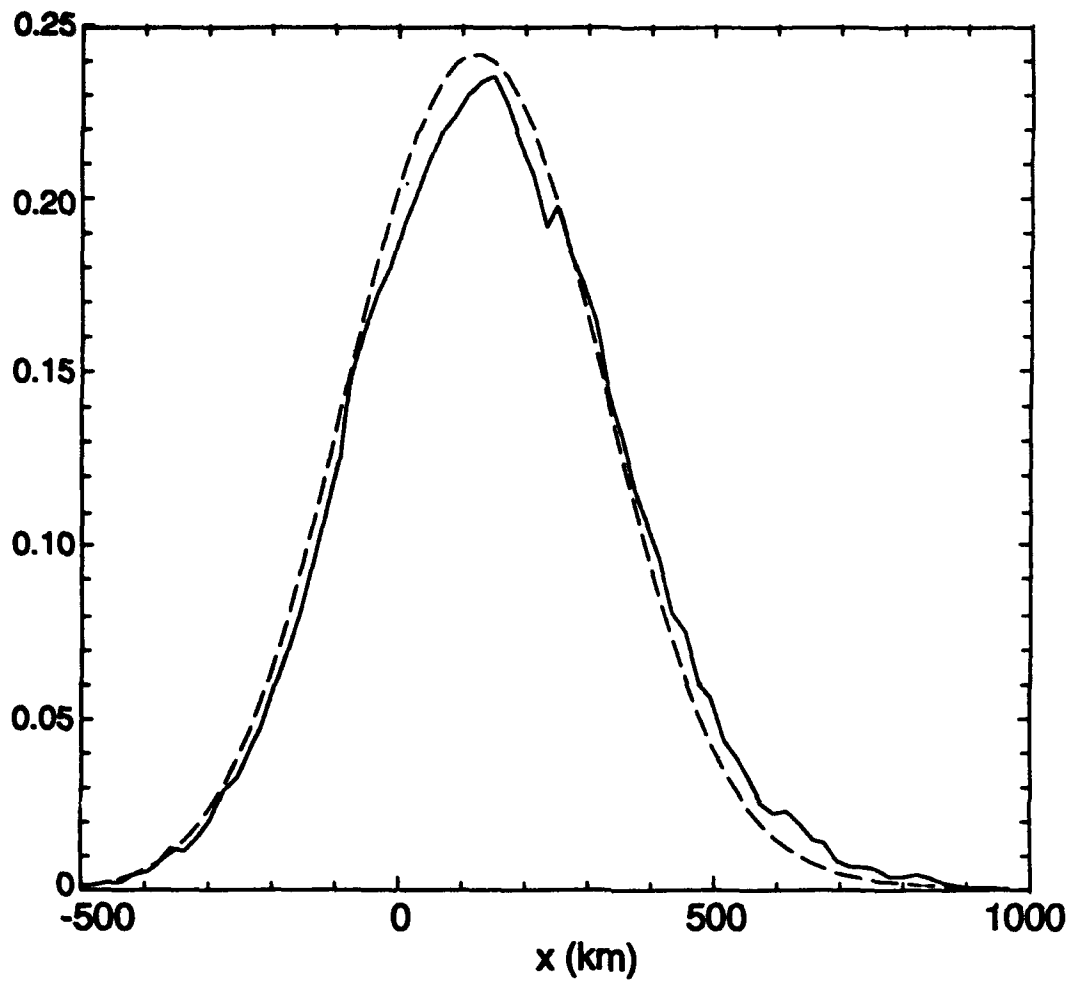


Figure 5-6. Probability of mass loading exceeding 1 mg/cm^2 for the ensemble of 3652 Moscow winds. Comparison between Monte-Carlo calculation (solid) and statistical estimate (dashed).

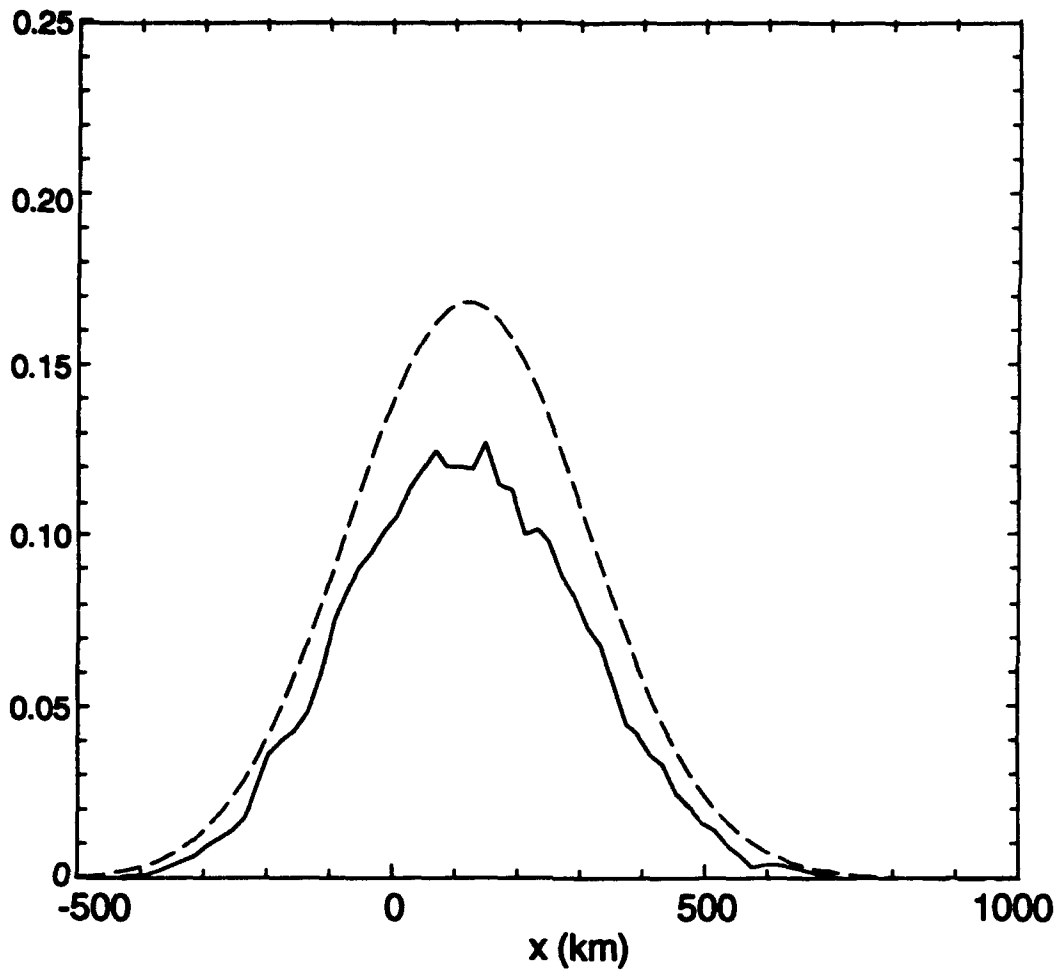


Figure 5-7. Probability of mass loading exceeding 10 mg/cm^2 for the ensemble of 3652 Moscow winds. Comparison between Monte-Carlo calculation (solid) and statistical estimate (dashed).

to give useful statistical predictions of the probability of intercepting various mass loadings in the presence of large wind uncertainties.

The details of the statistics can be easily modified to accommodate the height-dependent fall speed or alternative cloud diffusion rates. The analysis could also be performed for subsets of the climatological statistics, e.g. seasonal ensembles. The representation of multiple bursts and multiple aircraft routes would require further work, but the method presented here is a first step toward a realistic assessment of the uncertainties induced by the wind variability.

SECTION 6

SCIPUFF MODEL STUDIES

6.1 RADIOACTIVE FALLOUT FROM 20KT WEAPON.

A calculation of the late-time radioactive cloud and fallout from a small nuclear weapon was performed using initial conditions from the DICE/MAZ code. The standard cloud description was extended to track a level of radioactivity for each puff, specified as an active mass fraction, f_R . This fraction is conserved for an individual puff, assuming no radioactive decay on the time scales of interest, and the total active mass is conserved in a puff merging operation. In addition to the mass activity level, a fallout computation was included in SCIPUFF to track the deposition of material and the radioactivity on a surface grid. The total mass fallout from each puff was already routinely computed at each timestep, since this is the mass rate-of-change term, but the deposition was not stored. The code was extended to partition the mass deposition from each puff on a surface grid of points, using a Gaussian distribution in the horizontal plane and an appropriate mass-conserving normalization. Thus, all mass lost from the puffs is balanced by an increase in the surface deposition.

Initial conditions for the late-time SCIPUFF calculation were taken from the MAZ results for a 20kT surface burst at $t = 5$ minutes. The MAZ calculation tracked the evolution of the radioactive isotopes and their attachment to dust particles, and was similar to the demonstration run reported in Hassig et al. (1992). The total amount of radioactive material released in the explosion is approximately 1kg. Figure 6-1 shows the vertical distribution of the radioactive mass for particles smaller than 1mm, and also the distribution by particle size. The activity is confined to the main cloud, centered at 6km altitude, and is mostly carried by the particles smaller than 30 μ m. There is a small fraction of the radioactivity carried by particles larger than 1mm, but these particles are deposited very close to the burst location. The subsequent transport and diffusion of the smaller particles in the atmosphere was treated as a passive process, with the exception of gravitational settling. The high resolution wind fields provided by the ANATEX data (see Section 3) were used to transport the cloud from a release location of 42°N 88°W. The wind vectors at four altitudes over the region of interest are displayed in Figure 6-2.

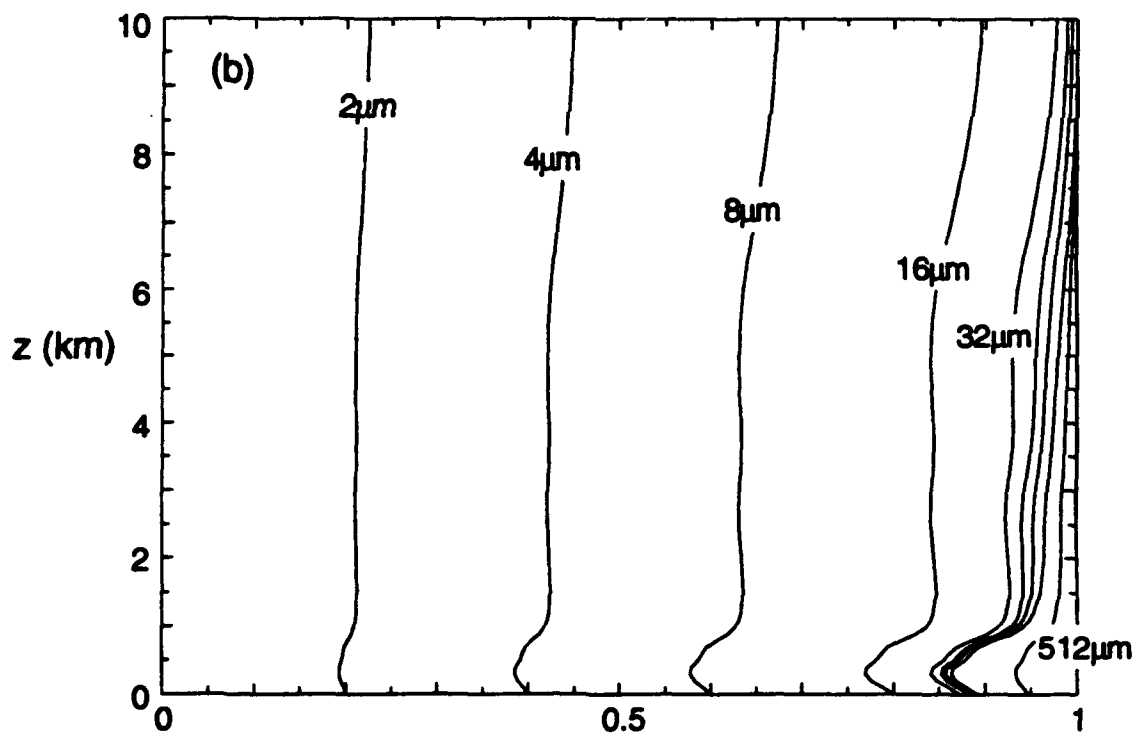
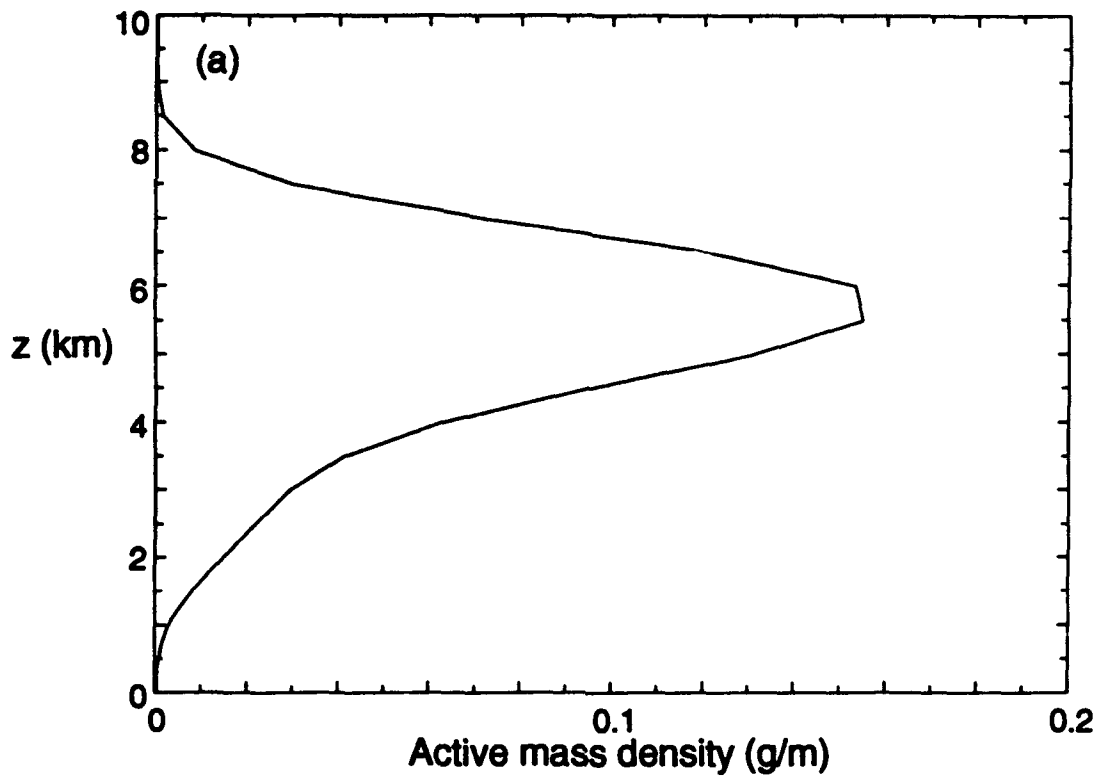


Figure 6-1. Distribution of radioactive material at $t=5$ mins. (a) vertical distribution of active mass; (b) distribution by particle size, contours indicate fraction of mass contained in particles smaller than the indicated diameter.

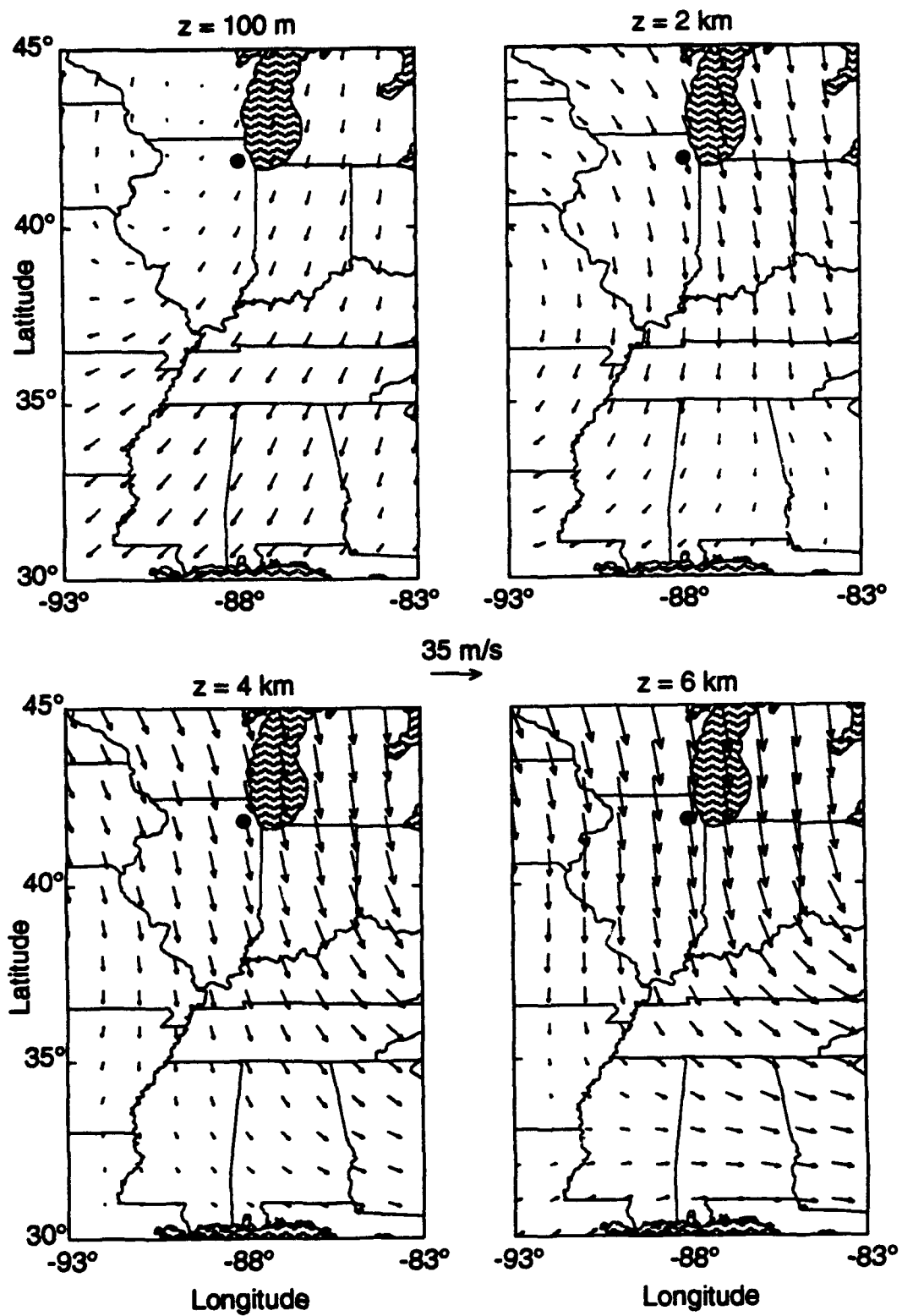


Figure 6-2. Initial wind field for the SCIPUFF simulation

The winds aloft show a strong Northerly flow while the low level winds near the release point are light and variable.

The mean cloud at $t = 8$ hours and two altitudes is shown in Figure 6-3. The cross section at $z = 100\text{m}$ shows a widely spread cloud while the section at 5km shows a more compact cloud transported further South over Tennessee. The elongation of the low altitude cloud is a result of the strong wind shear between the surface and 5km . The standard deviation of the expected concentration value is also indicated in Figure 6-3, and is comparable with the mean value. The accumulated surface dose after 8 hours in μgm^{-2} of radioactive material is shown in Figure 6-4, and shows the same elongation toward the South as the mean concentration at $z=100\text{m}$. There is some Northward transport in the light winds around the source, but the higher altitude winds transport the larger particles Southward before they fall to the ground.

The mean radiation dose from the deposited material close to the source after 8 hours is shown in Figure 6-5. We have converted the mass deposition to equivalent radiation at 1hr using a conversion factor of $10 \text{ rad/hr per } 1\mu\text{gm}^{-2}$ (R. Christian, personal communication). The high doses are concentrated in a plume extending to the South-East and are caused by the fallout of the larger particles. The very low level contamination to the North-West in Figure 6-3 results from small particles near the surface with little radioactive material. The statistical prediction can be used to assess the probability of exceeding a particular dose level. This uncertainty is a result of the incomplete knowledge of the wind field as represented in Figure 6-2 and is characterized by the concentration fluctuation variance. Figure 6-6 shows the probability of exceeding a dose of 0.1 rad/hr and 10rad/hr at 1hr.

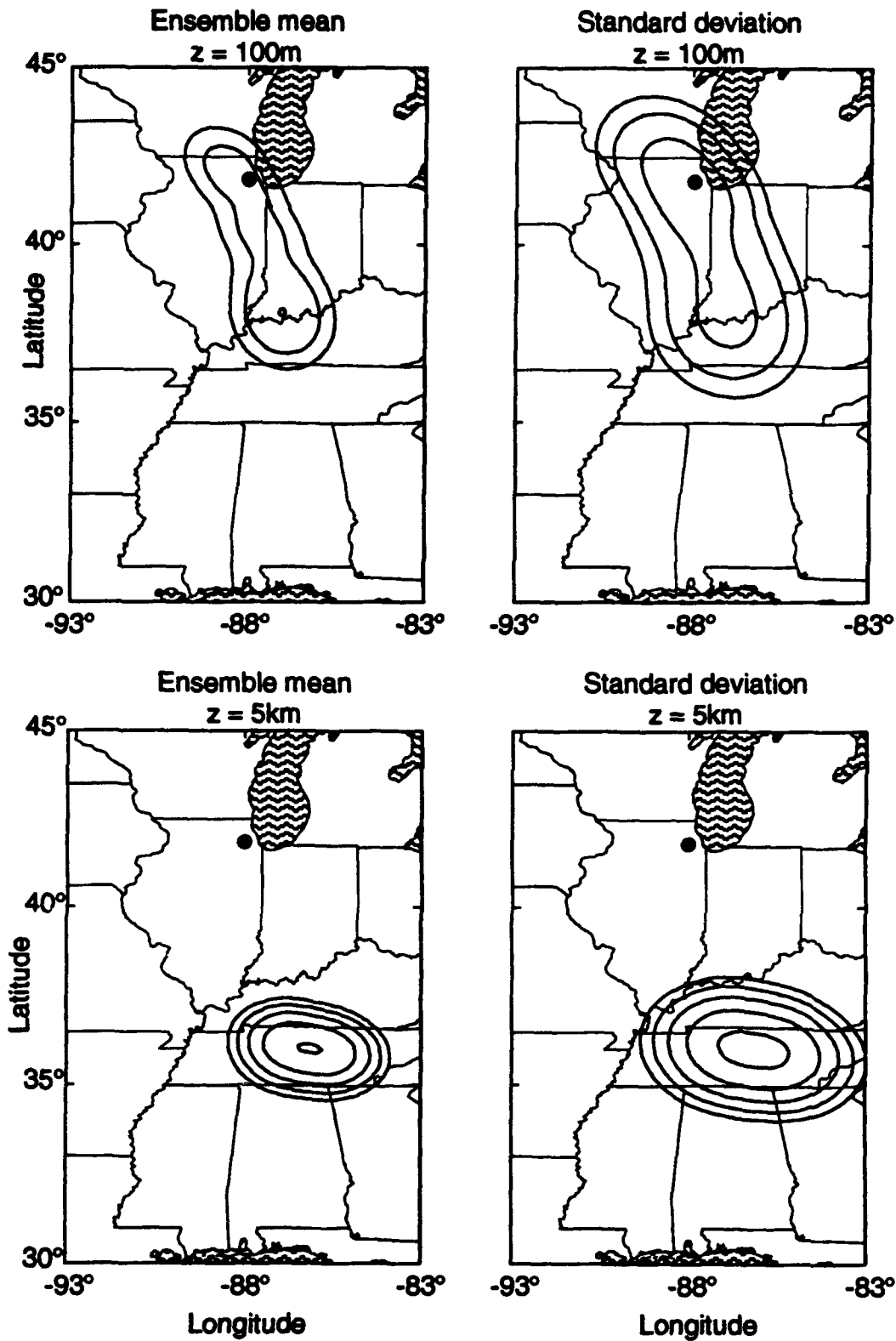


Figure 6-3. SCIPUFF prediction of the total dust concentration at $z=100\text{m}$ and $z=5\text{km}$ at 8 hours after initiation of a 20kT burst centered at $42^\circ\text{N}, 88^\circ\text{W}$. Contour levels of 10^{-3} , 10^{-2} , 10^{-1} , 1 and $10 \mu\text{g}/\text{m}^3$.

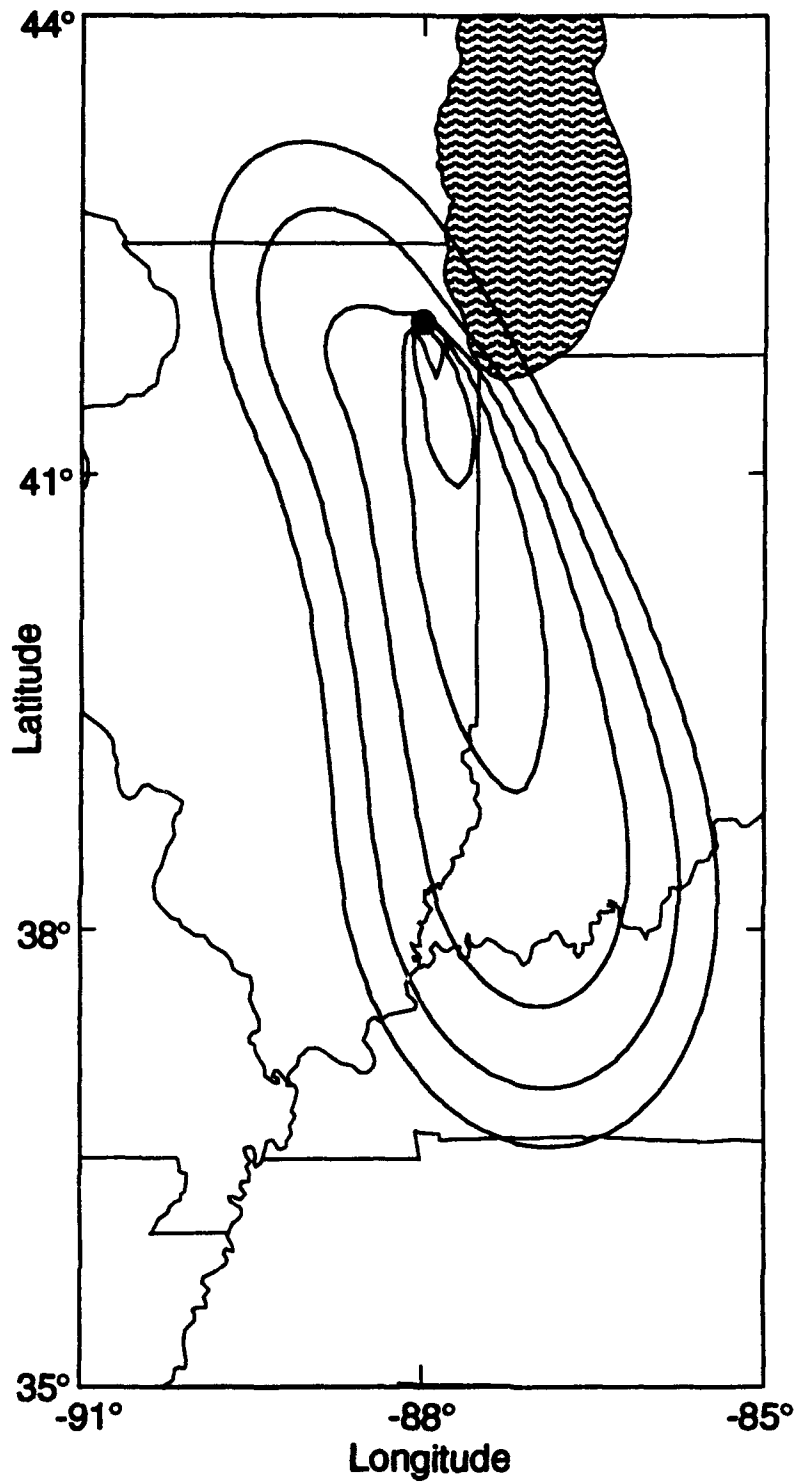


Figure 6-4. SCIPUFF prediction of the ensemble mean surface dose 8 hours after initiation of a 20kT burst centered at 42°N,88°W. Contour levels of 10^{-7} , 10^{-6} , 10^{-5} , 10^{-4} , 10^{-3} and 10^{-2} $\mu\text{g}/\text{m}^2$.

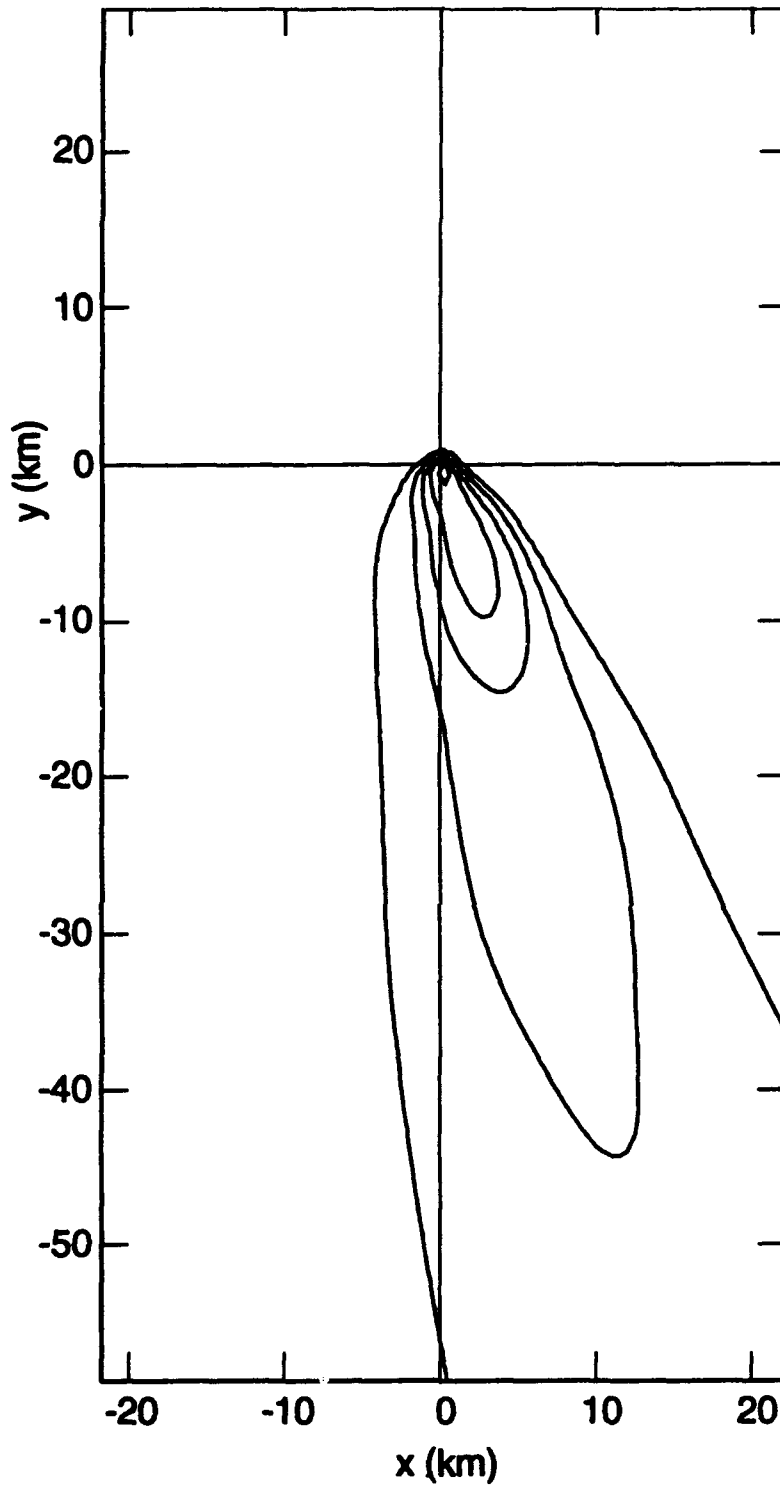


Figure 6-5. SCIPUFF prediction of the ensemble mean surface radiation dose 8 hours after initiation of a 20kT burst. Contour levels of .01, .1, 1, 10 and 100 rad/hr.

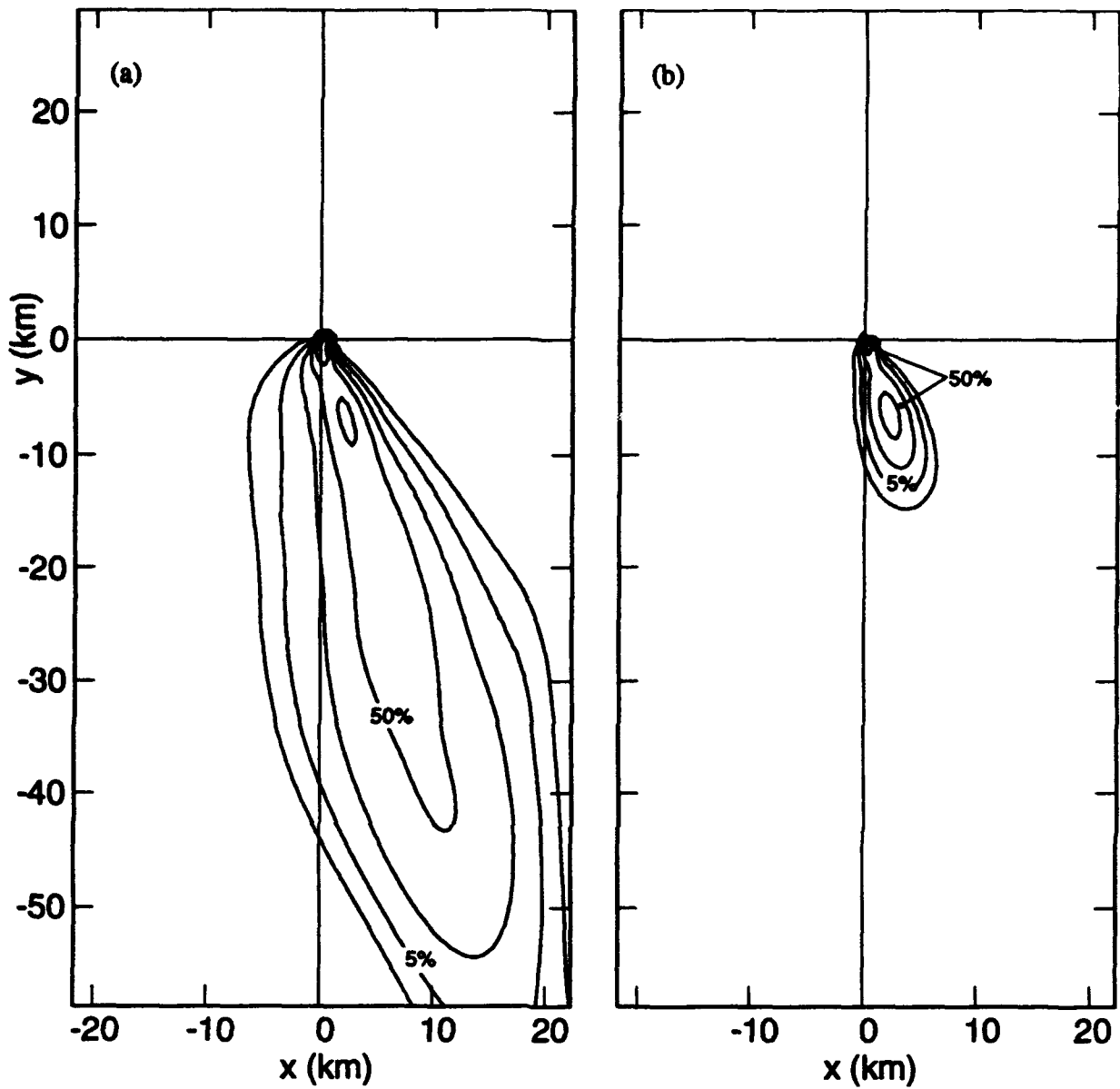


Figure 6-6. SCIPUFF prediction of the probability of exceeding a surface radiation dose of (a) 0.1 rad/hr and (b) 10 rad/hr 8 hours after initiation of a 20kT burst. Contour levels of 1%, 5%, 20%, 50%, 80% 100%.

6.2 NUCLEAR POWER PLANT RELEASE SENSITIVITIES.

In the event of a nuclear power plant explosion, either accidental or as a result of intentional attack, the release of radioactive material into the atmosphere causes hazardous conditions for human activity. The hazards range from intense radiation exposure close to the source all the way to large-area and long-term health effects due to radioactive fallout. The capability to predict the environmental effects of a nuclear plant release following an explosive event is an important planning tool, involving a source estimate, an atmospheric dispersion prediction, and a health effects model. In order to assist in the requirement definition for the source calculation, it is instructive to examine the subsequent atmospheric processes and their effects on the radioactive cloud. The question addressed here is the following: how detailed a description of the initial, local environment do we need to be able to reasonably estimate the long range (10-1000km), long term (hours-days) consequences? SCIPUFF has been run for a variety of scenarios in an effort to assess the sensitivity to source details. The matrix of SCIPUFF runs included variations in the meteorology, release point, and source characteristics. The meteorology variations included different wind fields, release points, and release times.

The wind fields were taken from the National Meteorological Center's Nested Grid Model (NGM) output. The data is available every 2 hours for the first quarter of 1987, being archived as part of ANATEX (Across North America Tracer EXperiment, see Section 3). A standard boundary layer was uniformly imposed over the entire domain and exhibited a diurnal variation with a depth of 50m during the night and a maximum depth of 1000m during the day in January and February, and 1500m during March. These are typical values for the planetary boundary layer and were used in the SCIPUFF validation study performed with the ANATEX data.

Three wind field data sets, each covering 60 hours, were used:

01/07/87:00:00 - 01/09/87:12:00

02/04/87:00:00 - 02/06/87:12:00

03/04/87:00:00 - 03/06/87:12:00.

All times referred to in this study are Central Standard Time.

Releases were made from two locations, central Illinois (90°W, 40°N) and the Four Corners area of Colorado (109°W, 37°N) for both a midnight (00:00CST) and noon (12:00CST) explosion. The locations were chosen to give a broader variation of wind

fields and the release times give a sensitivity to diurnal variations. The possible range of meteorological conditions is obviously very wide indeed, but this limited sample should provide some insight into the variability.

The puff source is defined by five parameters; initial cloud size and height, duration and rate of release and release material. The size, rate and duration were kept fixed for all runs. All releases were for 12 hours with a release rate of 1.0 kg/s, simulating an extended release at constant rate. The Gaussian puffs were initialized with a spread (σ) of 50m. Four release heights were used: 200m, 500m, 1000m, and 2000m. Four different source materials were also considered with different deposition and settling rates. Settling refers to the equilibrium fall speed under the influence of gravity, while deposition rate is the speed at which surface absorption occurs. In this study, we have ignored turbulent deposition of particulates but used a standard value of 1cm/s for the gaseous contaminant.

Table 6-1. Deposition rates and settling velocities for contaminant species.		
Type	Deposition Rate	Settling Velocity
Gaseous	1.0 cm/s	0.0 cm/s
10 μ m particle	0.0	0.7
30 μ m particle	0.0	6.3
100 μ m particle	0.0	52.2

The surface dose was computed on a coarse grid (20 km spacing) covering most of the continental United States at 24 and 48 hours after the start of the release. The surface doses at 48 hours for the release of a gaseous material at 500m for each of the 3 days and 2 times of day are shown in Figure 6-7 for the Illinois source and in Figure 6-8 for the Four Corners source. The extent of the surface pattern, measured by the area with a dose greater than 10^{-4} mg/m² or the total mass contained within that area varies by about a factor of 2 excluding the 2/4/87 Four Corners releases. These cases show a much smaller plume-like pattern but also left the surface grid to the west. The time of day of the release (00:00 vs. 12:00) does not significantly affect the amount of material reaching the surface. Figure 6-9 shows the surface dose at 48 hours for noon releases on 2/4/87 at

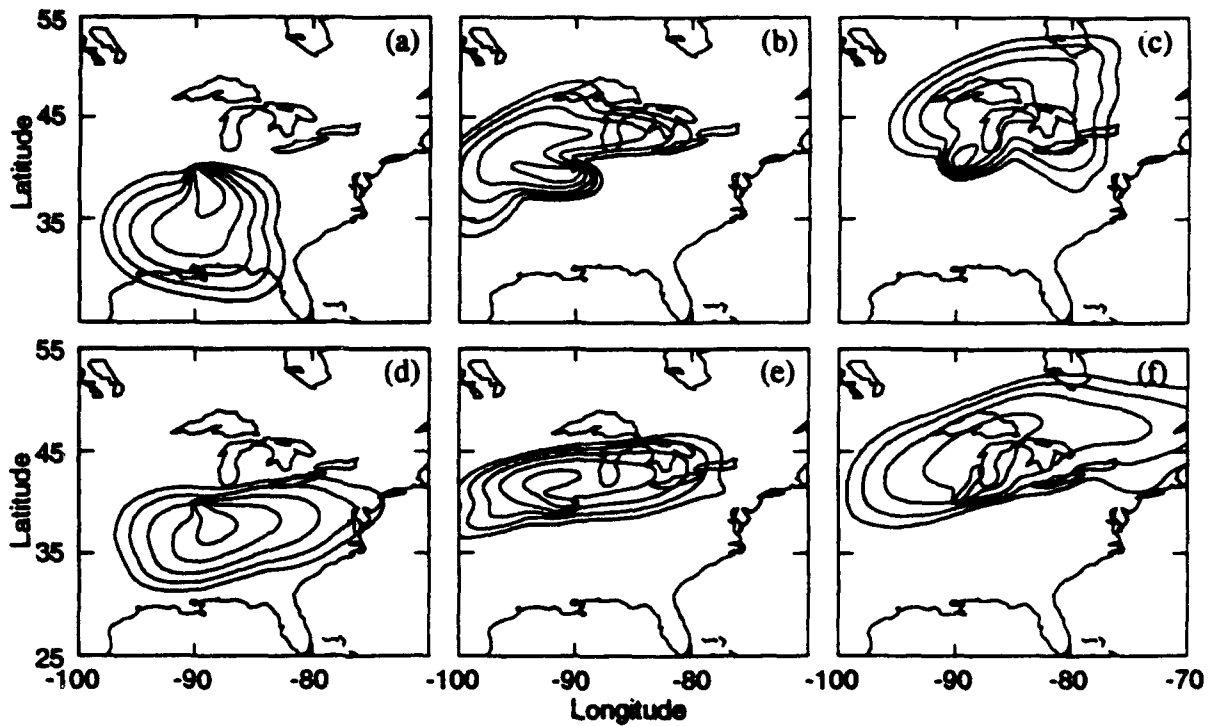


Figure 6-7. Surface dose at 48 hours after the release of a gaseous material at 500m from the Illinois source. Release start at (a) 01/07/87:00:00, (b) 02/04/87:00:00, (c) 03/04/87:00:00, (d) 01/07/87:12:00, (e) 02/04/87:12:00, (f) 03/04/87:12:00. Contour levels of 10^{-5} , 10^{-4} , 10^{-3} , 10^{-2} , 10^{-1} and 1 mg/m^2 .

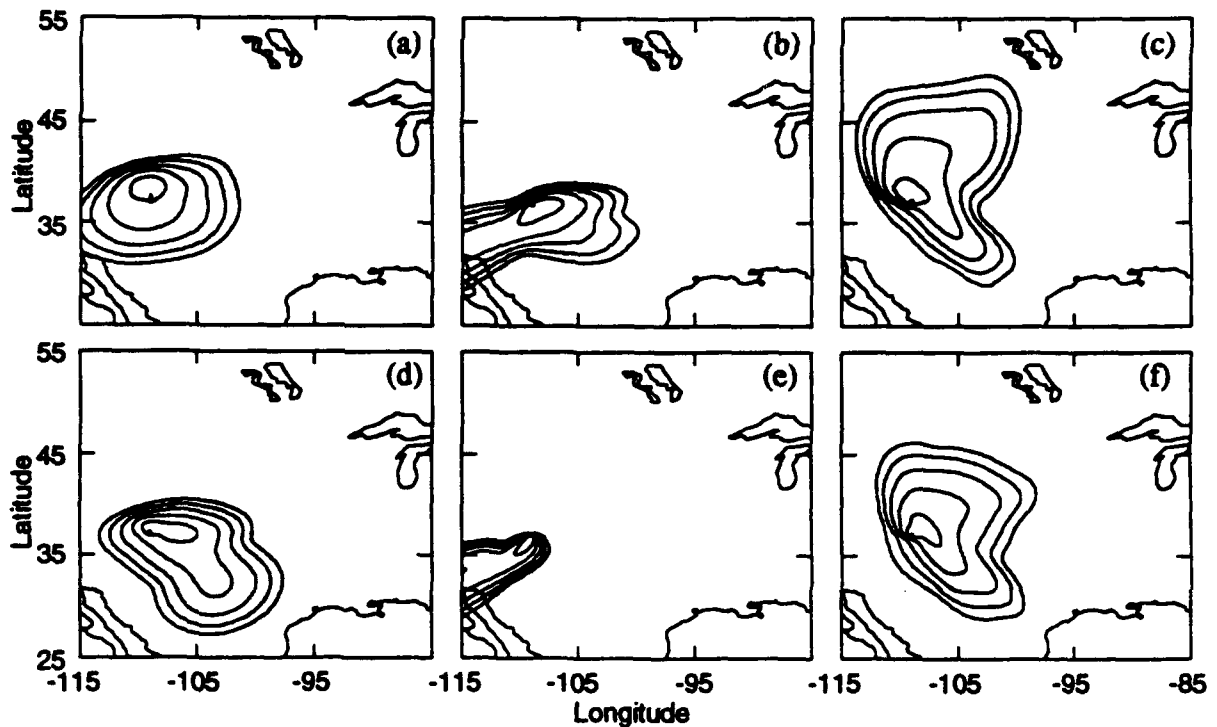


Figure 6-8. Surface dose at 48 hours after the release of a gaseous material at 500m from the Four Corners source. Release start at (a) 01/07/87:00:00, (b) 02/04/87:00:00, (c) 03/04/87:00:00, (d) 01/07/87:12:00, (e) 02/04/87:12:00, (f) 03/04/87:12:00. Contour levels of 10^{-5} , 10^{-4} , 10^{-3} , 10^{-2} , 10^{-1} and 1 mg/m^2 .

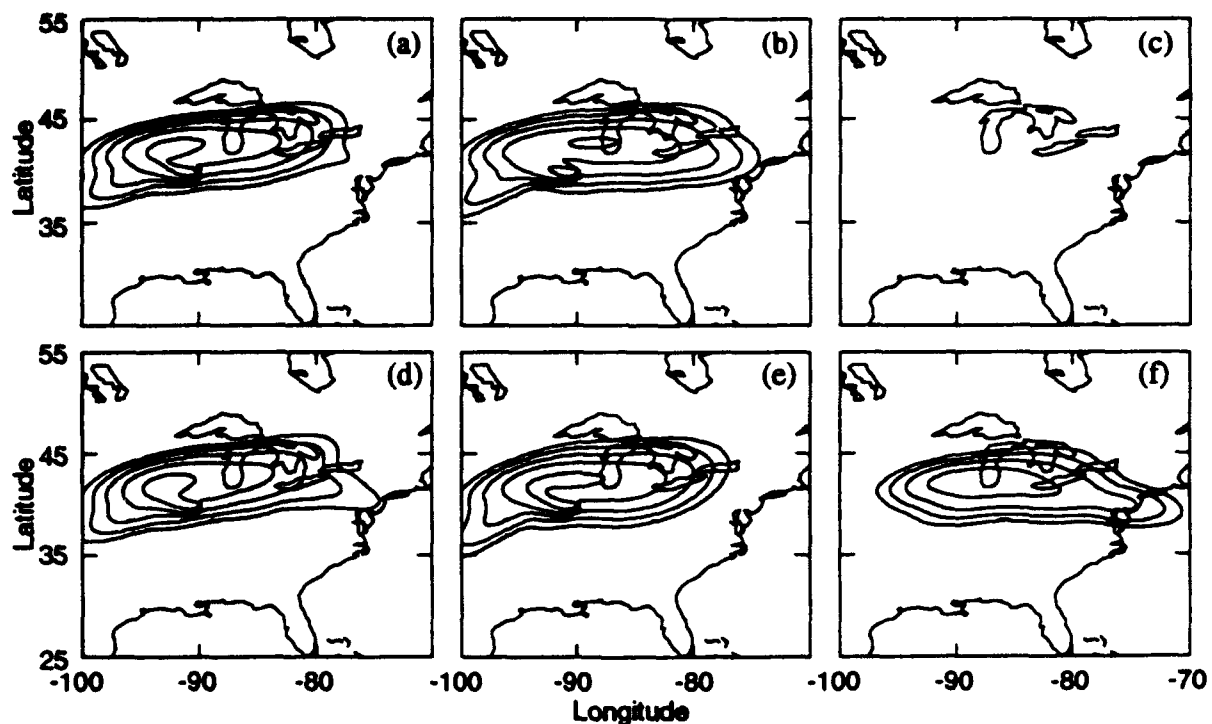


Figure 6-9. Surface dose at 48 hours after the release on 02/04/87 at 12:00 from the Illinois source. Release of (a) gas at 500m, (b) gas at 1000m, (c) gas at 2000m, (d) $10\mu\text{m}$ at 500m, (e) $10\mu\text{m}$ at 1000m, (f) $10\mu\text{m}$ at 2000m. Contour levels of 10^{-5} , 10^{-4} , 10^{-3} , 10^{-2} , 10^{-1} and 1 mg/m^2 .

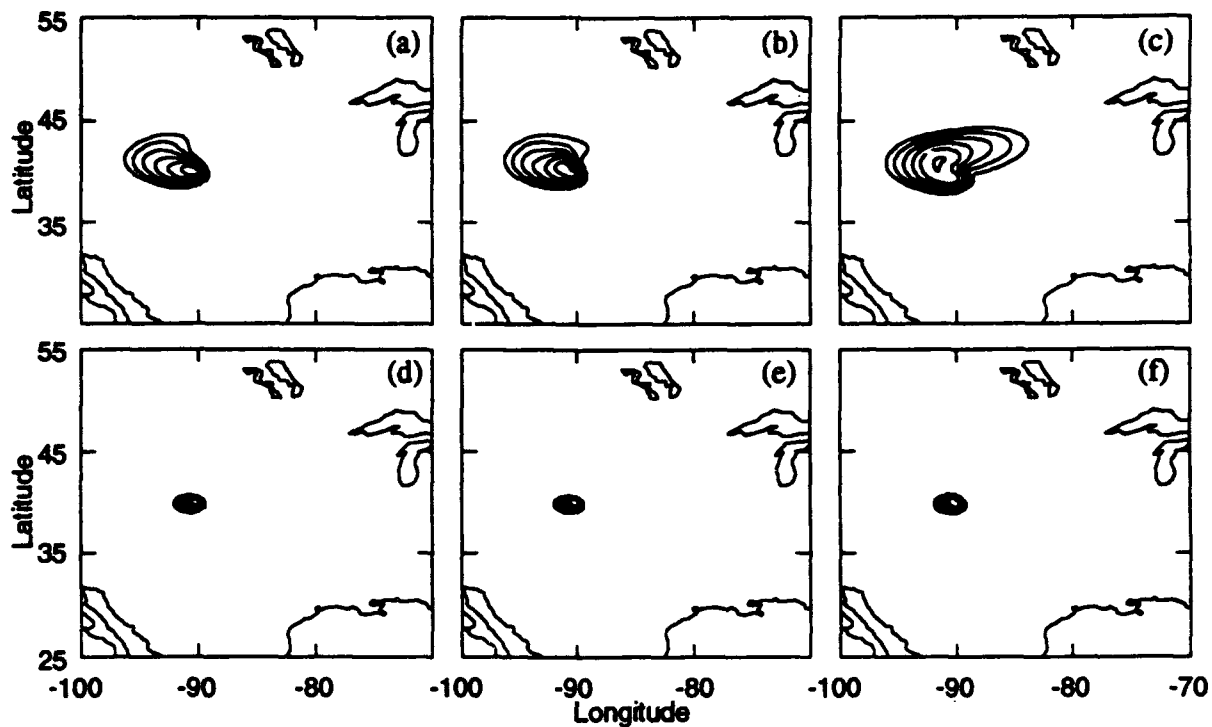


Figure 6-10. Surface dose at 48 hours after the release on 02/04/87 at 12:00 from the Illinois source. Release of (a) $30\mu\text{m}$ at 500m, (b) $30\mu\text{m}$ at 1000m, (c) $30\mu\text{m}$ at 2000m, (d) $100\mu\text{m}$ at 500m, (e) $100\mu\text{m}$ at 1000m, (f) $100\mu\text{m}$ at 2000m. Contour levels of 10^{-5} , 10^{-4} , 10^{-3} , 10^{-2} , 10^{-1} and 1 mg/m^2 .

the central Illinois site for several release heights and both a gaseous contaminant and a 10 μ m particulate. Figure 6-10 shows the same information for the larger particle releases. The gaseous and 10 μ m particle releases show nearly identical surface patterns and show little variation with height of release provided the release is within the mixed layer (<1000m). For releases above the mixed layer, the gaseous release, which is dependent on turbulent mixing to bring the material to the surface, does not impact the surface while the 10 μ m particles eventually fall into the mixed layer and are mixed to the surface. The largest particles (100 μ m) are not dependent on mixing to get to the surface and show little or no effect of release height or meteorology.

The surface dose was also computed on a finer grid (2 km spacing) covering the vicinity of the source at 4 and 8 hours after the start of the release. The surface dose at 8 hours for the release of a gaseous material at 200m for each of the 3 days, and 2 times of day is shown in Figure 6-11 (Illinois source) and Figure 6-12 (Four Corners source). The variations in the extent of the surface pattern are somewhat less than a factor of 2 if measured by the area greater than 10⁻² mg/m² but greater than a factor of 2 if measured by the mass. We should note that the effect of wind uncertainty is evident in the relatively wide spread of the plume. The wind field is only defined on a coarse grid and therefore contains significant uncertainty on the smaller scales. Expected concentrations for a particular event would be higher than those appearing in the figures, since these represent an average impact at each location from all possible wind fields. The expected concentration may display more sensitivity to source conditions, but we would not expect strong sensitivity at the ranges and transport times used in this study. Small-scale turbulence will effectively spread the plume at a rate of order 1m/s over the first hour, so variations in source size of 10's of meters will be negligible, in general. Figures 6-13 and 6-14 show the surface doses at 8 hours for noon releases on 2/4/87 at the central Illinois site for three release heights and the four release materials while Figures 6-15 and 6-16 show the surface doses for a night release. Close in, the effects of release height and time of release are more apparent for the gaseous and small particle releases. For the larger particles release height makes little difference but shows some effect of the meteorology.

In summary, the most important source factors governing the environmental prediction are the release rate and duration, and the release height. The type of material, i.e., gaseous or particulate can also be important in determining the timescales of interest for the atmospheric transport. Larger particles (diameters >30 μ m) will fall out relatively quickly near the source and will be less influenced by the meteorology. The mass release

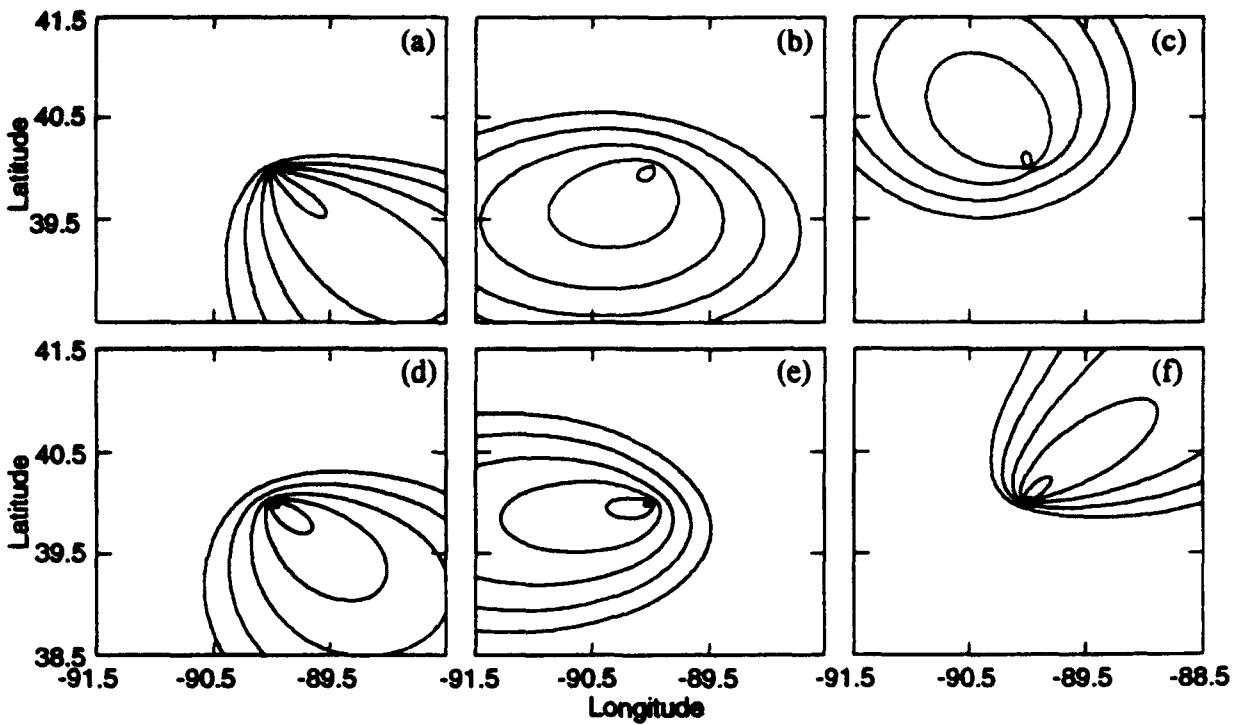


Figure 6-11. Surface dose at 8 hours after the release of a gaseous material at 200m from the Illinois source. Release start at (a) 01/07/87:00:00, (b) 02/04/87:00:00, (c) 03/04/87:00:00, (d) 01/07/87:12:00, (e) 02/04/87:12:00, (f) 03/04/87:12:00. Contour levels of 10^{-4} , 10^{-3} , 10^{-2} , 10^{-1} , 1 and 10 mg/m^2 .

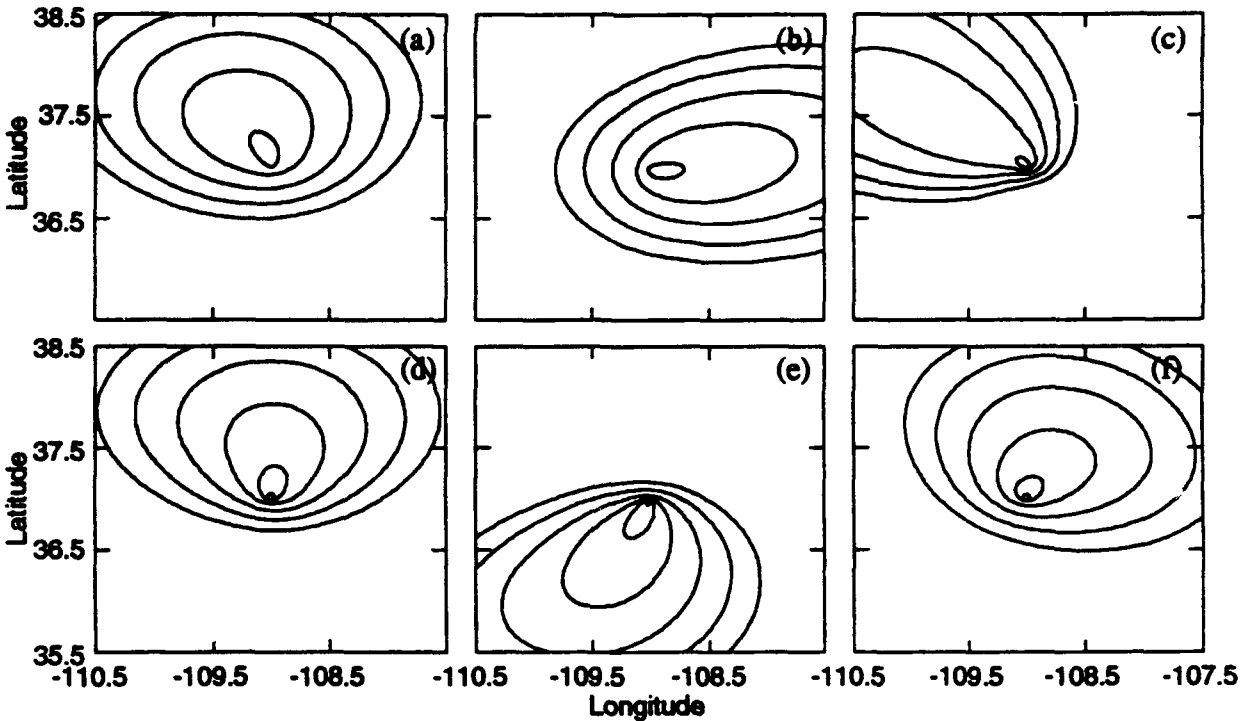


Figure 6-12. Surface dose at 8 hours after the release of a gaseous material at 200m from the Four Corners source. Release start at (a) 01/07/87:00:00, (b) 02/04/87:00:00, (c) 03/04/87:00:00, (d) 01/07/87:12:00, (e) 02/04/87:12:00, (f) 03/04/87:12:00. Contour levels of 10^{-4} , 10^{-3} , 10^{-2} , 10^{-1} , 1 and 10 mg/m^2 .

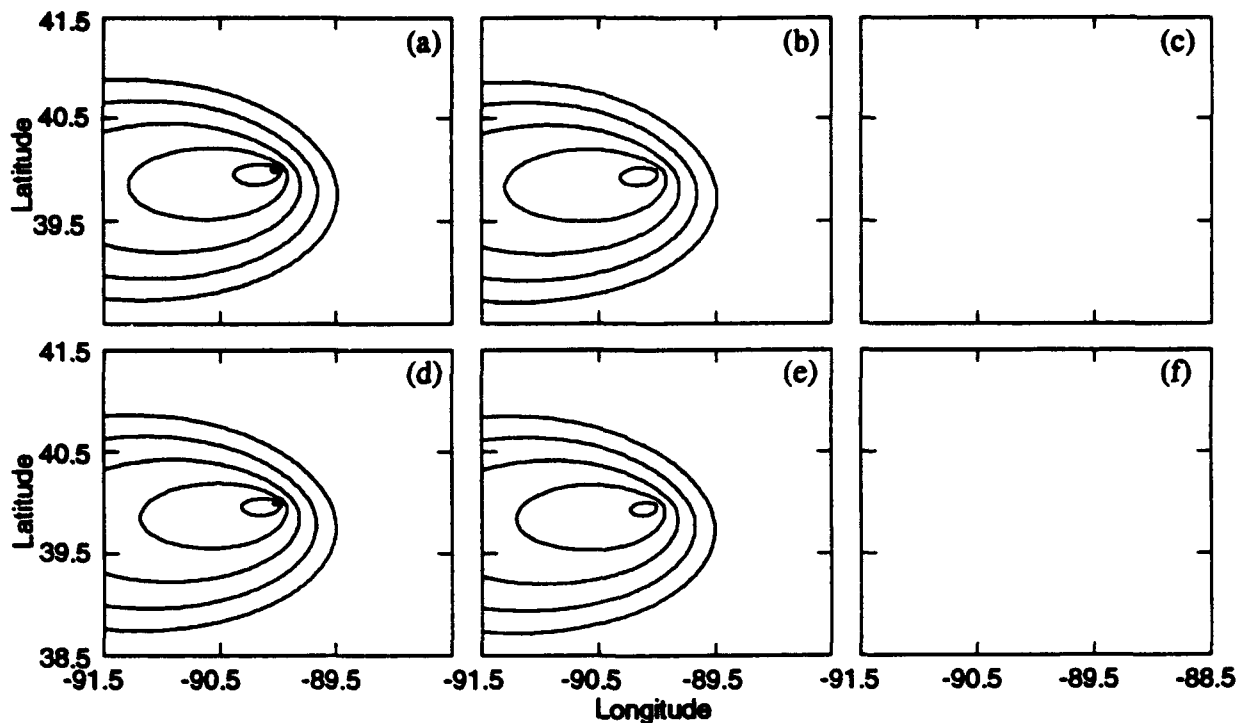


Figure 6-13. Surface dose at 8 hours after the release on 02/04/87 at 12:00 from the Illinois source. Release of (a) gas at 200m, (b) gas at 1000m, (c) gas at 2000m, (d) $10\mu\text{m}$ at 200m, (e) $10\mu\text{m}$ at 1000m, (f) $10\mu\text{m}$ at 2000m. Contour levels of 10^{-4} , 10^{-3} , 10^{-2} , 10^{-1} , 1 and 10 mg/m^2 .

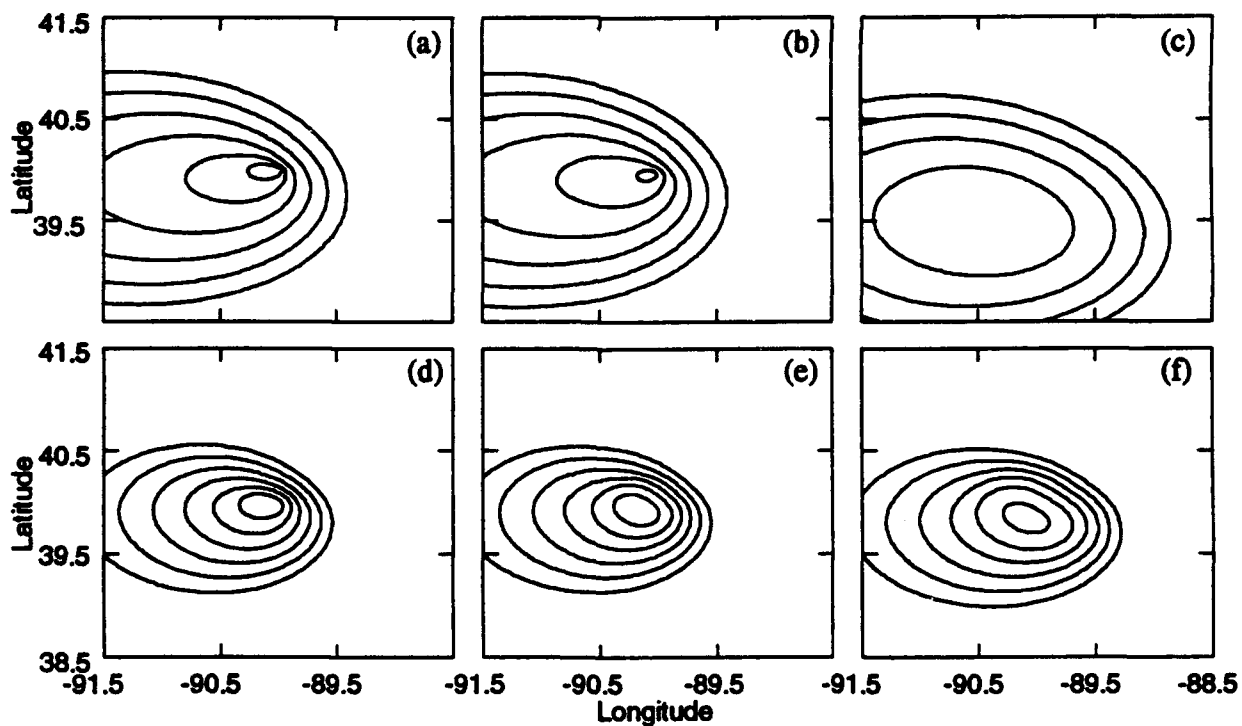


Figure 6-14. Surface dose at 8 hours after the release on 02/04/87 at 12:00 from the Illinois source. Release of (a) $30\mu\text{m}$ at 200m, (b) $30\mu\text{m}$ at 1000m, (c) $30\mu\text{m}$ at 2000m, (d) $100\mu\text{m}$ at 200m, (e) $100\mu\text{m}$ at 1000m, (f) $100\mu\text{m}$ at 2000m. Contour levels of 10^{-4} , 10^{-3} , 10^{-2} , 10^{-1} , 1 and 10 mg/m^2 .

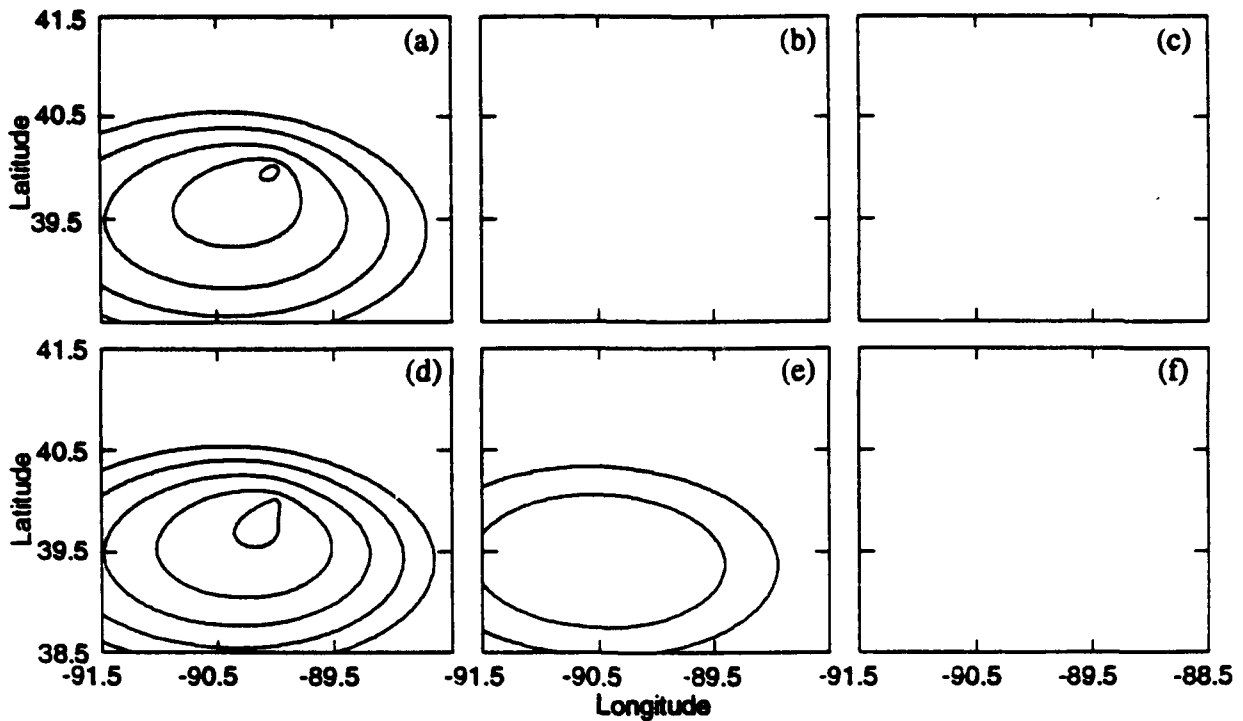


Figure 6-15. Surface dose at 8 hours after the release on 02/04/87 at 00:00 from the Illinois source. Release of (a) gas at 200m, (b) gas at 500m, (c) gas at 1000m, (d) 10 μ m at 200m, (e) 10 μ m at 500m, (f) 10 μ m at 1000m. Contour levels of 10⁻⁴, 10⁻³, 10⁻², 10⁻¹, 1 and 10 mg/m².

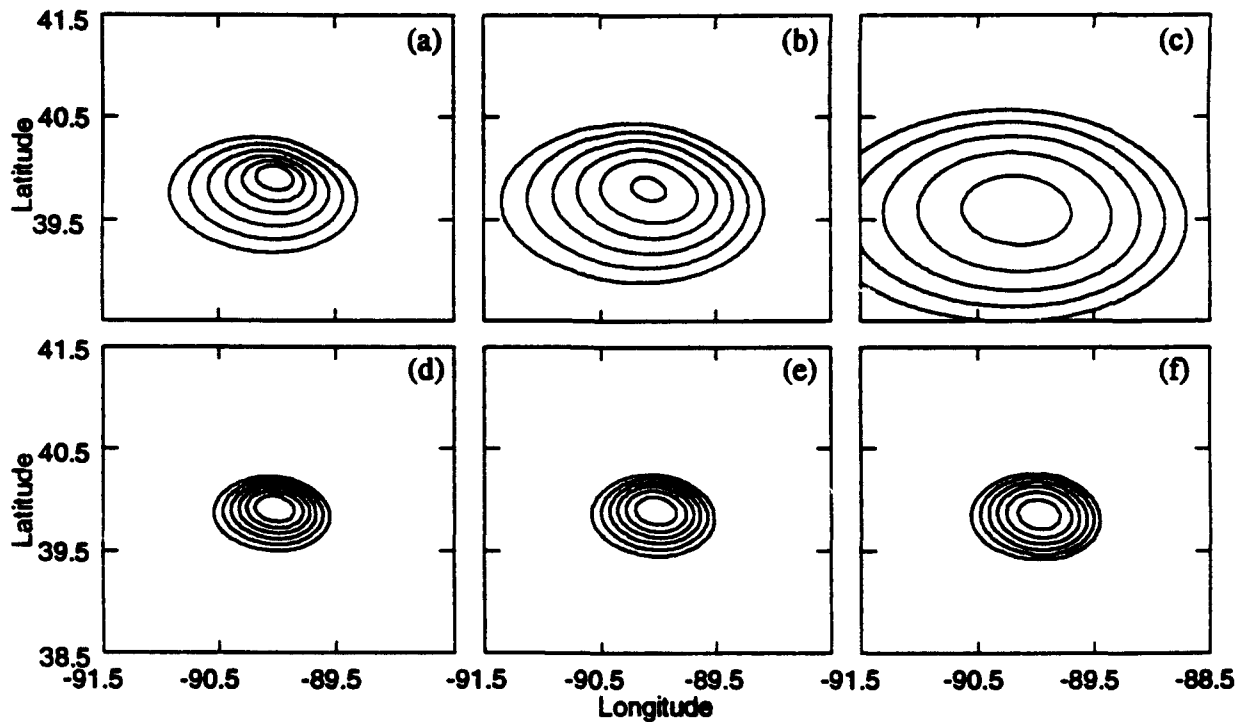


Figure 6-16. Surface dose at 8 hours after the release on 02/04/87 at 00:00 from the Illinois source. Release of (a) 30 μ m at 200m, (b) 30 μ m at 500m, (c) 30 μ m at 1000m, (d) 100 μ m at 200m, (e) 100 μ m at 500m, (f) 100 μ m at 1000m. Contour levels of 10⁻⁴, 10⁻³, 10⁻², 10⁻¹, 1 and 10 mg/m².

rate is a scale factor, i.e., double the release rate gives twice the concentration everywhere, but the quantitative assessment of the consequences of an actual release clearly requires a reasonably accurate definition of the release mass.

The release height is one of the important parameters for the dispersion calculation. For long range transport over time periods of many hours, the key factor is whether the release is within the planetary boundary layer. A gaseous release above the boundary layer will take a long time to diffuse vertically and may not reach the surface unless it encounters deep mixing, e.g., in the vicinity of convective clouds. Conversely, a release within the turbulent boundary layer will be quickly mixed throughout the depth of the layer and is therefore only sensitive to the initial height very close to the source. This region of sensitivity extends a few release heights downstream, since the vertical turbulent velocity fluctuations are generally some fraction of the mean wind speed, and is therefore of the order of a few hundred meters to a few kilometers. Beyond this range, the contaminant will be well-mixed under normal daytime conditions.

For nocturnal releases, the short term prediction is critically dependent on the description of the boundary layer. Details of the boundary layer are not generally available, so our knowledge of the vertical structure is rarely more reliable than a few hundred meters. It seems inappropriate for a source description to be more accurate than this.

SECTION 7

CONCLUDING REMARKS

The focus of this report has been the development and improvement of techniques for predicting the late-time dispersion of nuclear clouds in the atmosphere, with particular emphasis on the characterization of the uncertainties associated with such a prediction. Our knowledge of the state of the atmosphere, either in real time or at some future time, is inevitably limited, and this inability to specify the complete wind field generally leads to large uncertainty in any forecast of dispersion. In many instances, the range of the prediction errors is comparable to or larger than the predicted value so it is very important to be able to describe the statistical distribution of these errors. The errors cannot be reduced without more detailed information about the atmosphere, and since this is a formidable or even impossible (in the case of future scenarios) task, it is important that a probabilistic prediction capability be developed.

The basis of the probabilistic prediction methodology reported herein is the second-order turbulence closure framework as embodied in the SCIPUFF model, which uses a prognostic equation for the variance in the predicted concentration level to assess the level of uncertainty in any predicted quantity. The model has been extended to describe large scale atmospheric dispersion, using the GASP velocity fluctuation data of Nastrom and Gage (1985) and the velocity spectra distribution concepts of Gifford (1988). Although limited in their representation of atmospheric variability, since the GASP measurements were taken by commercial aircraft on international flights, these data provide an initial foundation on which to build a rational description of long range dispersion. Furthermore, Bauer (1983) concludes that the dispersion characteristics of the atmosphere do not vary markedly with altitude, so that the aircraft cruise altitude data can be used as a general basis for horizontal dispersion.

In addition to the improvement in the turbulence specification, the Gaussian puff description in SCIPUFF has been extended to include a completely general spatial second-moment evolution equation. This allows individual puffs to distort under the action of wind shear without artificially diffusing the concentration field or allowing neighboring puffs to separate from one another, leaving gaps in the initially continuous cloud. The capability of the new scheme to describe the persistent action of shear on an

isolated cloud was demonstrated in the 'Dust-Off' model comparison exercise, where contours of the concentration field after 8 hours transport showed a smoothly continuous distribution extending over 1000km in the horizontal. The model comparison statistics were not compiled as part of this study, but the treatment of wind shear was one of the most sensitive aspects of the various model approaches. Maintaining a strongly sheared cloud without artificial diffusion is a difficult numerical requirement, but is a prevalent feature of high altitude dispersion.

Model evaluation is always a vital part of the development of a predictive capability. Field data on atmospheric dispersion over scale of hundreds to thousands of kilometers is relatively sparse, however, making it difficult to quantitatively assess the accuracy of a model. The Across North America Tracer Experiment (ANATEX) provides a uniquely extensive data base for model evaluation at continental scale, since data were taken on an extensive network over a period of three months. This experiment, sponsored by NOAA, used specialized tracers detectable at very low concentrations with periodic surface releases throughout the experiment. In addition, NOAA provided detailed wind fields for model evaluation purposes. SCIPUFF was used to simulate the entire experimental period and the statistical distributions of concentrations were compared with the observations. The model showed good agreement with the observed 24-hour average concentrations as a function of distance from the source, and also showed good agreement with the short-term aircraft samples obtained on flights through the plume. SCIPUFF also showed some skill in predicting the observed distributions using only a single statistical average description of the wind field over the entire continent for the three month period. The evaluation exercise demonstrated the capability of the model in predicting concentration distributions for both long-term and short-term averages, and also indicates some skill using very limited wind data.

Several studies are reported in the preceding sections that demonstrate the feasibility of a quantitative treatment of uncertainty in atmospheric dispersion predictions. The ANATEX evaluation exercise provides some real data for comparison with SCIPUFF concentration predictions, but the probabilistic framework clearly has wider applicability and requires further validation. The general basis for the SCIPUFF prediction of turbulent boundary layer dispersion now seems to be established on scales ranging from several kilometers to thousands of kilometers, but there are a number of areas where further development is required. For example, our understanding of the variation in the one-point probability distribution function with averaging time and

transport distance could be improved. The ANATEX results suggest that the clipped-normal distribution is valid for short term samples, but long term averages are better approximated as log-normal. A second area of research is the high altitude shear-dominated regime, where the vertical diffusion is suppressed by the atmospheric stability. There is little data available from this regime, and our extension of the prediction methodology from the relatively well-understood turbulent lower atmosphere is not based on solid understanding.

In summary, therefore, we have demonstrated a practical methodology for the prediction of late-time dispersion in a probabilistic framework. The SCIPUFF model is capable of providing routine forecasts of concentrations from arbitrary sources together with a statistical assessment of the possible impact. The model has been validated on a wide range of horizontal scales, using surface tracer data, and shows good agreement with concentration measurements. The probabilistic framework should be extended and improved for use in general dispersion calculations, and the evaluation studies should be continued.

SECTION 8

REFERENCES

- Bauer, E. (1983), "The growth and disappearance of tracer clouds in the atmosphere", Institute for Defense Analyses, Science and Technology Division, IDA Note N-890. (UNCLASSIFIED)
- Friedlander, S. K. (1977), "*Smoke, Dust and Haze*", Wiley, 317pp. (UNCLASSIFIED)
- Gifford, F.A. (1959), "Statistical properties of a fluctuating plume dispersal model", *Adv. Geophys.*, **6**, 117-137. (UNCLASSIFIED)
- Gifford, F. A. (1988), "A similarity theory of the tropospheric turbulence energy spectrum", *J. Atmos. Sci.*, **45**, 1370-1379. (UNCLASSIFIED)
- Hassig, P. J., D. W. Hatfield, R. J. Schlamp, C. T. Nguyen, P. Hookham and M. Rosenblatt (1992), "Advances in nuclear cloud modeling", Defense Nuclear Agency, DNA-TR-92-23. (UNCLASSIFIED)
- Jeffreys, H. (1963), "*Cartesian tensors*", Cambridge University Press, Cambridge, 92pp. (UNCLASSIFIED)
- Lewellen, W. S. and Y. P. Sheng (1980), "Modeling of dry deposition of SO₂ and sulfate aerosols", Electric Power Research Institute, EA-1452. (UNCLASSIFIED)
- Lewellen, W. S., R. I. Sykes, S. F. Parker and D. S. Henn (1991), "The introduction of cloud microphysics into SCIPUFF", DNA-TR-90-90. (UNCLASSIFIED)
- Lovejoy, S. (1982), "Area-perimeter relation for rain and cloud areas", *Science*, **216**, 185-187. (UNCLASSIFIED)
- Nastrom, G. D. and K. S. Gage (1985), "A climatology of atmospheric wavenumber spectra of wind and temperature observed by commercial aircraft", *J. Atmos. Sci.*, **42**, 950-960. (UNCLASSIFIED)

Pasquill, F. (1974), "*Atmospheric Diffusion*", Ellis Horwood, Chichester, 429pp.
(UNCLASSIFIED)

Ross, R.F. (1991) Letter report to Maj. D. Wade, SPWE, DNA. March 21.
(UNCLASSIFIED)

Ross, R. F. and T. A. Mazzola (1993), "Statistical avoidance of fratricide exclusion regions", Defense Nuclear Agency, DNA-TR-92-168. (UNCLASSIFIED)

Sykes, R.I. (1984), "The variance in time-averaged samples from an intermittent plume", *Atmos. Env.*, 18, 121-123. (UNCLASSIFIED)

Sykes, R. I., W. S. Lewellen, S. F. Parker and D. S. Henn (1988), "A hierarchy of dynamic plume models incorporating uncertainty, Volume 4: Second-order Closure Integrated Puff", EPRI, EA-6095 Volume 4. (UNCLASSIFIED)

APPENDIX

Numerical Simulation of ANATEX Tracer Data using a Turbulence Closure Model for Long-Range Dispersion

by

R. I. Sykes, S. F. Parker, D. S. Henn and W. S. Lewellen

reprinted from the *Journal of Applied Meteorology*,

Vol. 32, No. 5, May 1993, pp 929-947.

Numerical Simulation of ANATEX Tracer Data Using a Turbulence Closure Model for Long-Range Dispersion

R. I. SYKES, S. F. PARKER, AND D. S. HENN

A.R.A.P. Group, California Research and Technology Division, Princeton, New Jersey

W. S. LEWELLEN

Department of Physics and Atmospheric Science, Drexel University, Philadelphia, Pennsylvania

(Manuscript received 11 February 1992, in final form 14 October 1992)

ABSTRACT

A long-range transport model based on turbulence closure concepts is described. The model extends the description of planetary boundary layer turbulent diffusion to the larger scales and uses statistical wind information to predict contaminant dispersion. The model also contains a prediction of the statistical fluctuations in the tracer concentration resulting from the unresolved velocity fluctuations. The dispersion calculation is made by means of a Lagrangian puff representation, allowing the use of time-dependent three-dimensional flow fields. Predictions of the ANATEX (Across North America Tracer Experiment) releases are compared with observations. Both 24-h average surface and short-term aircraft sampler concentrations are calculated using the high-resolution wind fields from the NMC Nested Grid Model. The statistical prediction is also tested using long-term average wind data.

Statistical uncertainty in the predictions, due to the unresolved wind fluctuations, is found to be small for the 24-h average surface concentrations obtained with the high-resolution winds but is very significant for the short-term aircraft sampler concentrations. A clipped normal probability distribution provides a reasonably good description of the overall cumulative distribution of the aircraft sampler concentrations. A reasonably good description of the 24-h surface concentrations is also obtained using only the long-term average wind statistics and a lognormal probability distribution for the concentration values.

1. Introduction

The atmospheric transport of pollutants over continental scales is an important environmental process and has received considerable attention from modelers and experimentalists. With national policy on issues such as acid rain being influenced by the predictions of long-range transport models, there is a strong demand for verification of these models. As with other dispersion model evaluation studies at smaller scales, the comparison between field observations and model predictions is far from straightforward. The inability to determine the state of the atmosphere leaves a large component of uncertainty in the prediction. It is generally very difficult to distinguish model error from meteorological input uncertainty, and consequently, it is impossible to reliably assess model accuracy. Various statistical measures have been recommended for model evaluation (Fox 1981), but there are no standard methods designed to address the uncertainty in a quantitative way. As Venkatram (1982) points out, the statistical ensemble represented by any model is

defined in terms of the model input data, which makes comparison between different models difficult if they use different input.

Recognizing the stochastic nature of atmospheric dispersion, we have previously proposed that a quantitative prediction of the uncertainty be included, allowing statistical significance to be assessed (Lewellen and Sykes 1989). The uncertainty is inherent in the sense that the atmosphere can never be completely described, and effort should be expended to deal directly with the random component rather than toward eliminating it. We have therefore developed models for atmospheric dispersion, based on second-order turbulence closure, that include a prediction of the concentration fluctuation variance and thus provide a means of testing consistency between observations and predictions. These models were designed to predict plume dispersion out to ranges of about 50 km and were extensively compared with the Electric Power Research Institute (EPRI) plume model validation experiments (Lewellen et al. 1988).

The major advantage of the use of turbulence closure in the dispersion prediction is the ability to relate the evolution of the scalar concentration field to measurable velocity statistics. This approach has been initiated by Gifford (1988) for long-range transport predictions using a random walk model and is presented here using

Corresponding author address: Dr. R. Ian Sykes, A.R.A.P. Group, California Research and Technology, 50 Washington Road, P.O. Box 2229, Princeton, NJ 08543-2229.

the second-order closure framework. The dispersion calculation is extended to include a prediction of the statistical fluctuation about the mean value. This provides a method of accounting for the effects of averaging time on the observed concentration as a function of the turbulent wind input. In this context, turbulence denotes the unresolved component of the wind field and therefore depends strongly on the wind data used in the model prediction. The statistical framework forces explicit consideration of the effects of averaging time and eddy scales, in contrast to the implicit assumptions inherent in the choice of diffusion parameters.

In this paper, we describe the adaptation of our Gaussian puff model to the long-range dispersion problem and compare the model results with the tracer observations from the Across North America Tracer Experiment (ANATEX) study (Draxler et al. 1991). ANATEX was conducted in 1987 under the auspices of the National Oceanic and Atmospheric Administration (NOAA) and provides a high quality, extensive database for dispersion over thousands of kilometers. The database is large enough for statistical comparisons to be significant and appears to be the most complete study to date.

The next section briefly describes the ANATEX data employed in our model evaluation study. Section 3 details the puff model as extended to the continental-scale problem and discusses the model comparison statistics. Section 4 contains the results. Concluding remarks are contained in section 5.

2. ANATEX data

a. ANATEX experiment

The ANATEX experiment is fully described in a series of reports (Draxler and Heffter 1989; Stundler and Draxler 1989; Heffter and Draxler 1989) and summarized by Draxler et al. (1991), so only the most important features will be outlined here. The experiment was designed to provide a database for long-range transport models and used an inert tracer detectable at very low concentrations to track the dispersion across the continental United States. Small releases of perfluorocarbon tracers were made from Glasgow, Montana, and from St. Cloud, Minnesota, and measured on a network of ground samplers extending eastward from the sources to the Atlantic coast and southward to the Gulf of Mexico. The release locations and surface sampler network are shown in Fig. 1.

Three tracers were employed, with detection limits below $1 \text{ fl l}^{-1} = 10^{-15} \text{ l l}^{-1}$. The experiment lasted 3 months, from 5 January through 30 March 1987, with releases made for 3 h every 2.5 days from the two source locations. Alternate releases were made in daytime and nocturnal conditions. Perfluoro-orthodimethylcyclo-

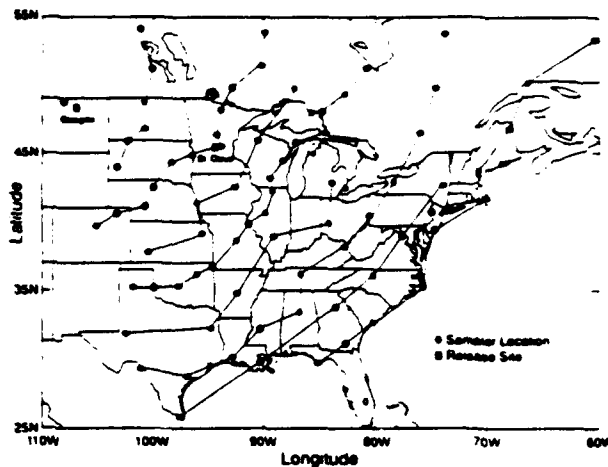


FIG. 1. ANATEX primary ground level sampling network.

hexane (oPDCH) and Perfluoromethylcyclohexane (PMCH) were released from St. Cloud, with PMCH being released every 5 days only under daytime conditions to provide some measure of independence. Perfluorotrimethylcyclohexane (PTCH) was released only from Glasgow. There was some small contamination of the oPDCH release by PMCH, but this seems to be adequately accounted for in the release data. The tracer technology is extensively described by Draxler and Heffter (1989), and the reader is referred to the ANATEX reports for further details.

b. Ground samplers

The ground sampler network, illustrated in Fig. 1, shows a total of 77 collection sites. Each sampler collected data for 24-h periods, which were then analyzed in the laboratory to obtain the average concentrations of all three tracers over the period. Samples were analyzed in two independent laboratories to provide estimates of reliability, and several collocated samples were also taken to determine repeatability. Estimates of the background concentrations of the three tracers were made from the distribution of analyzed concentrations, and all sampler concentrations are reported as excess over the background levels. There is some uncertainty in the estimate, and excess values close to the background value are not reliable. The background values for all three tracers are shown in Table 1.

In general, the sampler data analysis provided reliable concentrations from a very large fraction of the total data collected. Roughly 84% of the total possible number of measurements were archived as reliable data, giving 5400 concentrations for each of the three tracers. This is a remarkably high return, and the quantity and quality of the data make significant statistical comparison possible using this dataset.

TABLE 1. Ambient tracer background concentrations.

PTCH	PMCH	oPDCH
0.4	3.5	0.4

c. Aircraft data

In addition to the surface sampler network, three aircraft made direct sampling flights through the plumes at ranges out to about 450 km from the source. The aircraft attempted to fly transverse paths through the plume at different altitudes, using observed and forecast wind fields to estimate the plume location. The flights were reasonably successful, with roughly 40% of the observations producing nonzero concentrations, indicating the presence of a plume. Flights were made at altitudes up to about 2500 m, with data being sampled over 6-min periods (12 min in some cases). Using a typical airspeed of about 55 m s^{-1} , the effective path-length was about 20 km (or 40 km).

In total, the aircraft provided about 1300 sampler measurements from a total of 50 flights from Glasgow, and 22 flights from St. Cloud. The short time-average path integrals are an interesting complement to the fixed 24-h averages from the ground samplers. Unfortunately, the limited range of the aircraft data prevents much direct comparison between the two. The aircraft data does present a serious challenge for model prediction, however, and the predictability of these near-instantaneous samples will be examined below.

3. Model description

a. Puff dispersion model

SCIPUFF (for second-order closure integrated puff) was originally developed as a short-range dispersion model and tested against the EPRI plume model development and validation experiments at the Kincaid, Illinois, and Bull Run, Tennessee, power plants (Sykes et al. 1988). The model was derived from simplifications of the full second-order turbulence closure equations using a Gaussian puff framework. The Lagrangian puff methodology allows a general computation of time-dependent effects and spatial inhomogeneity. The model has been modified considerably to allow application to long-range transport problems, and the full equations for a passive tracer are presented here. SCIPUFF represents the scalar concentration distribution as a collection of overlapping Gaussian puffs; that is,

$$c(\mathbf{x}, t) = \sum_{\alpha} c_{\alpha}(\mathbf{x}, t). \quad (1)$$

where, using standard Cartesian tensor notation and the summation convention,

$$c_{\alpha} = \frac{Q_{\alpha}}{(2\pi)^{3/2} \|\sigma_{\alpha}\|^{1/2}} \times \exp\left[-\frac{1}{2} \sigma_{\alpha}^{-1}(x_i - \bar{x}_{i\alpha})(x_j - \bar{x}_{j\alpha})\right]. \quad (2)$$

Here Q_{α} is the mass associated with puff α , $\bar{x}_{i\alpha}$ is the puff centroid, σ_{α} is the second-moment tensor, and $\|\sigma_{\alpha}\|$ is the determinant of σ_{α} . The formal definition of the moments is

$$Q_{\alpha} = \int_V c_{\alpha} dV. \quad (3)$$

$$Q_{\alpha} \bar{x}_{i\alpha} = \int_V c_{\alpha} x_i dV. \quad (4)$$

$$Q_{\alpha} \sigma_{ij\alpha} = \int_V c_{\alpha} (x_i - \bar{x}_{i\alpha})(x_j - \bar{x}_{j\alpha}) dV. \quad (5)$$

This is a generalization of the standard puff representation, which assumes that σ is diagonal (e.g., Bass 1980; Sykes et al. 1988).

The model is advanced in time by solving ordinary differential equations for the puff moments (3)–(5). The derivation of these equations follows the plume analysis of Sykes et al. (1986) and will be described only briefly.

Conservation of scalar mass implies

$$\frac{dQ_{\alpha}}{dt} = 0. \quad (6)$$

Consideration of the moment equations yields

$$\frac{d\bar{x}_{i\alpha}}{dt} = \bar{u}_i(\bar{x}_{\alpha}, t) \quad (7)$$

and

$$\frac{d\sigma_{ij\alpha}}{dt} = F_{ij\alpha} + \sigma_{ik\alpha} \frac{\partial \bar{u}_j}{\partial x_k} + \sigma_{jka} \frac{\partial \bar{u}_i}{\partial x_k}. \quad (8)$$

where \bar{u}_i is the ambient mean wind velocity, and

$$Q_{\alpha} F_{ij\alpha} = \int [(x_i - \bar{x}_{i\alpha}) \overline{u'_j c'_{\alpha}} + (x_j - \bar{x}_{j\alpha}) \overline{u'_i c'_{\alpha}}] dV. \quad (9)$$

Here $\overline{u'_i c'_{\alpha}}$ represents the turbulent flux of the scalar associated with puff α ; standard Reynolds-averaging notation is used, with the overbar representing the mean value and prime denoting fluctuation from the mean. Thus, (7) represents translation of the centroid by the mean wind, while (8) describes spreading of the puff by turbulent diffusion and distortion by wind shear.

The evolution of the turbulent diffusion terms is obtained from the second-order closure result of Sykes et

al. (1986) but uses a simplified treatment of the large-scale turbulence, yielding

$$\frac{dF_{11\sigma}}{dt} = 2\overline{u'^2} - A \frac{q_H}{\Lambda_H} F_{11\sigma} \quad (10)$$

$$\frac{dF_{22\sigma}}{dt} = 2\overline{v'^2} - A \frac{q_H}{\Lambda_H} F_{22\sigma} \quad (11)$$

$$\frac{dF_{33\sigma}}{dt} = 2\overline{w'^2} + \frac{g}{T_0} G_\sigma - A \frac{q_v}{\Lambda_v} F_{33\sigma} \quad (12)$$

and

$$\frac{dG_\sigma}{dt} = 2\overline{w'\theta'} - F_{33\sigma} \frac{\partial \bar{\theta}}{\partial z} - A \frac{q_s}{\Lambda_v} G_\sigma \quad (13)$$

where

$$Q_\sigma G_\sigma = 2 \int_V (x_3 - \bar{x}_{3\sigma}) \overline{c'_\sigma \theta'} dV. \quad (14)$$

Here $\overline{u'^2}$, $\overline{v'^2}$, $\overline{w'^2}$ are the ambient velocity variances, $q_H^2 = \overline{u'^2} + \overline{v'^2}$, and Λ_H is the horizontal length scale of the velocity fluctuations. The parameter Λ_v is a vertical fluctuation scale, and $q_v^2 = 3\overline{w'^2}$ is a measure of the energy associated with the vertical motions. The gravitational acceleration is g , T_0 is a reference temperature for the Boussinesq approximation, and θ is the ambient potential temperature. The ambient vertical heat flux is $\overline{w'\theta'}$, and G_σ represents the effects of buoyancy on the vertical diffusivity. The empirical turbulence closure constant, A , takes the value 0.75 (Lewellen 1977). We assume that $F_{ij\sigma} = 0$ for $i \neq j$, although the effects of velocity cross correlations could be included if required. We do not expect significant effects from such correlations in dispersion on the scales of interest here. The specification of the ambient wind, temperature, and turbulence information will be presented in the next section.

To account for the inversion-capped mixing, the vertical diffusivity $F_{33\sigma}$ is set equal to zero for puffs within the mixed layer with $\sigma_z > 0.8z_i$, where $\sigma_z = \sqrt{\sigma_{33}}$ and z_i is the mixed-layer depth. This simply turns off any further vertical diffusion when the puff is mixed across the entire boundary layer.

A valuable feature of the second-order closure model for the turbulent diffusion is the quantitative link that it provides with measurable turbulence correlations. The velocity variances are not necessarily easily measured, but they can be estimated at various length scales to give a direct prediction of scalar diffusion.

Having presented the model equations for scalar transport and diffusion, it remains to define the scalar source. Details of the source specifications are given in appendix A, but a brief overview is given here. Since the dispersion calculation time step is 15 min and the source diameter is small (less than a meter), the spatial evolution of the source plume must be considered before initializing an appropriate puff. Essentially, a

simplified one-dimensional (or plume) version of SCI-PUFF is used to calculate mass, centroid, and second moments using a number of small time steps for a total time t . This scheme also allows us to compute the rapid evolution of the fluctuation variance c'^2 .

Equation (8) shows that puff size, shape, and orientation change through the action of turbulent diffusion and shearing motion due to nonuniformities in the wind field. These tend to increase the puff size: diffusion increases the diagonal moments and hence increases the puff volume, while the velocity shear terms preserve volume but cause elongation in the direction of the wind shear (and contraction normal to that). At some point, then, the puff size will grow too large for the local specification of the wind field to be accurate over the entire puff. This was not a factor in the limited-range modeling of Sykes et al. (1988) but will be important in long-range transport. Therefore, a puff-splitting algorithm based on the diagonal components of the moment tensor σ has been implemented.

When the moment in a particular coordinate direction exceeds the critical size specified for that direction, the puff is split into two smaller, overlapping puffs. The critical size is related to the scale of the specified mean velocity variation in each direction, typically the grid length for wind fields from a numerical model output. The splitting algorithm conserves all the moments of the distribution, eliminating artificial diffusion, and there is sufficient overlap of the newly created pair of puffs to prevent significant change in local concentrations.

Puffs are split in the vertical direction as well as in the horizontal, and special care must be used near the surface and near the inversion. The algorithm used in SCIPUFF reflects puffs at the surface and also at the inversion for any puff splitting from within the mixed layer. This essentially treats the inversion as a rigid boundary, except that the inversion moves vertically and the reflection condition is applied only locally to determine the location of the newly created split puff. A puff will cross the inversion if the inversion falls below its current location, leaving it in the low-turbulence region above the mixed layer.

In addition to the splitting algorithm, SCIPUFF also incorporates a merging routine for puffs that sufficiently overlap. Merging is required to track diffusion from a small source where a plume of small puffs is released. In this case, the puffs will eventually grow and overlap one another so that the plume can be adequately represented by a smaller number of puffs. The merging algorithm maintains an efficient calculation of the subgrid concentration field and also prevents the splitting algorithm from generating puffs in exponentially growing numbers. When new puffs are created in regions that already contain similar puffs, they will be merged with the existing puffs. The merging procedure,

like the splitting algorithm, maintains all the moments of the puff distributions.

b. Concentration fluctuation variance

One of the most important aspects of our modeling of scalar dispersion has been the derivation of model equations for the concentration fluctuation variance $\overline{c'^2}$. The turbulent dispersion of a scalar is inherently random and a quantitative measure of the uncertainty in any observable concentration is almost essential for any meaningful interpretation of model predictions of atmospheric observations. The plume models described by Sykes et al. (1984, 1986) contain a variance prediction that has been adapted to the context of long-range transport.

The variance prediction is obtained from the conservation equation for mean-square concentration. It is easily shown that $\overline{c'^2}$ is advected, diffused, and dissipated only by molecular diffusivity. We assume that the advection and turbulent diffusion of $\overline{c'^2}$ is similar to that of the mean concentration, and represent the c'^2 field as a sum of Gaussians with the same shape as the mean. Thus, an additional puff quantity, S_α , is associated with each puff, where

$$S_\alpha = \int_V \overline{c_\alpha'^2} dV. \tag{15}$$

The evolution of S_α is given by

$$\frac{dS_\alpha}{dt} = -\epsilon_\alpha, \tag{16}$$

where ϵ_α represents the volume-integrated dissipation associated with puff α .

Models for fluctuation dissipation are generally written in the form, c'^2/τ_c , that is, the fluctuation variance divided by a dissipation time scale. The first task in the specification of ϵ_α is therefore a derivation of the variance from S_α . By definition, $\overline{c'^2} = \overline{c^2} - \overline{c}^2$. The variance can be obtained from this relation, but the calculation of $\overline{c^2}$ involves an interaction between overlapping puffs. Since $\overline{c} = \sum_\alpha \overline{c}_\alpha$, we have

$$\overline{c^2} = \sum_{\alpha, \beta} \overline{c}_\alpha \overline{c}_\beta. \tag{17}$$

We define $V_\alpha = \int_V \overline{c_\alpha'^2} dV$, as the integrated variance associated with puff α , and approximate

$$V_\alpha = S_\alpha - \sum_\beta Q_\alpha Q_\beta I_{\alpha\beta}, \tag{18}$$

where $I_{\alpha\beta}$ is the overlap integral between puff α and puff β ; that is,

$$I_{\alpha\beta} = \int g_\alpha(x) g_\beta(x) dV. \tag{19}$$

and $g_\alpha = c_\alpha/Q_\alpha$ from (2).

The representation of the overlap integral in (18) relies on the assumption that the integrated $\overline{c'^2}$ associated with puff α can be written

$$\int_V \overline{c_\alpha'^2} dV = \sum_\beta \int_V \overline{c_\alpha c_\beta} dV.$$

This is a natural partition of the total $\overline{c'^2}$ between the puffs but is somewhat arbitrary, and perhaps other partitions could be imagined.

Having defined V_α , all that remains is the specification of the dissipation time scale, τ_c . As in our earlier modeling, τ_c is obtained from a predicted length scale of the fluctuations. In the long-range transport problems, however, the difference in character between horizontal and vertical motions must be dealt with.

The horizontal fluctuation scale is modeled in a similar way to the plume analysis of Sykes et al. (1986). Thus,

$$\frac{d}{dt} l_H = \begin{cases} 0.25q_i, & l_H \leq \Lambda_H \\ 0.1q_i, & l_H > \Lambda_H. \end{cases} \tag{20}$$

where

$$q_i^2 = (\overline{u'^2} + \overline{v'^2}) \min \left[\left(\frac{l_H}{\Lambda_H} \right)^{2/3}, 1 \right] + \overline{w'^2} \min \left[\left(\frac{l_H}{\Lambda_v} \right)^{2/3}, 1 \right]. \tag{21}$$

This represents an inertial range scaling of the velocity variances, with the vertical component included to account for the increased energy in convective conditions.

We then model

$$\tau_{c,H}^{-1} = 2bs \frac{q_i}{l_H}, \tag{22}$$

where $b = 0.125$ and $s = 1.8$ are closure model constants (Lewellen 1977).

The total dissipation must also account for vertical motions since the diffusion through the depth of the convective layer will involve significant dissipation of concentration fluctuations. In the context of long-range transport, it is assumed that this is a rapid process: that is, the pollutant quickly becomes well-mixed through the boundary layer and does not produce fluctuations. Generally, the time scales associated with vertical motions are expected to be rapid, although they will not remove the large-scale horizontal fluctuations. Therefore, a dissipation term has been included to reduce the total S_α by the appropriate amount to match the reduction of the mean concentration by vertical diffusion. The appropriate dissipation rates are

$$\tau_\alpha^{-1} = \frac{F_{33}}{2l_v^2} \tag{23}$$

and

$$\frac{dl_v^2}{dt} = 2F_{33}. \quad (24)$$

The full model for S_a is therefore

$$\frac{dS_a}{dt} = -\frac{V_a}{\tau_c},$$

where $\tau_c^{-1} = \tau_{ch}^{-1} + \tau_{cv}^{-1}$. The vertical puff scale is represented by l_v , which is not the same as σ_z . The individual puff spread depends on the splitting algorithm, which will reduce σ_z to maintain numerical resolution.

c. Meteorology

The meteorological inputs necessary for the dispersion calculation are the mean wind field and the turbulent velocity correlations. SCIPUFF does not contain any meteorological data-interpolation modules, so the meteorology must be specified. Fortunately, the National Meteorological Center's Nested Grid Model (NGM) output was archived every 2 h throughout the ANATEX experiment and is available on tape from the NOAA Air Resources Laboratory. This high-resolution weather prediction model was run in 12-h forecast mode for the period, giving short-range forecasts on a horizontal grid of roughly 90 km. For use in SCIPUFF, the fields were interpolated onto a three-dimensional grid with 1° horizontal (latitude, longitude) resolution and nonuniform vertical resolution as indicated in Table 2.

The boundary-layer turbulence was deduced from the NGM predictions of surface stress, u_*^2 , where u_* is the surface friction velocity, heat flux, H_0 , and mixing layer depth, z_i , as described below. Single mixed-layer values of the turbulence intensity and length scale for a given latitude and longitude were used because the puff-splitting algorithm tends to produce a nonuniform concentration profile if the mixed-layer contains several vertical grid lengths and the diffusivity varies across

the layer. Under our assumption of rapid mixing for long-range transport, the detailed evolution of the mixed-layer profile is not important. Difficulties are avoided with the splitting procedure by specifying constant values that are representative of the entire layer. Thus,

$$\overline{w'^2} = \begin{cases} 0.7u_*^2 + 0.4w_*^2, & z \leq z_i \\ 10^{-2} \text{ m}^2 \text{ s}^{-2}, & z > z_i, \end{cases}$$

$$\overline{u'^2} = \begin{cases} \max(2u_*^2 + 0.4w_*^2, \overline{u'^2}), & z \leq z_i \\ \overline{u'^2}, & z > z_i, \end{cases}$$

$$\lambda_v = \begin{cases} 0.25z_i, & z \leq z_i \\ 10 \text{ m} & z > z_i, \end{cases}$$

where $w_* = [(g/T_0)H_0z_i]^{1/3}$ is the convective velocity scale and the free atmosphere horizontal velocity variance $\overline{u'^2}$ is discussed in the next section. Here H_0 is assumed positive in the definition of w_* . If H_0 is negative, w_* is set to zero. The free atmosphere values for the vertical velocity variance and scale are somewhat arbitrary, although they are related by the definition of a unit turbulent Froude number; that is, $w_*^2/N^2\Lambda_v^2 = 1$, where N is the Brunt-Väisälä frequency, taken to be 10^{-2} s^{-1} . The horizontal turbulence scale in the boundary layer is taken to be the same as in the free atmosphere, as discussed below.

Wind profiles were obtained directly from the NGM fields with no boundary-layer correction imposed. The scheme suggested by Draxler (1990) implies a linear velocity profile below the first NGM grid point (roughly 150 m) under stable conditions. This was found to predict unrealistically low translation speeds for the low-level releases in ANATEX, where extensive stable conditions were predicted. Much better predictions were obtained with no correction and by simply using the lowest NGM grid-level velocity at all points between that level and the surface. Based on the model results described later, we suggest that the NGM boundary layers may be biased toward shallow stable layers, especially in January and February, where extensive areas of stable conditions were predicted for continuous periods of many days. Some calculations were therefore run with a "standard" boundary layer, which was uniformly imposed over the entire domain and exhibited the diurnal variation illustrated in Fig. 2. The height variations and surface heat flux were specified as shown, and the local time used for the variation was CST over the entire domain. The numerical values used in the runs were $h_{\max} = 1000 \text{ m}$ for the January-February period, and $h_{\max} = 1500 \text{ m}$ for March, and $h_{\min} = 50 \text{ m}$ for both periods. The surface heat flux associated with this boundary layer is zero during the night and a cosine variation during the day, with a maximum value of $0.05^\circ\text{C m s}^{-1}$. This is clearly a very approximate representation and cannot represent any particular day,

TABLE 2. Vertical grid used for SCIPUFF meteorology (m).

Level	Height
1	0.0
2	150.0
3	300.0
4	485.7
5	715.5
6	999.6
7	1350.4
8	1783.2
9	2316.9
10	2974.2
11	3783.2
12	4777.9
13	6000.0
14	7500.0

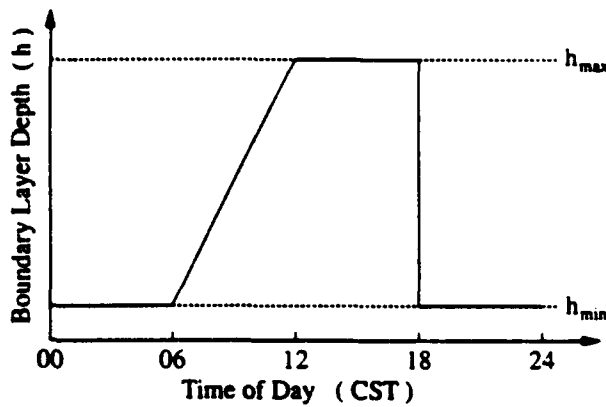


FIG. 2. Standard boundary-layer diurnal variation.

but it provides a reasonable average diurnal variation of the boundary layer.

d. Horizontal wind fluctuations

The specification of dispersion in terms of velocity fluctuation statistics avoids the use of completely empirical diffusivities but requires that these statistics be provided as part of the meteorological description. This can be viewed as a more complete specification of the flow conditions, defining the unresolved or random component of the velocity in addition to the mean wind. Two recent pieces of research have allowed us to characterize this component of the large-scale flow in a nonarbitrary way, although not with the level of understanding that we have for small-scale, three-dimensional turbulence in the planetary boundary layer. First, Nastrom and Gage (1985) analyzed the GASP (Global Atmospheric Sampling Program) wind data, collected by specially instrumented commercial aircraft over a long period. This work delineated the spectral behavior of the wind fluctuations in the upper troposphere and lower stratosphere as a function of latitude and season. The data shows a clear spectral break at a horizontal wavelength of about 400 km, with a k^{-3} spectrum at longer wavelengths and $k^{-5/3}$ for shorter scales. Second, Gifford (1988) proposed a theoretical model to describe the spectrum, arguing that the large-scale behavior is consistent with the predictions of two-dimensional turbulence theory, while the $k^{-5/3}$ behavior indicates three-dimensional motions in that part of the spectrum. Gifford's analysis assumes an integral time scale of f^{-1} for the three-dimensional turbulence, where f is the Coriolis parameter, using dispersion measurements as supporting evidence (Gifford 1985). A corresponding turbulence length scale is easily derived from the time and velocity scales.

We assume that the upper-troposphere data is representative of the entire lower atmosphere, although there is probably some vertical variation in practice. At present, the data do not exist to define the fluctu-

ation profiles, and the simplest assumption is made. Furthermore, the GASP data represent long-term averages and cannot provide any relationship between the local meteorological conditions and the local smaller-scale velocity fluctuations. Use of the GASP data is therefore equivalent to a climatologically averaged spectrum. Using Gifford's suggestions and the GASP profiles, which show an increase in fluctuation variance toward the poles, the horizontal velocity variance is represented as

$$\overline{u'^2} = \overline{v'^2} = \begin{cases} V_0^2 / (2 \cos \theta), & \theta < 75^\circ \\ V_0^2 / (2 \cos 75^\circ), & \theta \geq 75^\circ, \end{cases}$$

where θ is the latitude and $V_0^2 = 5.5 \text{ m}^2 \text{ s}^{-2}$. The value of V_0^2 is suggested by Gifford (1988) using an energy dissipation estimate, but the inverse cosine variation is an empirical factor to provide a match with the latitudinal variation observed in the GASP data. The turbulence length scale associated with these dissipative fluctuations is taken to be $\Lambda_T = (u'^2 + v'^2)^{1/2} / f$. The singularity in f at the equator is not a problem in the current applications since the southern boundary of the domain is 20°N .

The velocity variance used in the dispersion calculation depends on the resolution of the input wind fields since the turbulence input represents only the unresolved component of the wind. Using the filter scale, Λ_G , which is related to the wind-field resolution, we define

$$\Lambda_H = \min(\Lambda_G, \Lambda_T)$$

and

$$\overline{u'^2} = \overline{u'^2} \left(\frac{\Lambda_H}{\Lambda_T} \right)^{2/3},$$

consistent with a $k^{-5/3}$ spectral behavior. For the winds used in this study, we postulate $\Lambda_G > \Lambda_T$ since $\Lambda_T \approx 30 \text{ km}$ and the numerical grid length is about 100 km . The model calculations will therefore use the full spectral energy, $\overline{u'^2}$.

This essentially specifies all the horizontal turbulence statistics required for a dispersion prediction, and the results of the calculations using these statistics will be presented in section 4.

e. Model performance measures

It is well known that trajectory errors are one of the major causes of poor correlation between model predictions and observations. An error in plume location will result in a negative correlation, that is, zero prediction for samplers impacted by the plume and high concentrations predicted where nothing is observed. The errors in trajectory prediction are largely due to wind field errors, although some discrepancy can result from incorrect prediction of the vertical distribution

of pollutants. The errors in the NGM trajectory predictions are discussed by Draxler (1991) and in the model comparison study of Clark and Cohn (1990) and will not be presented here. Suffice it to say that the NGM errors lie within the range of the other trajectory methods reported by Clark and Cohn.

We will concentrate on the statistical distribution of the concentration observations, uncorrelated in time and space. Some localization will be introduced by consideration of two separate time periods of observations and also by partition by distance from the source. Clearly, as the sampled set is made more specific, the number of observations are reduced and the statistical comparison becomes less significant. The relatively large sample size for the surface observations allows a reasonable partition to be made, and cumulative concentration distributions will be presented for a selection of samples. Similar comparison will be made for the aircraft data.

4. Results

a. Ground samplers

The three-month ANATEX study is divided into two parts by a missing week of NGM wind fields, from 23 February to 1 March. This gives a seven-week continuous period from 5 January to 21 February, and a four-week period in March. Since the model needs to

be reinitialized in March, several days are allowed for the tracers to become established on the sampler network and comparisons in the second period are restricted to cover 9 March to 28 March. This is not the same division as used by Clark and Cohn (1990), who considered two six-week periods, but is the most convenient means of treating the missing wind data.

Typical maps of the predicted instantaneous concentrations at two altitudes are shown in Figs. 3 and 4. These maps, which show tracer patterns from many releases of PTCH from Glasgow and oPDCH from St. Cloud, illustrate the different characteristics of the two periods. The January–February winds are generally northwesterly with a very shallow mixed layer, resulting in very little tracer being found at 1 km in Fig. 3. The vertical wind shear is also evident in Fig. 3, with the tracer at 1 km displaced to the east of the surface-level tracer. Figure 4 shows a typical March distribution, with very light winds and dispersion over the entire domain. The deeper mixing is also evident with almost uniform concentrations up to 1 km.

The surface sampler network records 24-h average concentration, and the time-dependent SCIPUFF prediction must be averaged over the appropriate period for comparison with the observations. A typical time history for a sampler in the center of the network is shown in Fig. 5, along with the 24-h average and the observed concentrations. The individual releases are often evident in these traces, although the time of pas-

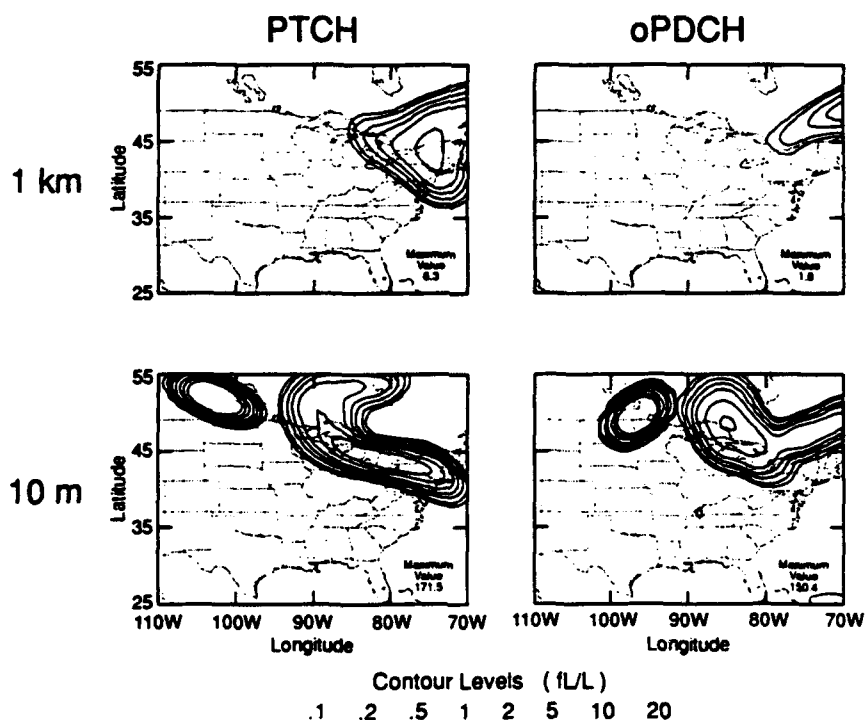


FIG. 3. SCIPUFF instantaneous PTCH and oPDCH surface concentration patterns at two altitudes for 1800 UTC 29 January.

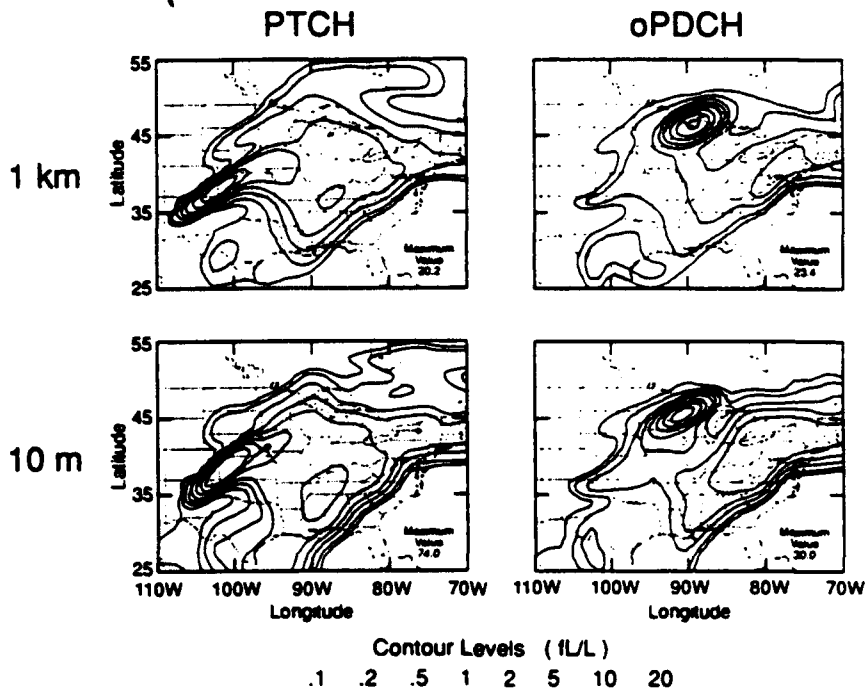


FIG. 4. SCIPUFF instantaneous PTCH and oPDCH surface concentration patterns at two altitudes for 0600 UTC 28 March.

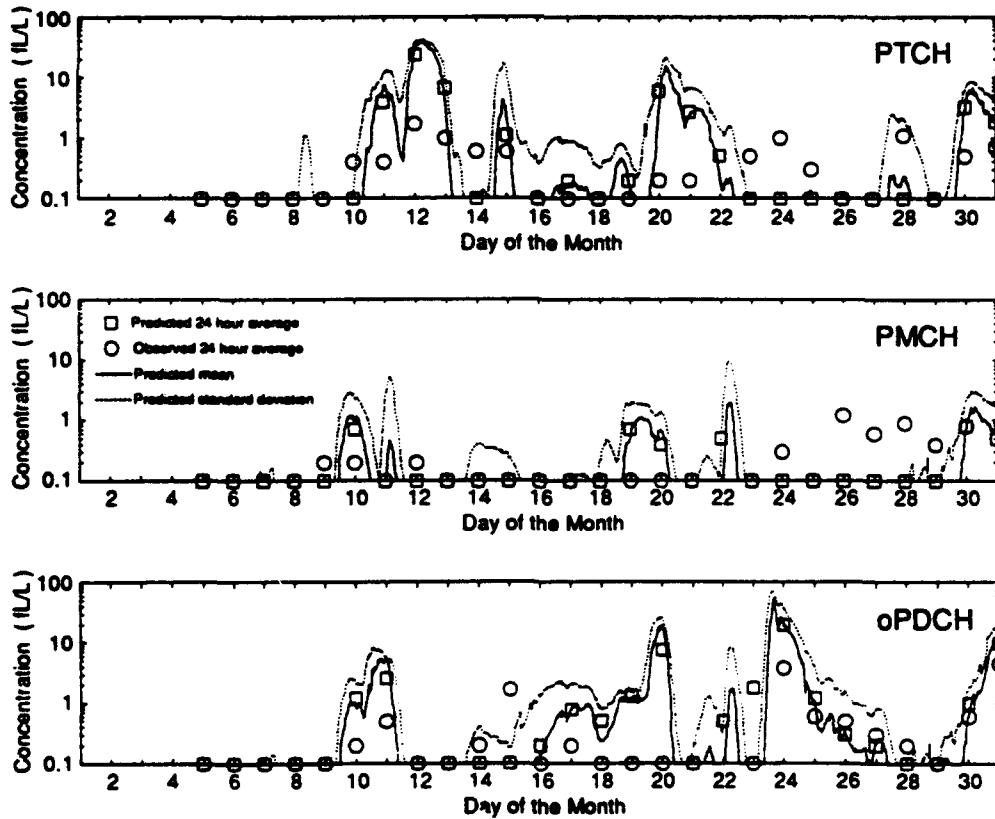


FIG. 5. Tracer history for sampler 2005 located at Dayton, Ohio (39.87°N, 84.12°W), for the month of January. (□ predicted 24-h average; ○ observed 24-h average; predicted: mean —, standard deviation - - - -).

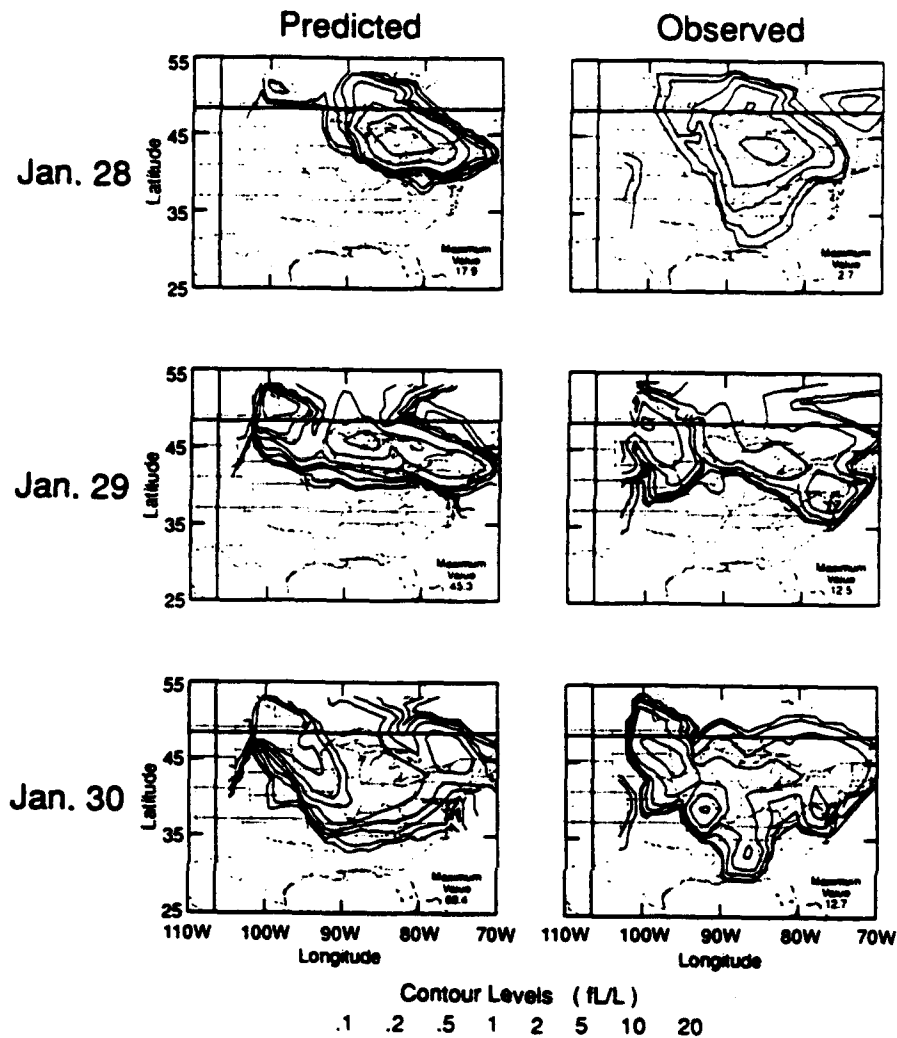


FIG. 6a. Comparison of the SCIPUFF 24-h average PTCH surface concentration patterns with the observed patterns for the period 28-30 January.

sage varies considerably, and it is sometimes difficult to distinguish between releases. There are periods of good correlation between observed and predicted concentration, but in general there is a poor prediction of the actual value on a day-by-day basis. This is consistent with other model comparisons, as discussed in the Introduction, and is largely attributable to errors in flow trajectory.

In addition to trajectory errors, there is an inherent uncertainty due to unresolved turbulence. SCIPUFF contains a prediction of the turbulence-induced uncertainty, but the effect of 24-h time averaging (discussed in appendix B) reduces the fluctuation intensity to near-negligible proportions. Therefore, only mean concentration is considered in the analysis of the 24-h average data. The turbulent fluctuation component will be discussed later in connection with the short-term aircraft data.

Figure 6 shows two 3-day sequences of the 24-h average surface tracer concentrations compared with the equivalent maps from the observed values. In general, the shape and location of the predicted surface concentration patterns show good overall agreement with the observations for both periods. This is an indication of the accuracy of the prescribed wind field and, also, the lateral diffusion parameterization. The concentration magnitude is evidently overpredicted in the January period; however, the quantitative agreement is much better for the March period. This discrepancy will be discussed further in connection with the statistical analysis below.

The trajectory errors have been analyzed by Clark and Cohn (1990) for a range of wind models, including the NMC NGM winds, so no such analysis is performed here. We proceed directly to a comparison between the cumulative distributions of the sampler concentrations.

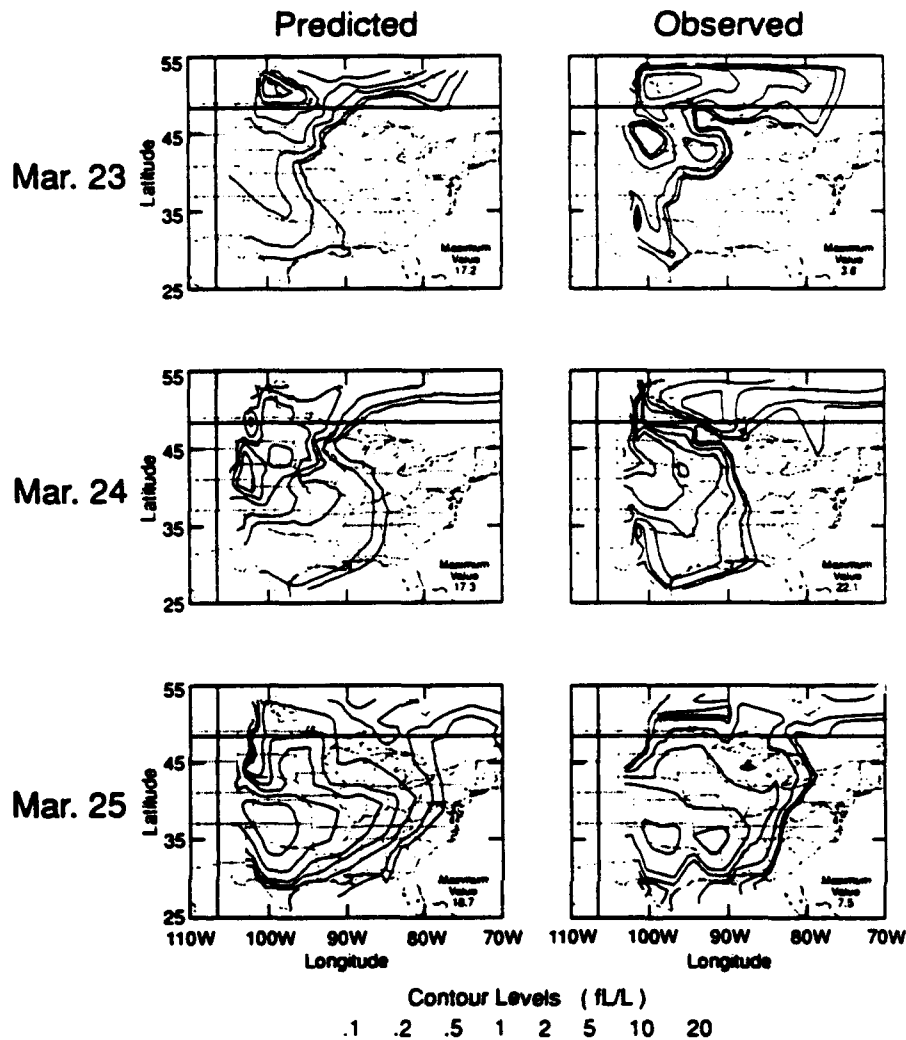


FIG. 6b. Comparison of the SCIPUFF 24-h average PTCH surface concentration patterns with the observed patterns for the period 23–25 March.

These distributions include all the samplers over the whole time period, with the exception of the three samplers closest to St. Cloud for PMCH and oPDCH and the closest sampler to Glasgow for PTCH. These samplers are within the puff-initialization region, and therefore, accurate predictions cannot be made for them. Figure 7 shows the cumulative distribution for the January–February period and indicates an overprediction by roughly a factor of 2 for all three tracers. Since the horizontal spread and location of the surface concentration patterns are generally well predicted, as illustrated in Fig. 6, the most likely cause of the overprediction is incorrect vertical diffusion of the tracer. An examination of the NGM boundary-layer prediction shows that persistent shallow, stable layers occur frequently in the January–February period over much of the domain. In contrast, the March predictions typically show deeper convective layers developing almost

every day. We, therefore, suggest that the overprediction may be due to insufficient vertical mixing using the NGM boundary-layer predictions. Figure 7 also shows the results using a standard 1000-m-deep mixed layer every day over the whole spatial domain for the January–February period. The dispersion prediction is obviously sensitive to the boundary-layer estimate since this determines the vertical dilution of the tracer: a 1000-m layer apparently gives a much better distribution. The results can be examined in more detail by subdividing the samplers into arcs depending on their distance from the sources. The distributions for PTCH on three separate arcs, shown in Fig. 8, provide evidence that the model is predicting the correct evolution of the tracer with distance.

Similar results are available for the three-week March period, although use of the NGM boundary layer gives a better prediction here, as shown in Fig. 9. The results

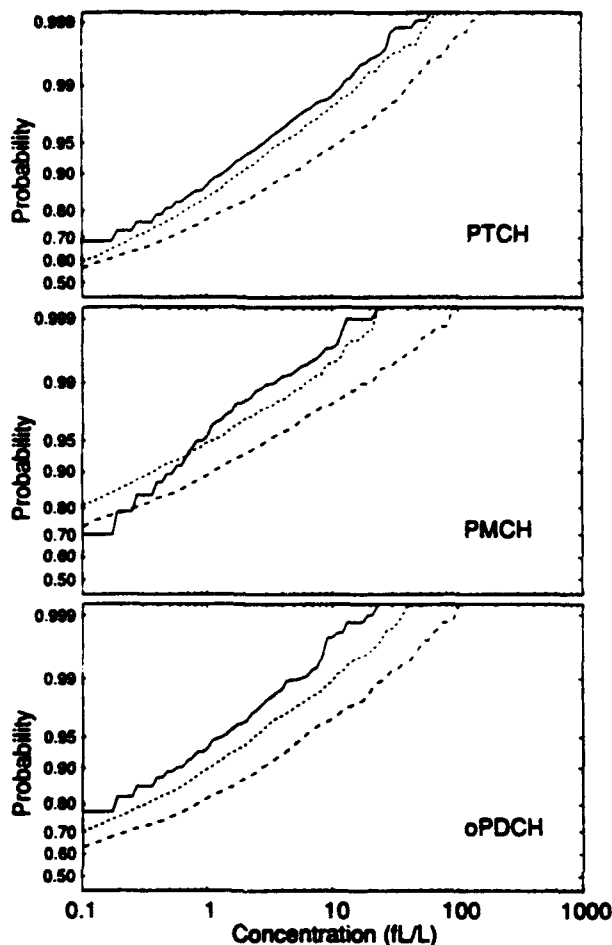


FIG. 7. Predicted and observed ground sample cumulative distribution functions for the period 5 January–21 February (— observed; - - - predicted; NGM boundary layer - - - , standard 1000-m boundary layer - - -).

for a standard 1500-m layer are also presented in Fig. 9 and show an improvement. The distributions on the arcs show a good prediction of the downwind evolution for this three-week period, but it is similar to Fig. 8 and is therefore not shown.

b. Aircraft data

The data from the aircraft samplers provide short-term spatial averages over a pathlength typically on the order of 20 km. The corresponding model predictions are computed as the average of the mean concentration at the flight path endpoints (effectively assuming a linear variation with path length). Reductions in the predicted concentration variances due to spatial averaging are estimated by a procedure, described in appendix B, based on an assumed spatial correlation function with an integral scale related to the internal fluctuation scale l_H .

Turbulent fluctuations are much more significant in these shorter-term averages than in the 24-h surface averages, and any comparison with the data requires that account of the resulting uncertainty be made. Following the philosophy of Lewellen and Sykes (1989), the aircraft data are therefore treated as realizations of a random variable theoretically defined by appropriate probability distribution functions. Our modeling assumes a form for the distribution function that can be defined using only the predicted mean and variance. As in our shorter-range results, we assume a clipped normal distribution, since it gives better agreement than the lognormal distribution suggested by Csanady (1973). The clipped normal distribution results from replacing any unrealizable negative tail of a normal distribution by a delta function at zero concentration whose strength is defined by integrating over the negative range. Details can be found in Lewellen and Sykes (1986).

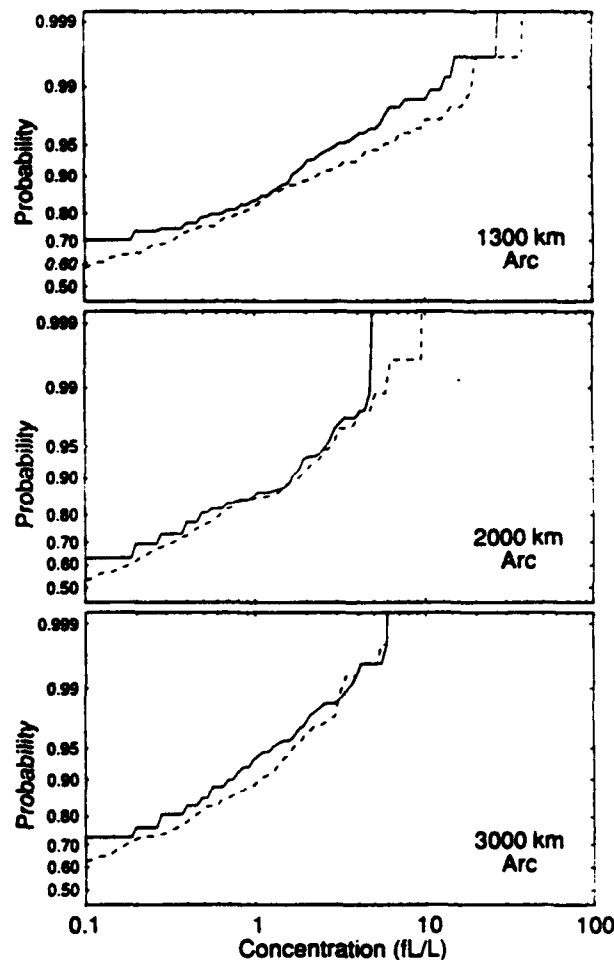


FIG. 8. Predicted and observed ground sample cumulative distribution function for PTCH along three arcs for the period 5 January–21 February. Predictions were made using a standard boundary-layer depth of 1000 m (— observed; - - - predicted).

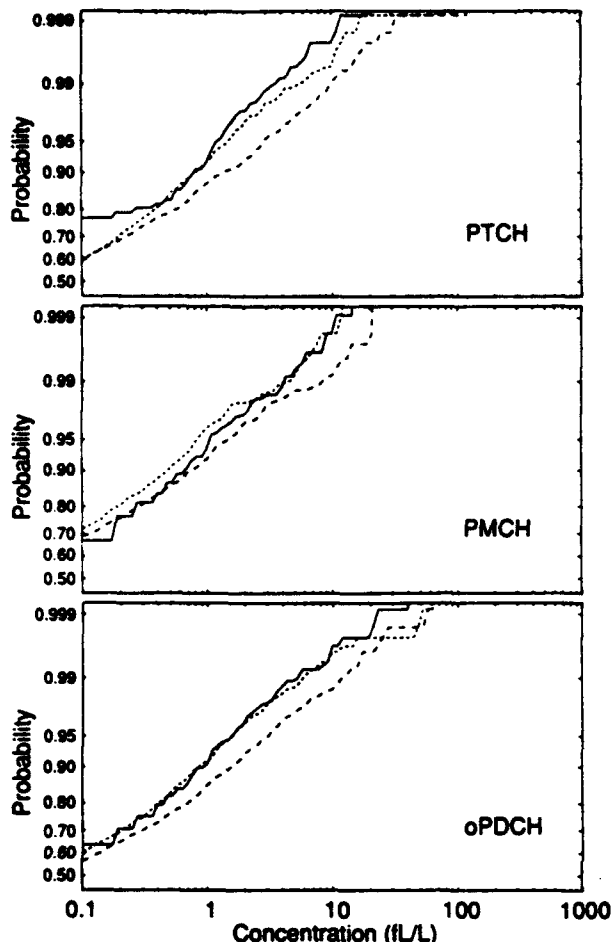


FIG. 9. Predicted and observed ground sample cumulative distribution functions for the period 9–28 March (— observed; predicted: NGM boundary layer ---, standard 1500-m boundary layer ----).

The cumulative distribution of aircraft sampler concentrations of PTCH from Glasgow is shown in Fig. 10. The data is restricted to samples further than 50 km from the source to avoid the puff-initialization region. This is a minor restriction since most of the samples were from greater distances. The figure also shows the distributions of the predicted mean concentration \bar{c} , the expected distribution with 90% confidence limits, and the observations. The expected distribution is obtained by making a large number of random samples from each of the predicted distributions. Specifically, for each aircraft sample, the model-predicted mean and variance (of the average along the flight path) are used, along with the assumed clipped-normal shape, to define a probability distribution. A set of pseudo-observations are created by taking random samples from each distribution and constructing the resulting cumulative distribution function (cdf). After taking a large number of random samples and constructing a large number

of cdf's from these pseudo-observations, the expected distribution is obtained, that is, the average cdf and confidence bounds. (The 90% confidence bounds shown in Fig. 10 indicate that 90% of the cdf's constructed from individual sets of the pseudo-observations fall between the two appropriate curves.)

The contrast between the \bar{c} distribution and the expected distribution is worth noting. Here \bar{c} is the predicted ensemble-average plume concentration, taking no account of fluctuations, and therefore tends to be spread over a larger region than that occupied by an actual plume realization (observed or "predicted"). Thus, the mean distribution contains many small values but few nonzero predictions, while the expected distribution contains a small number of large values but many zero predictions, that is, high intermittency.

Figure 10 illustrates some features that are typical of all the predicted tracer distributions. The distribution of \bar{c} contains too few small values ($<1 \text{ fl l}^{-1}$) and too few large values for the reasons just discussed, while the expected distribution has too many small values compared with the observations. The discrepancy between the observed and expected distribution is attributed to the nonrandom-sampling procedure used in the aircraft sampling. Flights were made on the basis of the most recent wind forecasts, with the objective of intersecting the tracer plume. Furthermore, on-board real-time sampling was used to locate the tracer and to determine the flight pattern during the mission to provide several transects of the plume. This procedure can be expected to produce fewer "zero" samples than a completely random sampling, and some allowance for this effect needs to be made in the comparison.

This conditional sampling of the tracer cannot be modeled easily, and we therefore arbitrarily match the observed and predicted distributions at the 1 fl l^{-1} level.

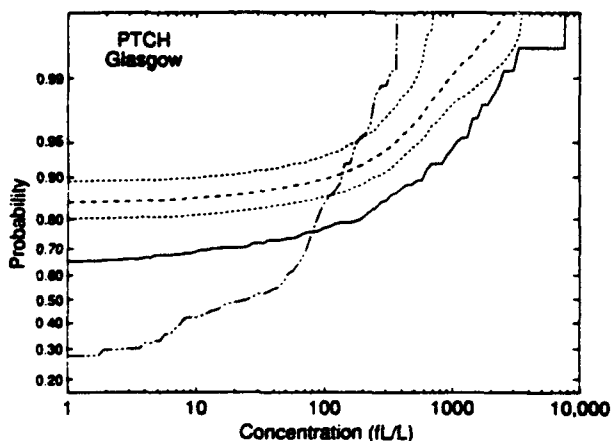


FIG. 10. Predicted and observed aircraft sample cumulative distribution functions for the period 9–28 March. Predictions were made using a standard boundary-layer depth of 1500 m (— observed; predicted: expected ---, mean - - - - -, 90% confidence limits ----).

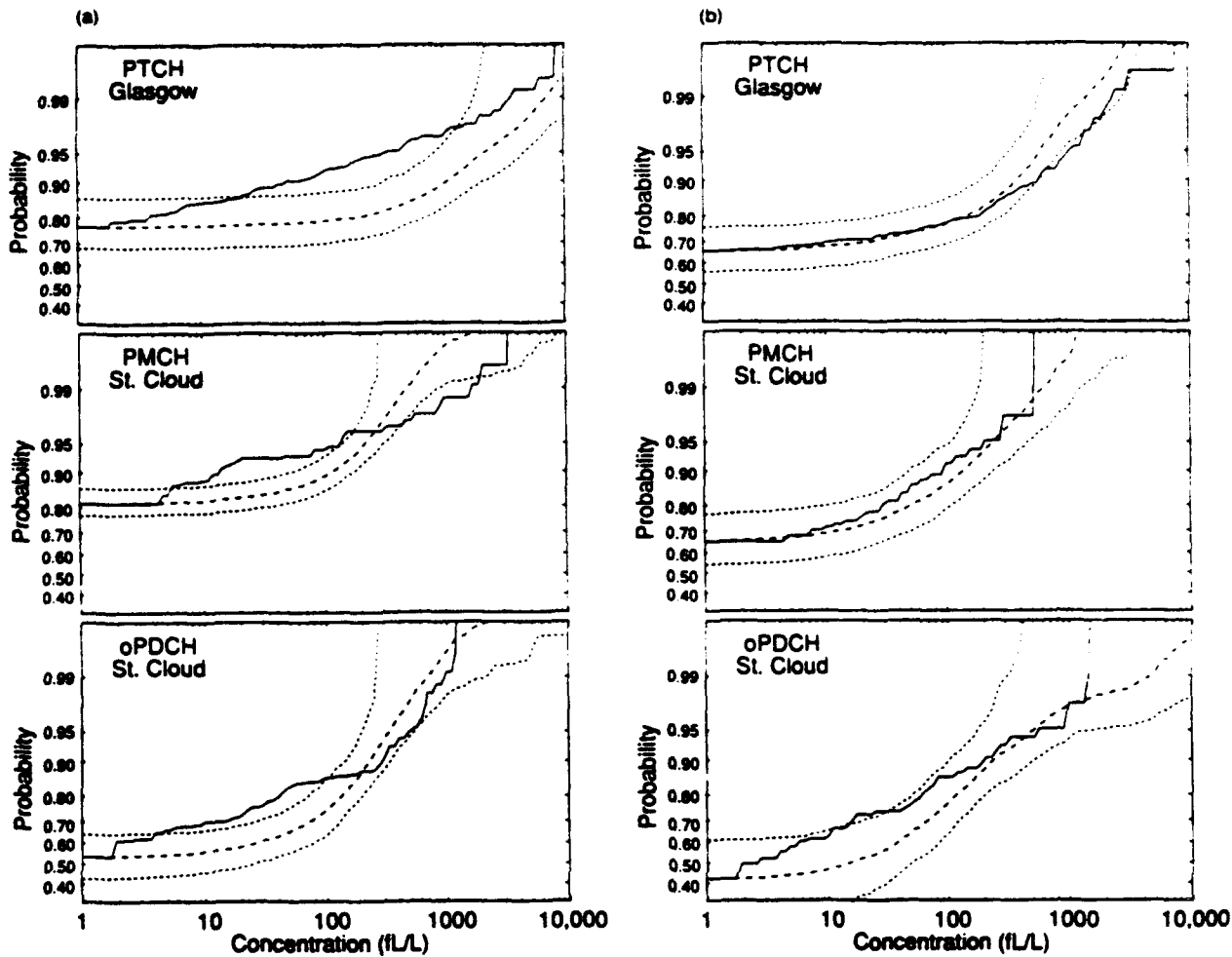


FIG. 11. Predicted and observed aircraft sample cumulative distribution functions (— observed; --- predicted; ····· 90% confidence limits). Predictions were made using a standard boundary layer. (a) Period 5 January–21 February with 1000-m boundary layer. (b) Period 9–28 March with 1500-m boundary layer.

This level was chosen as being effectively zero concentration so that only the distribution of nonzero concentrations can be compared, that is, concentrations greater than 1 fl l^{-1} . The small concentrations are ignored since the fraction of "zero" aircraft observations depends on the plume-locating skill of the flight observers.

The adjusted results for the two periods using the standard boundary-layer estimate are shown in Fig. 11, which includes the expected distribution together with 90% confidence bounds. The comparison between the predicted distributions and the aircraft observations is encouraging, although we note again the forced agreement at 1 fl l^{-1} . The information provided by the variance allows us to give a much better estimate of the expected short-term concentrations and also some measure of the confidence bounds on the prediction. The clipped normal function provides a reasonable description of the shape of the cumulative distribution.

especially for the March period where the observations lie almost completely within the 90% confidence bands.

It should be pointed out that the sampling procedure just described ignores correlation between observations since each random choice is made independently. Since the pathlengths do not generally provide more than a few observations within the tracer cloud we do not have the situation of strong correlation between adjacent samplers, and this is not a severe limitation. The effect of such correlation, in general, is to reduce the number of degrees of freedom in the problem and hence increase the width of the confidence band.

c. Ensemble predictions

The partitioning of the velocity fluctuations into resolved and turbulent components depends on the resolution of the measured wind field. As the detail in the wind field input is reduced, the uncertainty in the dis-

prediction is increased, along with the turbulent energy component. The applicability of our statistical prediction can be investigated by reducing the resolution of the wind input and testing the predictions based on the lower information content. An extreme test is provided by using an average of the wind field over the entire spatial domain and over the two time periods of interest. The resulting wind varies only with altitude and represents a long-term average for the eastern United States.

The mean and rms fluctuation component profiles for the two periods of NGM wind data are shown in Fig. 12. The mean wind is generally westerly and increases with height; the profiles are very similar except close to the surface where the March data shows near-stagnant conditions in the average. The rms fluctuation profiles are also very similar, with a value of $6\text{--}7\text{ m s}^{-1}$ in the lowest few kilometers and increasing up to around 15 m s^{-1} at $z = 8\text{ km}$.

Idealized profiles were specified for the model runs. Only the lowest few kilometers are relevant since the tracer is generally contained below 3 km. Linear velocity profiles were fit to the mean velocity and a constant value of $50\text{ m}^2\text{ s}^{-2}$ was used for the horizontal velocity variances. A length scale for the horizontal velocity fluctuations also needed to be specified, and it was found that $\Lambda_H = 2000\text{ km}$ gave a reasonably consistent description. First, this scale is typical of the large-scale eddies in the NGM field, and second the assumption of the $k^{-5/3}$ spectrum gives smaller-scale energies close to those assumed in the previous calculations. Thus, if the typical scale of $\Lambda_T = 30\text{ km}$ from section 3d is used, the appropriate energy at that scale in the ensemble flow would be $50(30/2000)^{2/3} \approx 3\text{ m}^2\text{ s}^{-2}$. It should be noted that the energy in the larger scales is probably not proportional to $k^{-5/3}$, but we believe that the most important feature here is the representation of the bulk of the spectrum. Over the transport times of this study, the concentration fluctuation scales do not grow larger than 2000 km and the representation of the long-wave end of the spectrum is not critical. The specification is best regarded as investigative and we hope to show that further study is warranted.

The dispersion calculation with the ensemble wind field is very simple, since the wind is steady and homogeneous. The standard diurnally varying boundary layers are used, which are representative of an ensemble average, for the calculation with a daytime maximum depth of 1000 m for January–February and 1500 m for March. The calculations are computationally fast, using only a few puffs that spread rapidly with the high turbulence levels and light wind.

We can compare only the cumulative distribution of the surface samples, since the prediction uses no information about particular days in the period. The mean concentration prediction is a very slow-moving, rapidly spreading circular Gaussian shape with the day-

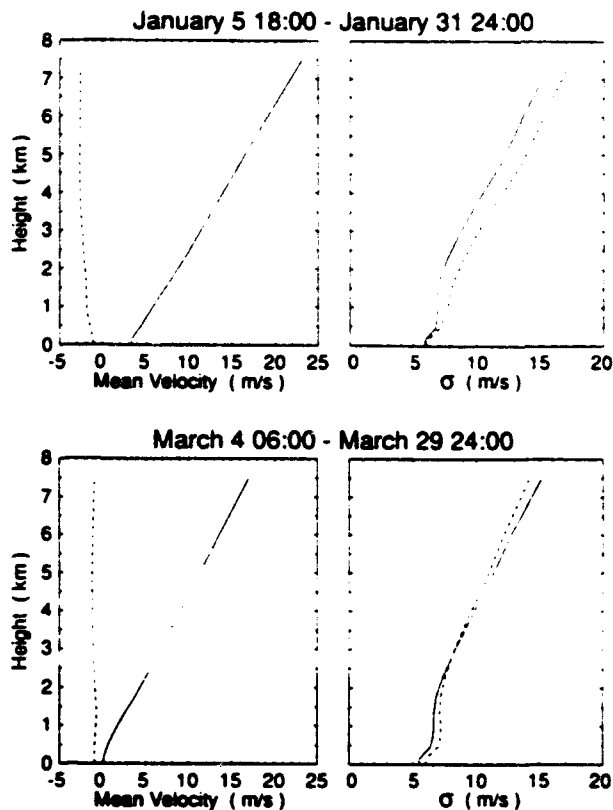


FIG. 12. Ensemble velocity profiles (— u ; --- v).

to-day variability represented statistically by the variance prediction. Expected cumulative distributions are generated in the same way as the aircraft predictions: by selecting randomly from a probability distribution at each sampler location. The variance was reduced by the appropriate averaging over the 24-h period of the observation, as described in appendix B, and the lognormal probability distribution function was found to give a much better fit to the data. The intermittency of the clipped-normal distribution gave poor agreement with the observations, perhaps as a result of the long time averaging that reduces the probability of a zero concentration.

The results of the simplified ensemble-average prediction for the two time periods are shown in Figs. 13a,b. The prediction is remarkably good considering the limited statistical information used in the calculation. The use of the concentration variance prediction and the assumed lognormal probability distribution allows an estimate of the 24-h average concentrations from the much longer averaging times in the wind statistics. The March statistics are very well predicted, except for the lowest concentrations of PTCH. It is not clear that the distribution below 1 fl l^{-1} is significant since the background noise levels are of this magnitude (see Table 1), but the results down to 0.1 fl l^{-1} are

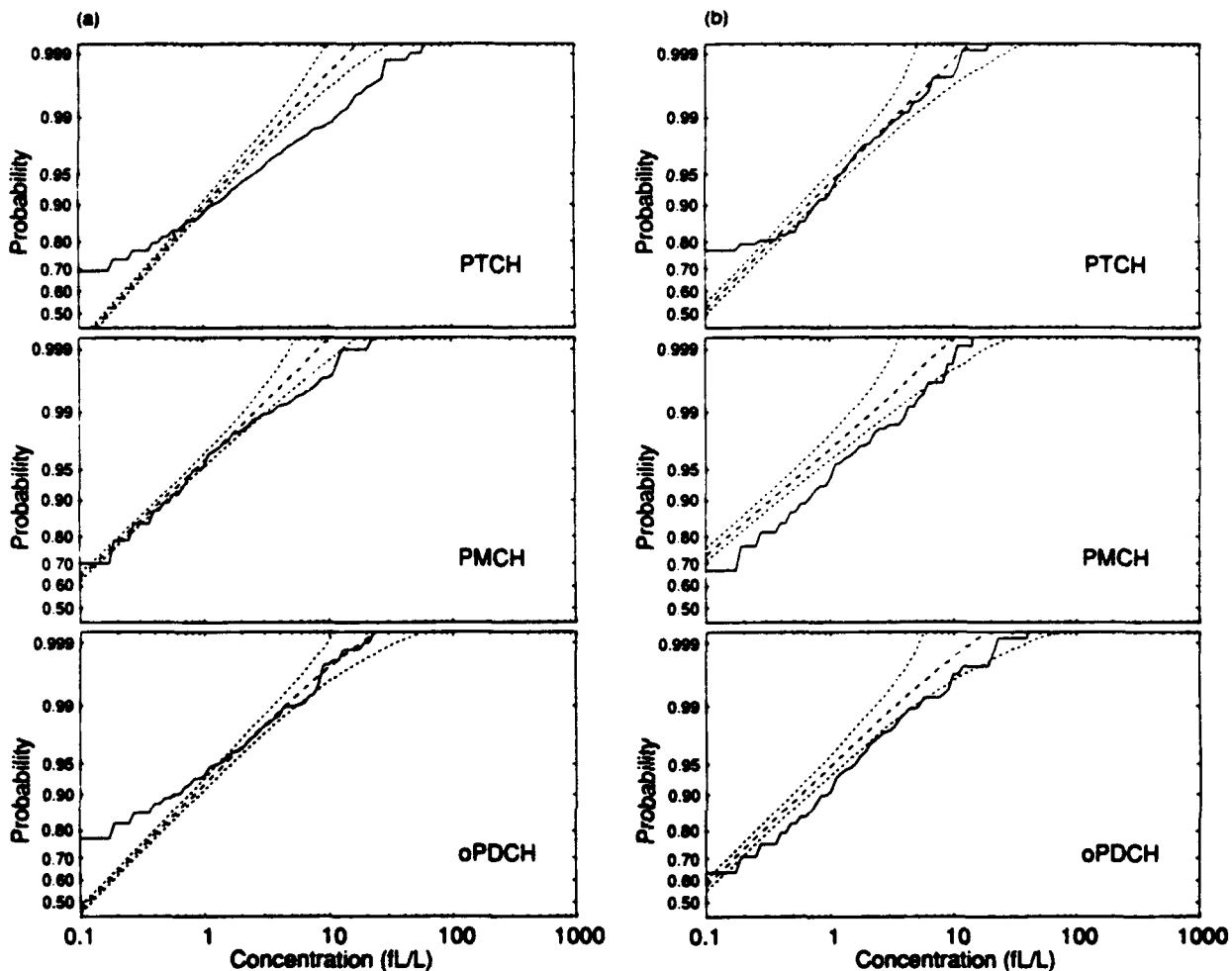


FIG. 13. Predicted and observed ground sample cumulative distribution functions. Predictions were made using the ensemble meteorology (— observed; --- predicted; ····· 90% confidence limits). (a) Period 5 January–21 February. (b) Period 9–28 March.

shown for completeness. The most significant error is in the PTCH distribution in the January–February period, which shows an underprediction of the values above 1 fl l^{-1} . The other tracers are better predicted, however, and generally show much closer resemblance to the March period distributions. The model results are also very similar for the two periods, since the wind statistics do not differ significantly.

Some skill is demonstrated in the prediction of the variation with distance, as shown in Fig. 14. Here the cumulative distributions of PTCH samples for March are shown along various sampler areas. We choose the March period because of the reasonably good overall prediction, and we have combined adjacent areas to increase the sample size and reduce the confidence bounds. The range of the confidence bounds is still large, but the model does show the general decrease with distance from the source.

5. Summary and conclusions

A Lagrangian puff model for long-range atmospheric dispersion, SCIPUFF, has been described. The model uses second-order turbulence closure methods to represent the diffusion processes and has been developed from shorter-range applications where boundary-layer turbulence dominates. The mesoscale velocity fluctuation statistics for longer-range calculations are based on recent descriptions of the energy spectrum from measurements and theoretical considerations. The Lagrangian framework provides an efficient description of the local concentration field and is coupled with splitting and merging algorithms to maintain an economical representation with appropriate resolution of the flow features. The internal puff concentration distribution is a fully general Gaussian shape so that shear distortion effects can be computed accurately.

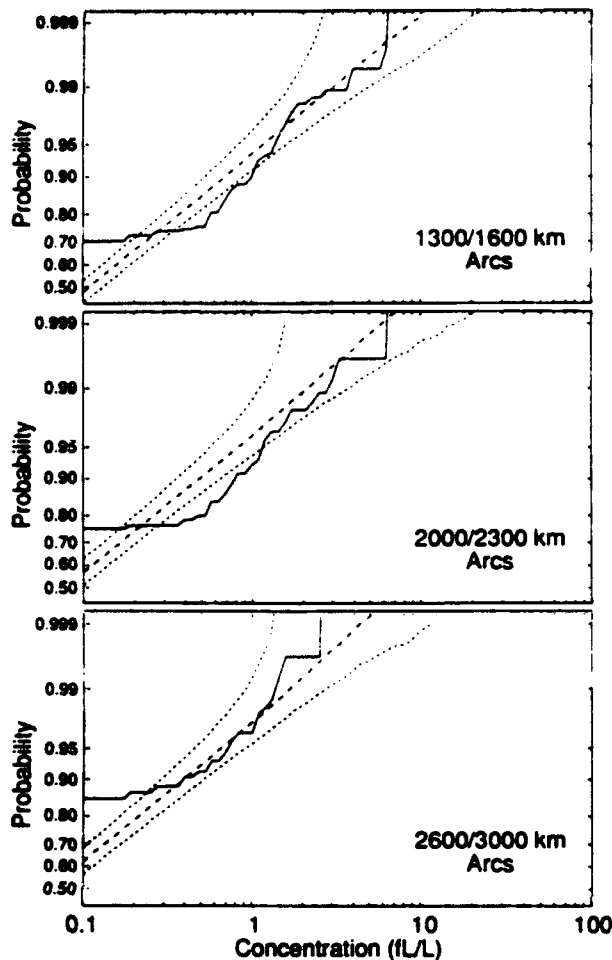


FIG. 14. Predicted and observed ground sample cumulative distribution function for oPDCH along three pairs of arcs for the period 9–28 March. Predictions were made using the ensemble meteorology (— observed; --- predicted; 90% confidence limits).

The turbulence closure includes a prediction for the concentration fluctuation variance, a measure of the random variability in an observable value. This can be used to provide a measure of the statistical significance in model evaluation. The variance prediction relates the uncertainty in the input wind field, that is, the turbulence velocity fluctuations, to the uncertainty in the predicted concentration field. Turbulent fluctuations are generally considered to be relatively small in scale, but the spectrum of atmospheric motions is continuous and the definition of the turbulent wind component depends on the detail of the available resolved wind field. One could also consider input wind inaccuracy as a stochastic component with a measurable spectrum, but our present understanding of the large-scale wind fluctuations is not sufficiently well developed for a quantitative assessment of the various contributing components.

The use of explicit velocity fluctuation statistics, and consideration of the spectral distribution of the fluctuation energy, allows a rational approach to the prediction of observable concentrations and the effects of sampling times. In contrast to the use of an empirical dispersion parameter based on averaging time, the turbulence closure framework provides an ensemble description of the concentration field and a method for predicting the statistics of any sampling procedure. The prediction requires assumptions for the probability distribution functions and correlation functions, but these can be made on a rational basis with the potential for direct measurement of these quantities at some time in the future.

The SCIPUFF model has been exercised on the ANATEX dispersion data using the wind fields from the NMC Nested Grid Model. The experiment recorded three months of 24-h average tracer concentrations on a sampler network ranging 3000 km from the source. The impact from multiple short-duration releases from two separate sources was measured at 77 ground-based samplers, providing a large database for evaluation purposes. In addition, aircraft samples of short duration were obtained within a few hundred kilometers of the sources. The model predictions and observed concentrations cannot be compared on a paired time and location basis due in part to the inaccuracy of the wind field, but the model predictions of the statistical distributions of the observed concentrations are generally good. There is a tendency for the model to overpredict the surface impact in the January–February period, and this is ascribed to the frequent shallow, stable boundary-layer predictions of the NGM. Use of a standard 1000-m-deep daytime layer improved the prediction significantly. A reasonably good prediction of the aircraft statistical distribution was also obtained by matching the observed fraction of zero concentrations to account for the conditional nature of the aircraft sampling and assuming a clipped normal probability distribution function.

As a further test of the statistical prediction, calculations were made with the average wind statistics for the entire NGM domain over the ANATEX periods. This modifies the turbulent wind component to include all the resolved variations in the NGM wind fields. The predicted concentration variance is much larger in this case, and a reasonable prediction of the observed distribution was found with a lognormal probability distribution for the 24-h samples.

In summary, a statistical dispersion model has been compared with the ANATEX observations using two different levels of resolution in the wind field. The results are very encouraging but would benefit greatly from further study of the statistical nature of the atmospheric flow fields. A number of speculative assumptions were necessary in the application of the model to the ANATEX cases, since reliable informa-

tion on spectral intensities, time and space correlation scales, and probability distribution functions is not currently available. The utility of a statistical prediction has been demonstrated in the calculation of confidence bounds in the comparison with the short-term samples from aircraft and in the ensemble wind-field prediction. The inherent uncertainty associated with any prediction of atmospheric transport over a long range is likely to always be significant, and research efforts can be devoted to describing or reducing it. The results presented above suggest that a quantitative description of the uncertainty is within reach.

Acknowledgments. This work was sponsored by the Defense Nuclear Agency under Contract DNA001-90-C-0100. The ANATEX data were provided by NOAA/ARL Atmospheric Sciences Modeling Division.

APPENDIX A

Source Specification

In principle, the plume emanating from a source with a mass flow rate F can be modeled by creating new puffs at each time step defined by a mass $Q = F\Delta t$, a centroid defined by the source location and second moments related to the source size. The subsequent plume evolution would then simply be computed using SCIPUFF. If the time step is long enough for the plume to travel more than the source diameter, however, then the spatial evolution of the plume during the time step must be considered. Since the dispersion time step is 15 min and the source size is less than 1 m, plume evolution during a time step is certainly a consideration. We therefore require a plume model to initialize puffs at the source for use in SCIPUFF. A simple model for the plume spread might be adequate for defining mass, location, and second moments, but the rapid evolution of the fluctuation variance c'^2 requires more sophisticated treatment. Therefore, a plume version of the full puff equations of section 3 are solved; that is, we march downstream from the source with a very small time step for a time t , computing dispersion in the vertical and lateral directions. The source time t_s is chosen so that the puff time scales are large enough to be resolved by the SCIPUFF calculation time step, Δt ; $t_s = 60$ min in the ANATEX calculations.

At each time step, a puff is initialized at the wind-translated location corresponding to a time t_s after release, with a streamwise spread of $U\Delta t$, where U is the local wind speed. All other moments are obtained from the plume calculation. Thus, for example, the plume initialization solves

$$\frac{dx}{dt} = U(x_s, t) \quad (\text{A1})$$

$$\frac{d}{dt} \sigma_{yy} = F_{yy} \quad (\text{A2})$$

$$\frac{d}{dt} F_{yy} = 2\overline{v_s'^2} - Aq_H F_{yy}, \quad (\text{A3})$$

where x_s is the source location, $U(x_s, t)$ is the velocity at the source, and $\overline{v_s'^2}$ is the velocity variance. Equations (A1)–(A3) are integrated out to $t = t_s$; then the puff spatial moments are rotated from the local frame determined by the plume into the SCIPUFF coordinate system. The two horizontal diffusivities, $F_{11\sigma}$ and $F_{22\sigma}$, are initialized with the value of F_{yy} from the plume calculation.

The calculation of the mean-square concentration, S_σ , proceeds similarly, except that there is only a self-interaction term in the plume equivalent of (18) and the overlap integral is two-dimensional. These plume equations are essentially those described by Sykes et al. (1986), except for one subtle point associated with the anisotropic treatment of the turbulence. The special treatment of the vertical dispersion and the extra dissipation term, (23), are retained in the plume calculation. This implies that the variance production is only a result of the lateral dispersion, and this one-dimensional situation requires that the coefficient of $2bs$ in (22) be reduced to bs in order to be consistent with the Gifford meandering plume result (Gifford 1959).

APPENDIX B

Effect of Averaging on the Fluctuations

The field observations of tracer concentrations involve averaging, either purely temporal in the case of the 24-h ground samples or mostly spatial for the aircraft data. SCIPUFF predicts the instantaneous fluctuations variance, which is reduced by the averaging process, and the reduction must be accounted for before comparing with the observations.

If the average concentration is defined as

$$\Gamma = \frac{1}{T} \int_{t_0-T/2}^{t_0+T/2} c(t) dt, \quad (\text{B1})$$

then

$$\bar{\Gamma} = \frac{1}{T} \int_{t_0-T/2}^{t_0+T/2} \bar{c}(t) dt \quad (\text{B2})$$

and

$$\begin{aligned} \overline{\Gamma'^2} &= \frac{1}{T^2} \iint \overline{c'(t)c'(t')} dt dt' \\ &= \frac{1}{T^2} \iint \overline{c'^2(t)} \rho(t; t') dt dt', \end{aligned} \quad (\text{B3})$$

where

$$\rho(t; t') = \frac{\overline{c'(t)c'(t')}}{\overline{c'^2(t)}}.$$

If $c(t)$ is a stationary process, then (B3) reduces to the standard result of Tennekes and Lumley (1977): that is,

$$\overline{\Gamma'^2} = \frac{2}{T} \overline{c'^2} \int_0^T \left(1 - \frac{t'}{T}\right) \rho(t') dt'. \quad (\text{B4})$$

The estimate of the variance in an averaged observation requires an estimate of the correlation function. For the stationary case, an exponential form is assumed, so that

$$\overline{\Gamma'^2} = 2 \overline{c'^2} \frac{(\beta - 1 + e^{-\beta})}{\beta^2},$$

where $\beta = T/T_c$ and $\rho(t') = e^{-t'/T_c}$.

For the general, nonstationary case, a crude approximation for (B3) is used, effectively assuming

$$\rho(t') = \begin{cases} 1, & |t'| < T_c \\ 0, & |t'| > T_c. \end{cases}$$

Then (B3) becomes

$$\overline{\Gamma'^2} = \frac{2}{T^2} \int_0^T \overline{c'^2}(t) \min\{t, T_c(t)\} dt. \quad (\text{B5})$$

All of the above discussion applies immediately to the case of spatial averaging if t is regarded as distance along the path of integration and T_c is replaced by l_c , the integral scale of the spatial correlation.

The integral scales are specified in terms of the predicted fluctuation scale l_H using the relations

$$l_c = 2l_H \quad (\text{B6})$$

and

$$T_c = \frac{0.75l_H}{\max(U', q_H)}. \quad (\text{B7})$$

The time scale, (B7), is based on short-range estimates from large-eddy simulations (Sykes and Henn 1992), while the spatial scale is determined from idealized calculations for randomly displaced Gaussian puffs. Both estimates should be regarded as very speculative at this stage and need more direct measurements of the fluctuations on the larger scale.

REFERENCES

- Bass, A., 1980: Modelling long range transport and diffusion. *Proc. Second Joint Conf. on Application of Air Pollution Meteorology*, New Orleans. Amer. Meteor. Soc., 193-215.
- Clark, T. L., and R. D. Cohn, 1990: The Across North America Tracer Experiment (ANATEX) model evaluation study. U.S. Environmental Protection Agency Rep. EPA/600/3-90/051, 142 pp.
- Csanady, G. T., 1973: *Turbulent Diffusion in the Environment*. D. Reidel, 248 pp.
- Draxler, R. R., 1990: The calculation of low-level winds from the archived data of a regional primitive equation forecast model. *J. Appl. Meteor.*, 29, 240-248.
- , 1991: The accuracy of trajectories during ANATEX calculated using dynamic model analyses versus rawinsonde observations. *J. Appl. Meteor.*, 30, 1446-1467.
- , and J. L. Heffter, 1989: Across North America Tracer Experiment (ANATEX). Volume I: Description, ground-level sampling at primary sites, and meteorology. NOAA Air Resources Laboratory, Tech. Memo. ERL ARL-167, 83 pp.
- , R. J. Lagomarsino, and G. Start, 1991: Across North America Tracer Experiment (ANATEX): Sampling and analysis. *Atmos. Environ.*, 25A, 2815-2836.
- Fox, D. G., 1981: Judging air quality model performance. *Bull. Amer. Meteor. Soc.*, 62, 599-609.
- Gifford, F. A., 1959: Statistical properties of a fluctuating plume dispersal model. *Adv. Geophys.*, 6, 117-137.
- , 1985: Atmospheric diffusion in the range 20 to 2000 kilometers. *Air Pollution Modeling and Its Applications*, C. D. Wepelaere, F. A. Schiermeier, and N. V. Gillani, Eds., Plenum Press, 247-265.
- , 1988: A similarity theory of the tropospheric turbulence energy spectrum. *J. Atmos. Sci.*, 45, 1370-1379.
- Heffter, J. L., and R. R. Draxler, 1989: Across North America Tracer Experiment (ANATEX). Volume III: Sampling at Tower and Remote Sites. NOAA Air Resources Laboratory, Tech. Memo. ERL ARL-175, 67 pp.
- Lewellen, W. S., 1977: Use of invariant modeling. *Handbook of Turbulence*, W. Frost and T. H. Moulden, Eds., Plenum Press, 237-280.
- , and R. I. Sykes, 1986: Analysis of concentration fluctuations from lidar observations of atmospheric plumes. *J. Climate Appl. Meteor.*, 25, 1145-1154.
- , and —, 1989: Meteorological data needs for modeling air quality uncertainties. *J. Atmos. Oceanic Technol.*, 6, 759-768.
- , S. F. Parker, D. S. Henn, N. L. Seaman, D. R. Stauffer, and T. T. Warner, 1988: A hierarchy of dynamic plume models incorporating uncertainty. Vol. 1: Overview. EPRI Report EPRI EA-6095, Project 1616-28, 180 pp.
- Nastrom, G. D., and K. S. Gage, 1985: A climatology of atmospheric wavenumber spectra of wind and temperature observed by commercial aircraft. *J. Atmos. Sci.*, 42, 950-960.
- Stundler, B. J. B., and R. R. Draxler, 1989: Across North America Tracer Experiment (ANATEX). Volume II: Aircraft-based sampling. NOAA Air Resources Laboratory Tech. Memo., ERL ARL-177, 62 pp.
- Sykes, R. I., and D. S. Henn, 1992: Large-eddy simulation of concentration fluctuations in a dispersing plume. *Atmos. Environ.*, 26A, 3127-3144.
- , W. S. Lewellen, and S. F. Parker, 1984: A turbulent-transport model for concentration fluctuations and fluxes. *J. Fluid Mech.*, 139, 193-218.
- , —, and —, 1986: A Gaussian plume model of atmospheric dispersion based on second-order closure. *J. Climate Appl. Meteor.*, 25, 322-331.
- , —, and D. S. Henn, 1988: A hierarchy of dynamic plume models incorporating uncertainty. Vol. 4: Second-order closure integrated puff. EPRI Report EPRI EA-6095, Project 1616-28, 99 pp.
- Tennekes, H., and J. L. Lumley, 1977: *A First Course in Turbulence*. MIT Press, 300 pp.
- Venkatram, A. K., 1982: A framework for evaluating air quality models. *Bound.-Layer Meteor.*, 24, 371-385.

DISTRIBUTION LIST

DNA-TR-93-61

DEPARTMENT OF DEFENSE

ASSISTANT TO THE SECRETARY OF DEFENSE
ATTN: EXECUTIVE ASSISTANT

DEFENSE INTELLIGENCE AGENCY
ATTN: DIW-4
ATTN: PAA-1A G WEBER

DEFENSE NUCLEAR AGENCY
ATTN: OPNA
ATTN: SPSD
3 CY ATTN: SPWE DR C GALLOWAY
ATTN: TDTR
2 CY ATTN: TITL

DEFENSE TECHNICAL INFORMATION CENTER
2 CY ATTN: DTIC/OC

FIELD COMMAND DEFENSE NUCLEAR AGENCY
ATTN: FCTO
ATTN: FCTT
ATTN: FCTT-T W SUMMA

DEPARTMENT OF THE ARMY

ARMY RESEARCH LABORATORIES
ATTN: AMSRL-SL-CE

DEP CH OF STAFF FOR OPS & PLANS
ATTN: DAMO-NCZ

U S ARMY ATMOSPHERIC SCIENCES LAB
ATTN: SLCAS-AR-M R SUTHERLAND

U S ARMY BALLISTIC RESEARCH LAB
ATTN: SLCBR-SS-T
ATTN: SLCBR-TB-B G BULMASH

U S ARMY ENGR WATERWAYS EXPER STATION
ATTN: C WELCH CEWES-SE-R
ATTN: D RICKMAN CEWES-SE-R
ATTN: E JACKSON CEWES-SD-R
ATTN: F DALLRIVA CEWES-SS-R
ATTN: J BALSARA CEWES-SS-R

U S ARMY NUCLEAR & CHEMICAL AGENCY
ATTN: MONA-NU DR D BASH

DEPARTMENT OF THE NAVY

NAVAL RESEARCH LABORATORY
ATTN: CODE 5227 RESEARCH REPORT

NAVAL SURFACE WARFARE CENTER
ATTN: L VALGE

NAWCWPNSDIV DETACHMENT
ATTN: CLASSIFIED LIBRARY

OFFICE OF CHIEF OF NAVAL OPERATIONS
ATTN: NUC AFFAIRS & INT'L NEGOT BR

DEPARTMENT OF THE AIR FORCE

AERONAUTICAL SYSTEMS CENTER
ATTN: ENSSS H GRIFFIS

AIR UNIVERSITY LIBRARY
ATTN: AFIT/LD
ATTN: AUL-LSE

HQ USAF/XOFN
ATTN: XOFN

PHILLIPS LABORATORY
ATTN: PLWS MR SHARP

DEPARTMENT OF ENERGY

LAWRENCE LIVERMORE NATIONAL LAB
ATTN: PAUL GUDIJKSEN
ATTN: R PERRETT

LOS ALAMOS NATIONAL LABORATORY
ATTN: A S MASON
ATTN: J NORMAN
ATTN: R W SELDEN
ATTN: R W WHITAKER
ATTN: B SHAFER

SANDIA NATIONAL LABORATORIES
ATTN: A CHABAI DIV 9311

U.S. DEPARTMENT OF ENERGY
OFFICE OF MILITARY APPLICATIONS
ATTN: OMA/DP-252 MAJ D WADE

OTHER GOVERNMENT

CENTRAL INTELLIGENCE AGENCY
ATTN: OSWR/NED
ATTN: OSWR/S WALLENHORST

DEPARTMENT OF DEFENSE CONTRACTORS

JAYCOR
ATTN: CYRUS P KNOWLES

KAMAN SCIENCES CORP
ATTN: D MOFFETT
ATTN: DASIAC
4 CY ATTN: J NYDEN

KAMAN SCIENCES CORPORATION
ATTN: DASIAC

SCIENCE APPLICATIONS INTL CORP
ATTN: D BACON
ATTN: J COCKAYNE
ATTN: P VERSTEEGEN
ATTN: W LAYSON

THE TITIAN CORPORATION
2 CY ATTN: D S HENN
2 CY ATTN: R I SYKES
2 CY ATTN: S F PARKER